Studies on radio frequency dressed potentials for cold atoms

By

ARIJIT CHAKRABORTY

PHYS03201204016

Raja Ramanna Centre for Advanced Technology, Indore

A thesis submitted to the

Board of Studies in Physical Sciences

In partial fulfillment of requirements

For the Degree of

DOCTOR OF PHILOSOPHY

of

HOMI BHABHA NATIONAL INSTITUTE



October, 2018

Homi Bhabha National Institute

Recommendations of the Viva Voce Board

As members of the Viva Voce Board, we certify that we have read the dissertation prepared by Arijit Chakraborty entitled "Studies on radio frequency dressed potentials for cold atoms" and recommend that it maybe accepted as fulfilling the dissertation requirement for the Degree of Doctor of Philosophy.

Date: 29-10-18

Chairman - Dr. K. S. Bindra

Date: 29.10.2018

Guide/Convener - Dr. S. R. Mishra

Date: 29/10/2018

Examiner - Dr. U. Rapol

Date: 29/10/2018

External Member - Dr. S. Pradhan

Date: 29/10/2018

Member 1 - Dr. P. K. Mukhopadhyay

Date: 29/10/18

Member 2 - Dr. S. K. Majumder

Date: 29/10/18

Member 3 - Dr. C. Mukherjee

Date: 29/10/2018

Member 4 - Dr. A. Moorti

Final approval and acceptance of this dissertation is contingent upon the candidate's submission of the final copies of the dissertation to HBNI.

I hereby certify that I have read this dissertation prepared under my direction and recommend that it may be accepted as fulfilling the dissertation requirement.

Date: 29th October, 2018

Place: RRCAT, Indore

Dr. S. R. Mishra
Guide

ACKNOWLEDGEMENTS

Now that finally I am at the doorstep to start the next chapter of my life, it is indeed a pleasure to acknowledge the people whose support kept me going in the past five years. May that be at dinner time chatter after a long exhausting day of lab work or the moral support after knowing the days work failed to live upto the high expectations, my friends and colleagues gave me support which I will always remember. The possibility of acknowledging everyone with whom I walked this path, is tiny, not because I forgot some of them but because I remember all of them and what they did for me. I am quite positive that the friendship I made with my seniors, juniors and batch mates in RRCAT will last for a long time, if not forever.

But, no matter how much anonymous I intend this acknowledgement to be, I must thank those whose support was imperative in this journey. My supervisor, Dr. S. R. Mishra should be the first one I thank for his encouragement for letting me explore all the odd projects I came up with during my Ph D work. I must say thank you to my lab mates, Dr. Surjya Prakash Ram and Sanjiv Kumar Tiwari for being patient with me while teaching me how to perform cold atom experiments. My other two lab mates Amrita Srivastava and Charu Mishra deserve a thank you not only for their help in the past few years but also for becoming one of those selected persons whom I call friend. I am really thankful to all my group members Dr. Surendra Singh, Vivek Singh, Amit Chaudhary and Dr. Vibhuti Bhushan Tiwari. It was almost a perfect blend of honor and joy to work with them.

I acknowledge the Doctoral Committee and the Director RRCAT for providing the support to complete my work.

Dedicated to my family

3. Trapping of laser cooled ^{87}Rb atoms in spatially separated different radio frequency dressed states by A Chakraborty, S. R. Mishra, S. P. Ram, S. K. Tiwari and H.S. Rawat, National Laser Symposium (NLS-25), Bhubaneshwar, India, 2016.

4. Evolution of laser cooled ^{87}Rb atom cloud in a time varying radio-frequency dressed potential A. Chakraborty, S. R. Mishra and S. P. Ram, National Laser Symposium (NLS-26), Mumbai, India, 2017.

5. Comparative studies on radio frequency dressed lattice potentials and optical lattices by A. Chakraborty and S. R. Mishra, International Conference on Recent Trends in Cold and Ultracold Matter, IIT Guwahati, India, 2018.

Arijit Chakraborty
29/10/2018

(Arijit Chakraborty)

List of Publications arising from the thesis

Journal:

1. Anisotropic Two-dimensional RF-dressed Potentials for Ultracold Atoms by A. Chakraborty and S. R. Mishra, J.Kor.Phys.Soc. 65 (9), 1324 (2014).

2. A toroidal trap for cold ^{87}Rb atoms using an rf-dressed quadrupole trap by A Chakraborty, S R Mishra, S P Ram, S K Tiwari and H S Rawat, J. Phys. B: At. Mol. Opt. Phys. 49, 075304 (2016).

3. A Floquet formalism for the interaction of magnetically trapped atoms with rf-fields by A. Chakraborty and S. R. Mishra, J. Phys. B: At. Mol. Opt. Phys. 51, 025002 (2018).

4. Resonance enhancement of two photon absorption by magnetically trapped atoms in strong rf-fields by A. Chakraborty and S. R. Mishra, Phys Lett A 382 (4), 157 (2018).

5. Evolution of a cold atom cloud in a time dependent rf-dressed potential by A. Chakraborty, S. R. Mishra, S. P. Ram, S. K. Tiwari, and H. S. Rawat, arXiv:1606.04302.

Conferences:

1. Trapping laser cooled ^{87}Rb atoms in a ring trap by A Chakraborty, S. R. Mishra, S. P. Ram, S. K. Tiwari and H.S. Rawat, National Laser Symposium (NLS-24), Indore, India, 2015.

2. Dynamics of finite temperature condensates in rf-dressed potentials using PySol, Multicomponent Atomic Condensates and Rotational Dynamics (MACRO), Newcastle, UK, 2016.

DECLARATION

I, hereby declare that the investigtion presented in the thesis has been carried out by me. The work is original and has notbeen submitted eralier as a whole or in part for a degree / diploma at this or any other Institution / University.

Arijit Chakraborty
29/10/2018

(Arijit Chakraborty)

STATEMENT BY AUTHOR

This dissertation has been submitted in partial fulfillment of requirements for an advanced degree at Homi Bhabha National Institute (HBNI) and is deposited in the Library to be made available to borrowers under rules of the HBNI.

Brief quotations from this dissertation are allowable without special permission, provided that accurate acknowledgement of source is made. Requests for permission for extended quotation from or reproduction of this manuscript in whole or in part may be granted by the Competent Authority of HBNI when in his or her judgment the proposed use of the material is in the interests of scholarship. In all other instances, however, permission must be obtained from the author.

Arijit Chakraborty
29/10/2018

(Arijit Chakraborty)

4.3 Numerical results and comparison with experimental observations 73
4.4 Evolution after trap formation 76
4.5 Conclusion 78

5 Radio-frequency dressed traps with poly-chromatic rf-fields 79
5.1 Many Mode Floquet Theory 80
5.2 Establishment of validity of MMFT approach 86
5.2.1 Comparison of MMFT with other techniques for single mode rf-field 87
5.2.2 Comparison of MMFT with earlier methods for two mode rf-field 90
5.2.3 Effect of truncation of the infinite matrices in MMFT 94
5.3 Results of MMFT on interaction of atoms with the polychromatic rf-field . 96
5.3.1 Analysis of the Floquet spectrum 96
5.3.2 Dependence of eigen-energies on field parameters 99
5.3.3 Dependence of transition probabilities on rf-field parameters . . . 105
5.4 Conclusion 108

6 Conclusion 109
6.1 Summary 109
6.2 Future plan 112

Bibliography 113

2.2.1 Symmetric traps . . . 34
2.2.2 Asymmetric ring traps . . . 36
2.2.3 Rotating traps . . . 39
2.3 Conclusion . . . 44

3 Experimental realization of rf-dressed potentials for cold ^{87}Rb atoms 45
3.1 Experimental Setup . . . 46
3.1.1 Vacuum systems . . . 46
3.1.2 Laser systems and optical layout . . . 49
3.1.3 Magnetic trap and rf-field sources . . . 52
3.1.4 Controller system . . . 53
3.2 Sequence of experimental procedure . . . 53
3.2.1 Formation of magneto-optical traps . . . 54
3.2.2 Optical molasses and optical pumping . . . 55
3.2.3 Loading of quadrupole magnetic trap . . . 55
3.2.4 Radio frequency dressing of trapped atoms . . . 56
3.2.5 Imaging of the atom cloud . . . 56
3.3 Observations on ^{87}Rb atom cloud trapped in rf-dressed potential . . . 57
3.3.1 Formation of ring trap using two rf-fields . . . 57
3.3.2 Ring radius measurements . . . 59
3.3.3 Formation of ring trap using single rf source . . . 60
3.3.4 Formation of tilted ring cloud . . . 61
3.3.5 Concentric atom trapping clouds using two rf-fields . . . 62
3.4 Conclusion . . . 63

4 Evolution of atom clouds in time varying rf-dressed potentials 65
4.1 Direct Simulation Monte Carlo Technique . . . 66
4.2 Experimental observations on time evolution of atom cloud trapped in rf-dressed potentials . . . 70

Table of Contents

Synopsis **xii**

List of Figures **xxiv**

1 An introduction to laser cooling **1**

1.1 Fundamentals of atom light interaction 2

1.2 Force exerted on atoms by radiation fields 6

1.3 Basic cooling and trapping techniques 7

1.3.1 Doppler cooling of atoms and optical molasses 9

1.3.2 Sub-Doppler cooling of multilevel atoms 11

1.3.3 Magneto Optical Trap 13

1.3.4 Magnetic trapping of atoms 15

1.3.5 Evaporative cooling 16

1.4 Characterization of cold atom clouds 18

1.4.1 Absorption imaging of the cold atom cloud 18

1.4.2 Fluorescence imaging of the cold atom cloud 19

1.4.3 Phase contrast imaging of the cold atom cloud 19

1.4.4 Measurement of temperature of atom cloud 20

1.5 Remarks 21

2 Radio-frequency dressed potentials **25**

2.1 Theory 26

2.2 Trapping geometries 33

(3) Trapping of laser cooled ^{87}Rb atoms in spatially separated different radio frequency dressed states by A Chakraborty, S. R. Mishra, S. P. Ram, S. K. Tiwari and H.S. Rawat. National Laser Symposium (NLS-25), Bhubaneshwar, India, 2016.

(4) Evolution of laser cooled ^{87}Rb atom cloud in a time varying radio-frequency dressed potential A. Chakraborty, S. R. Mishra and S. P. Ram. National Laser Symposium (NLS-26), Mumbai, India, 2017.

Signature of Student: Amijit Chakraborty

Date: 13.03.2018

No.	Name	Designation	Signature	Date
1.	Dr. K. S. Bindra	Chairman		13/03/18
2.	Dr. S. R. Mishra	Guide/ Convener	SRMishra	13.3.18
3.	Dr. S. Pradhan	External Member		13/3/18
4.	Dr. P. K. Mukhopadhyay	Member		13/3/18
5.	Dr. S. K. Majumder	Member		13/3/18
6.	Dr. C. Mukherjee	Member		13/3/18
7.	Dr. A. Moorti	Member		12/3/18.

Publications in Refereed Journal:

(a) Published:

(1) Anisotropic Two-dimensional RF-dressed Potentials for Ultracold Atoms by A. Chakraborty and S. R. Mishra, J.Kor.Phys.Soc. 65 (9), 1324 (2014).

(2) A toroidal trap for cold ^{87}Rb atoms using an rf-dressed quadrupole trap by A Chakraborty, S R Mishra, S P Ram, S K Tiwari and H S Rawat, J. Phys. B: At. Mol. Opt. Phys. 49, 075304 (2016).

(3) A Floquet formalism for the interaction of magnetically trapped atoms with rf-fields by A. Chakraborty and S. R. Mishra, J. Phys. B: At. Mol. Opt. Phys. 51, 025002 (2018).

(4) Resonance enhancement of two photon absorption by magnetically trapped atoms in strong rf-fields by A. Chakraborty and S. R. Mishra, Phys Lett A 382 (4), 157 (2018).

(b) Accepted:

(c) Communicated:

(1) Evolution of a cold atom cloud in a time dependent rf-dressed potential by A. Chakraborty, S. R. Mishra, S. P. Ram, S. K. Tiwari, and H. S. Rawat.

Other Publications:

(a) Book/Book Chapter:

(b) Conference/Symposium:

(1) Trapping laser cooled ^{87}Rb atoms in a ring trap by A Chakraborty, S. R. Mishra, S. P. Ram, S. K. Tiwari and H.S. Rawat, National Laser Symposium (NLS-24), Indore, India, 2015.

(2) Dynamics of finite temperature condensates in rf-dressed potentials using PySol, Multicomponent Atomic Condensates and Rotational Dynamics (MACRO), Newcastle, UK, 2016.

[12] Walther Gerlach and Otto Stern. *Zeitschrift für Physik*, 9(1):349–352, 1922.

[13] O. Zobay and B. M. Garraway. *Phys. Rev. Lett.*, 86:1195–1198, 2001.

[14] Colombe, Y., Knyazchyan, E., Morizot, O., Mercier, B., Lorent, V., and Perrin, H. *Europhys. Lett.*, 67(4):593–599, 2004.

[15] Arijit Chakraborty and Satya Ram Mishra. *J. of the Kor. Phys. Soc.*, 65:1324–1335, 2014.

[16] A Chakraborty, S R Mishra, S P Ram, S K Tiwari, and H S Rawat. *Journal of Physics B: Atomic, Molecular and Optical Physics*, 49(7):075304, 2016.

[17] A Chakraborty and S R Mishra. *Journal of Physics B: Atomic, Molecular and Optical Physics*, 51(2):025002, 2018.

[18] A. Chakraborty and S.R. Mishra. *Physics Letters A*, 382(4):157 – 161, 2018.

[3] Igor B Mekhov and Helmut Ritsch. *Journal of Physics B: Atomic, Molecular and Optical Physics*, 45(10):102001, 2012.

[4] T Schumm, S. Hofferberth, et. al. *Nature Physics*, 1:57, 2005.

[5] Franco Dalfovo, Stefano Giorgini, Lev P. Pitaevskii, and Sandro Stringari. *Rev. Mod. Phys.*, 71:463–512, 1999.

[6] W. K. Hensinger, H. Hffner, A. Browaeys, N. R. Heckenberg, K. Helmerson, C. McKenzie, G. J. Milburn, W. D. Phillips, S. L. Rolston, H. Rubinsztein-Dunlop, and B. Upcroft. *Nature*, 412:52, 2001.

[7] Michael Albiez, Rudolf Gati, Jonas Fölling, Stefan Hunsmann, Matteo Cristiani, and Markus K. Oberthaler. *Phys. Rev. Lett.*, 95:010402, 2005.

[8] Andrew D. Ludlow, Martin M. Boyd, Jun Ye, E. Peik, and P. O. Schmidt. *Rev. Mod. Phys.*, 87:637–701, 2015.

[9] A. Günther, S. Kraft, C. Zimmermann, and J. Fortágh. *Phys. Rev. Lett.*, 98:140403, 2007.

[10] S. Abend, M. Gebbe, M. Gersemann, H. Ahlers, H. Müntinga, E. Giese, N. Gaaloul, C. Schubert, C. Lämmerzahl, W. Ertmer, W. P. Schleich, and E. M. Rasel. *Phys. Rev. Lett.*, 117:203003, 2016.

[11] D. Sheng, S. Li, N. Dural, and M. V. Romalis. *Phys. Rev. Lett.*, 110:160802, 2013.

being controlled by the mode separation of the polychromatic rf-field. The obtained potentials were compared with an approximate analytical expression to estimate the trap depth, width and trap frequency of lattice well potential. These lattice potentials are flexible and easy to manipulate than their optical counterparts. A large two photon transition probability was also observed between the Zeeman hyperfine sub-levels with a dependence on the applied rf-field strength and mode separation of the polychromatic rf-field. These observations are fascinating due to their applicability in rf-spectroscopy to precisely determine the temperature of a trapped atom cloud. These results have also published in peer reviewed journals [17, 18]

The conclusions of the research work carried out in the thesis is presented in **Chapter 6** along with the scope of the future work. The thesis predicts various trapping geometries using static quadrupole trap and rf-fields. Some of the predicted geometries have been experimentally demonstrated. In future, work may be carried out to demonstrate the lattice like periodic potentials with the rf-field having polychromatic spectrum.

References

[1] A V Taichenachev, V I Yudin, and S N Bagayev. *Journal of Physics: Conference Series*, 793(1):012027, 2017.

[2] John Weiner, Vanderlei S. Bagnato, Sergio Zilio, and Paul S. Julienne. *Rev. Mod. Phys.*, 71:1–85, 1999.

final value of the frequency in the ramp. Further, the decay of the number of trapped atoms in the atom cloud during the ramp of rf-field (amplitude and frequency) had shown two distinct regimes. In the initial phase, the removal of hotter atoms due to the evaporation mechanism led to a faster decay of the trapped atoms. In the later phase, the atom number was almost unchanged while the shape of the atom cloud was changing, having lower loss rates in the rf-dressed potential. A numerical technique based on the direct simulation Monte Carlo (DSMC) method was developed to gain the insight into physical processes occurring during the ramp. This numerical simulation revealed that after the complete transfer of the atoms from one dressed state to another state is the dominating mechanism involved in the formation of the ring trap.

In **Chapter 5**, the rf-dressed trapping potentials with a polychromatic rf-field have been studied theoretically using the many mode Floquet theory (MMFT). In this theoretical framework, the applied rf-field spectrum was considered to be of comb type. The amplitude envelop function in the comb can be chosen to generate any arbitrary type of rf-field spectrum. The Floquet Hamiltonian was constructed using the basis sets of infinite Fourier components corresponding to the rf-field central frequency ω_0 and separation frequency ω_r. The eigen-energies of the Hamiltonian to evaluate the rf-dressed potentials have been calculated numerically by truncating the Hamiltonian appropriately. These rf-dressed potentials with polychromatic rf-field have shown a spatially periodic lattice like structure with the lattice parameter

nected to a circular copper loop antenna via an impedance matching circuit. This multi-turn loop antenna was used for applying the dressing rf-field to the atoms trapped in the quadrupole trap. A different antenna was used for the evaporative cooling before loading the rf-dressed potentials. Absorption imaging technique was used for characterization of the trapped cloud. A field programmable gate array (FPGA) card based controller system was utilized to control the duration, sequence and synchronization of various processes during the experiments. The controller system was operated through an industrial PC and LabVIEW software. The detailed description of these experimental procedures is given in this chapter.

The experimental realization of the rf-dressed ring trap with a single rf ramp and single antennae was also tried. This is an extremely useful technique to trap atoms in a ring type potential whose radius can be varied by changing the final value of the rf-field frequency during the frequency ramp. The results were published in a journal [16].

Chapter 4 describes the study of the transformation of the quadrupole trap into an rf-dressed ring trap in presence of the applied rf-field. The ^{87}Rb atoms trapped in the quadrupole magnetic trap were exposed to a time dependent (amplitude and frequency) rf-field and the cloud shape of the trapped atoms was monitored in a time resolved manner while frequency and amplitude of the rf-field were varied. It was found that, at a significant field strength of rf-field, the spherical cloud gets transformed into a ring or toroidal shape which finally settles with a radius of ring dependent on the

ent Zeeman hyperfine sub-levels and induce transitions among them. The interaction of an atom with the static and time varying rf-field has been considered in the dressed state framework and the resulting potential energy landscapes were found to be exquisite as well as time independent in the rotating wave approximation. The formalism used have reproduced the potentials, like double wells and ring trap potentials, which were obtained previously by other groups. In addition, new types of potentials have been predicted which include asymmetric, rotating and oscillating ring traps [15]. These rotating traps are promising for investigating novel physical phenomenons as well as having practical utilization for realizing an atom gyroscopes.

Chapter 3 describes the details of the experimental setup using which the experiments have been performed to realize our predicted rf-dressed potentials. In this setup, a vapor chamber MOT (VC-MOT) of ^{87}Rb atoms is formed in a chamber at a pressure of $\sim 1 \times 10^{-8}$ mbar and an ultra-high vacuum MOT (UHV-MOT) is formed in a glass cell at a pressure of $\sim 5 \times 10^{-11}$ mbar. The atom cloud in the VC-MOT works as a source of atoms to load the UHV-MOT. The UHV-MOT was loaded by using a push beam focused on the VC-MOT atom cloud.

The chapter also describes the use of several acousto-optic modulators (AOMs) for the control over the duration of laser beams as well as for the shifting of frequency of the laser beams. The rf sources for dressing and evaporative cooling were assembled in-house using a commercial rf-synthesizer coupled to a broadband rf-amplifier. The output of the amplifier was con-

these rf-dressed potentials. The work is then performed to use a polychromatic rf-field instead of a monochromatic rf-field, for rf-dressing of atomic states in the magnetic trap and investigate the modifications in the obtained rf-dressed potentials. A many mode Floquet theory (MMFT) has been implemented to study the atom field interaction using the polychromatic rf-field. The results have shown that rf-dressed potentials with polychromatic rf-field can have lattice like spatial periodic structure. It is also shown theoretically that single and two photon transition probabilities for an atom exposed to polychromatic rf-field can be very large.

This thesis is organized in six chapters whose brief description is as follows.

In **Chapter 1**, the fundamentals of interaction of light with atoms have been discussed. These discussions are extended to case of a moving atom interacting with a frequency detuned laser beam to understand the basic principles of laser atom cooling techniques. The basic working principle of quadrupole magnetic traps, quadrupole Ioffe traps and forced evaporative cooling in these traps using a radio frequency field has also been described. These fundamental techniques were utilized in the experiments to obtain the cold atom cloud with temperatures in the range of few tens to hundreds of micro Kelvin for the experimental work presented in the thesis.

Chapter 2 provides theoretical background for the generation and manipulation of radio frequency dressed potentials. In presence of a static quadrupole magnetic trap, an appropriately chosen rf-field can couple differ-

radio frequency (rf) dressed potentials, first proposed theoretically by Zobay and Garaway [13] and later demonstrated experimentally by several groups [14, 4] are considered to be an excellent choice. The rf-dressed potentials are formed by superposing an oscillating rf-field over the static magnetic trap field. By varying the frequency, amplitude and polarization of the applied rf-field, a number of different potentials can be generated.

In this thesis work, we have predicted a number of new type of rf-dressed potentials using a static quadrupole magnetic field and rf-fields with different polarizations, phases and magnitude. These potentials can provide a variety of atom trapping geometries which can be useful for various applications of cold atoms in basic science and device development. To begin with, we took the static magnetic quadrupole trap and a single frequency rf-field to generate rf-dressed potentials. In this study, we have predicted various symmetric and asymmetric potential landscapes for atom having static and rotating configurations [15]. Later, we have performed experiments to realize the trapping of cold atoms in the symmetric and asymmetric ring / toroid shaped geometries, using cold ^{87}Rb atoms trapped in a quadrupole magnetic trap and exposed to the rf-fields of different polarizations [16]. The trapped ring shaped atom cloud radius was dependent on the applied rf-field frequency. Studies have been further performed to understand the time evolution of cold atoms in rf-dressed potential and corresponding evolution in the shape of atom cloud, as amplitude and frequency of the dressing rf-field was varied. This shred light in the associated decay mechanisms and Landau-Zener transitions in

the existing state-of-the-art devices. In all above applications, there exists the requirement to further improve the ability to trap and manipulate cold atoms.

The manipulation of neutral atoms using magnetic field was first demonstrated by Stern and Gerlach in their famous experiment [12]. But, due to the weak magnetic dipole moment of neutral atoms, trapping of atoms solely based on magnetic field requires low temperature of atom cloud and a strong magnetic field gradient of the order of hundreds of Gauss per cm. The simplest and very popular magnetic trap for neutral atoms is a quadrupole trap generated using a pair of coils in anti-Helmholtz configuration. The trap centre in the quadrupole trap has zero of magnetic field, which results in a loss mechanism known as 'Majorana loss'. This loss mechanism is so dominant at low temperatures that it hinders to reach the quantum degeneracy, called Bose Einstein Condensation (BEC). To overcome this, other magnetic trap configurations, though difficult to realize, are used to obtain a trap minimum with non-zero magnetic field. The basic limitation with the atom traps using static magnetic field comes from the Maxwell's equations and Earnshaw's theorem, which suggest that static macroscopic magnetic traps can have only one minimum, with no scope to generate a landscape having multiple magnetic field minima and maxima. On the other hand, the urge to realize a potential landscape which can be tailored, is growing continuously due to several upcoming applications of cold atoms as discussed before. To cater this need for tailored potential landscapes for atoms, the



Homi Bhabha National Institute

SYNOPSIS OF Ph. D. THESIS

1. **Name of the Student: Arijit Chakraborty**
2. **Name of the Constituent Institution: Raja Ramanna Centre for Advanced Technology, Indore**
3. **Enrolment No. : PHYS03201204016**
4. **Title of the Thesis: Studies on radio frequency dressed potentials for cold atoms**
5. **Board of Studies: Physical Sciences**

SYNOPSIS

Over the past few decades, the field of cold atoms has made a tremendous progress in various fronts. With the advent of atom cooling and trapping techniques, the phenomenal developments in ultra-precision spectroscopy [1], ultra-cold collisions [2], quantum optics [3], matter wave optics [4], degenerate gases [5], tunneling [6], super-fluidity and Josephson oscillations [7] etc have taken place. The applications of cold atoms in measurement devices are also fast upcoming which include atomic and optical clocks [8], atom interferometer [9], atomic gravimeter [10], atomic magneto-meter [11], etc . These cold atoms based devices are expected to provide accuracy better than

5.13 Single (black) and two (red) photon transition probability as a function of Rabi frequency $\Omega_0/2\pi$. The solid lines are linear fit to the logarithmic variation. The inset shows a sharp dip in the transition probabilities which is due to the splitting of the avoided crossings. 107

5.14 Variation of the single (black curve) and two (red curve) photon transition probabilities as a function of the separation frequency ω_r at the central resonance $\xi = 0$. The inset shows the width (Δ) of the single photon transition probability lobe as a function of the separation frequency ω_r. In the inset, circles, squares and triangles denote the width of the central, left and right lobes in the transition probability. The solid lines depict the linear fit. 107

5.8 Eigen-energy levels as a function of the dimensionless scale ξ for three different sub-manifolds (*i.e.* $m = 0, \pm 1$) of the first FBZ (*i.e.* $n = 0$). The black curves corresponds to eigen-energies for $\Omega_0 = 2\pi \times 2$ kHz and the red curves corresponds for $\Omega_0 = 2\pi \times 400$ kHz. 100

5.9 Variation in the minima positions as a function of the coupling strength $\Omega_0/2\pi$. At the crossing coupling strength Ω_0^c, the single minimum splits in to two minimas asymmetrically. The inset shows the spatial variation of the eigen-energies ϵ as a function of ξ, showing the splitting of the secondary avoided crossing formed at the 2.5 μK at $\xi = 0$. The dashed and the solid curve shows the eigen-energies at $\Omega_0 = 2\pi \times 0.75$ MHz and $\Omega_0 = 2\pi \times 1.0$ MHz respectively. 101

5.10 Variation in the depth of the calculated trapping potential for different field strength. The hollow markers (circle, square and triangle) shows the obtained numerical values whereas the solid curves denote the analytical fitting using Eq. (5.32). The dashed curve corresponds to a parabolic fit to the eigen-energy variation for $B_0^x = 1$ G. The other parameters are $\omega_0 = 2\pi \times 2$ MHz, $B_0^y = B_0^z = 0$, $B_q = 100\ G\ cm^{-1}$, $N_o = 5$ and $N = 4$. . . 102

5.11 (a) Variation in position of local eigen-energy minimum ξ_m^k (ξ_m^{-3} and ξ_m^{-4}) as a function of ω_r. The dashed lines show the lower and upper ends of ξ_m^k values. (b) Variation in the separation between the terminal frequencies (ω_r^t), *i.e.* $\Delta\omega_r^t$, as a function of the separation frequency ω_r (open square). The continuous line is a linear fit. The other parameters are $\omega_0 = 2\pi \times$ 2 MHz, $B_0^x = 1$ G, $B_0^y = B_0^z = 0$ and $B_q = 100\ G\ cm^{-1}$, $N_o = 5$, $N = 4$. 104

5.12 Transition probabilities $\bar{P}_{\alpha\to\beta}$ normalized by the off resonant transition probability $\bar{P}^{(0)}_{\alpha\to\beta}$ for different rf-field strengths : (a) B_0^x=10 mG, (b) B_0^x=50 mG, (c) B_0^x=0.1 G, (d) B_0^x=0.5 G, (e) B_0^x=1 G, (f) B_0^x=5 G. Here, $B_0^y = B_0^z = 0$, $\omega_0 = 2\pi \times$ 2 MHz, $\omega_r = 2\pi \times$ 100 kHz, $B_q = 100\ G\ cm^{-1}$, $N_o = 5$. . . 106

5.3 Dimensionless quality parameter ζ for equally strong rf-fields (*i.e.* $|\Omega_0|^2 = |\Omega_1|^2$) as a function of relative frequency separation $\Delta\omega/\omega_0$ in the LRM approach. The inset shows the magnified plot of a particular region with (continuous curve) and without (hollow circles) considering the stark shifts $\Gamma(\mathbf{r})$ due to the off-resonant rf-fields. Here $\omega_0 = 2\pi \times 2$ MHz, $B_0^x = 1$ G, $B_0^y = B_0^z = 0$ and $B_1^x = 1$ G, $B_1^y = B_1^z = 0$, $B_q = 100\ Gcm^{-1}$. 93

5.4 Calculated energy difference ($\Delta\epsilon_0$) between the RWDS and MMFT methods as a function of truncation order N_o in the infinite matrix $\mathbb{H}^F_{\omega_0}$ for two different values of detuning values δ_0 ($r = 0\ \mu m$) and δ_0 ($r = 40\ \mu m$). The saturation of energy difference above $N_o = 3$ provides the minimum order of truncation to be used is $N_o > 3$. The other parameters are $\omega_0 = 2\pi \times 2$ MHz, $B_0^x = 1$ G, $B_0^y = B_0^z = 0$, $B_q = 100\ G\ cm^{-1}$. 94

5.5 Calculated convergence of relative error (*i.e.* $(\epsilon_{N_0+1} - \epsilon_{N_0})/\epsilon_{N_0}$) of the infinite matrix $\mathbb{H}^F_{\omega_0}$ as a function of the truncation order at off-resonant detuning δ_0 ($r = 40\ \mu m$). The other parameters are $\omega_0 = 2\pi \times 2$ MHz, $B_0^x = 1$ G, $B_0^y = B_0^z = 0$, $B_q = 100\ G\ cm^{-1}$. 95

5.6 Spatial variation of the quasi-energies as a function of the dimensionless scale ξ are plotted for the Floquet manifolds $n = 0, \pm 1$ (a); and the submanifolds $m = 0, \pm 1$ for n=0 (b). 97

5.7 (a) Variation in eigen-energies (ϵ) as a function of dimensionless parameter $\xi = (\omega_L - \omega_0)/\omega_r$ for $N = 4$. Here, ξ_m^k correspond the eigen-energy minimum for the kth component of the rf-field. (b) Time averaged transition probabilities $\left(\bar{P}_{\alpha\to\beta}\right)$ between the $|0\rangle$ and $|\pm 1\rangle$, $|\pm 2\rangle$ states as a function of ξ. The other parameters are $\omega_0 = 2\pi \times 2$ MHz, $\omega_r = 2\pi \times 100$ kHz and $B_0^x = 1$ G, $B_0^y = B_0^z = 0$, $B_q = 100\ G\ cm^{-1}$, $N_o = 5$. 98

4.7 The experimentally measured variation in number of atoms (circles) in the trapped cloud with time when frequency of dressing rf-field was varied from 15 MHz to 1 MHz in 1 sec duration. The continuous curve is exponential fit to the data and guide to eyes. The inset shows a similar variation obtained from simulations for $N_0 = 1 \times 10^5$ atoms. 76

4.8 Measured variation in number of atoms with holding time. Circles show number of atoms trapped in the rf-dressed quadrupole trap and crosses show number of atoms trapped in the bare quadrupole trap. Error bars are shown for some data points generated after repeated measurements. The continuous curves are to guide eyes. 77

5.1 Comparison of the MMFT and RWDS method for an atom interacting with a single frequency rf-field. (a) Variation of eigen-energies (ϵ_0) for different Zeeman hyperfine sub-levels as a function of δ_0, using the RWDS and MMFT (for truncation order $N_o = 5$). (b) Difference ($\Delta\epsilon_0$) between the energy values predicted by MMFT and RWDS approaches as a function of δ_0. The other parameters used are $\omega_0 = 2\pi \times 2$ MHz, $B_0^x = 1$ G, $B_0^y = B_0^z = 0$, $B_q = 100\, G\, cm^{-1}$. 89

5.2 Relative shift in energy $(\Delta\epsilon/\epsilon)_{0,1}$ as a function of the relative strength (Ω_1/Ω_0). In the inset, eigen-energies ($\epsilon_{0,1}$) obtained from the RWDS (dashed curve) and the MMFT (solid curve) for relative strength $\Omega_1/\Omega_0 = 0.1$ are shown as a function of detuning δ_0. The other parameters are $\omega_0 = 2\pi \times 2$ MHz, $\omega_1 = 2\pi \times 2.2$ MHz, $B_0^x = 1$ G, $B_0^y = B_0^z = 0$, $B_q = 100\, G\, cm^{-1}$, $N_o = 5$. 91

4.3 Observed variation in the ring radius with time during the evolution of the dressing rf-field. Points show the experimentally measured values and the error bars show the deviation in the value in repeated measurements. The solid line represents the linear fit whereas the dahsed line shows the steady state theoretical values of radius. The inset shows the absorption images (optical density) of the atom cloud at different times of evolution. . 72

4.4 The measured variation in number of atoms (dark circles) in a trapped cloud during the rf-field ramp from 15 MHz to 1 MHz in 5 sec duration. The initial faster decay of number of atoms in the trap bears the signature of the rf induced forced evaporation, whereas the slow variation at the trailing edge shows the trapping of atoms in the rf-dressed potential with lower losses. The continuous curve shows the exponential decay in number of atoms. The inset shows the magnified view of the evolution of number of atoms in the rf-dressed ring potential. 73

4.5 Simulated atom cloud pictures at different instants of time during the rf-frequency ramp from 15 MHz to 1 MHz in 5 sec. The simulation results are for initial number of atoms 5×10^4 at temperature 200 μK in quadrupole trap. The blue colour dots represent particles in the $|m_F = -2\rangle_A$ state and red dots represent particles in $|m_F = 2\rangle_A$ state. The ring with red dots indicates the cloud trapped in the toroidal geometry. Figures (a) to (c) show the simulated cloud shapes as frequency ramp progresses. . 74

4.6 Results of numerical simulations showing the variation in number of atoms with time during the ramp down of rf-field frequency. The curves (a), (c) and (e) show results of simulations for initial number N_0=1×10^6, whereas (b), (d) and (f) show the results for 1×10^5. The curves (c) and (d) show number of atoms in $|m_F = -2\rangle_A$ state whereas (e) and (f) show atom numbers in $|m_F = 2\rangle_A$ state. The inset shows the magnified view of the evolution of number of atoms in different states. 75

3.6 Variation in the rf-coupling strength (*i.e.* the peak Rabi frequency, $\Omega_0 = (g_F\mu_B/\hbar)|B^{rf}|$) with frequency, during the frequency variation in the rf-field ramp. The circles show the experimental data and continuous curve shows an exponential fit. The error-bars show the standard deviation between multiple experimental observations. 60

3.7 (a) The absorption image of the cloud after evaporative cooling and rf-dressing using the multi-turn coil (frequency of the rf-field is ramped down from 15 MHz to 1 MHz). (b) The absorption image of the cloud when both the single and multi turn coils are simultaneously used with frequency of the rf-field ramped down from 15 MHz to 1 MHz. The image shows the formation of asymmetric ring traps with two rf-fields of different polarizations. The curves show the variation of optical density in the images across the horizontal and vertical diameters. 62

3.8 (a) Absorption images of the atom cloud in a ring trap formed by a single rf-field of frequency $\omega_0 = 2\pi \times 1.5$ MHz. (b) and (c) shows absorption images while applying a second weak rf-field of frequency $\omega_1 = 2\pi \times 1$ MHz. The central cloud is trapped in the $|F = 2, m_F = -2\rangle_A$ state while the concentric ring cloud is in state $|F = 2, m_F = 2\rangle_A$. 63

4.1 Two dimensional representation of the DSMC scheme. The dots represent the atoms with the histograms showing the number of occurrence of atoms in a specific spatial bin. Here h_x and h_y denotes the cell width and height respectively. 67

4.2 Experimentally observed absorption images of the cold atom cloud at different instants of time after starting the ramp of the rf-field : (a) t = 0.5 sec, (b) t = 1.0 sec, (c) t = 1.5 sec, (d) t = 2.0 sec, (e) t = 2.5 sec, (f) t = 3.0 sec, (g) t = 3.5 sec, (h) t = 4.0 sec, (i) t = 4.5 sec, (j) t = 5.0 sec. The colours from blue to red in all the images show optical density in increasing order. 71

2.5 Contours of rf-dressed potential of Eq. (2.44) with $B_q = 100\ Gcm^{-1}$, $\omega_0 = 2\pi \times 1.5$ MHz,$B_0^x = B_0^y = 700\ mG$, $B_0^z = 500\ mG$ and $\omega_m = 2\pi \times 1$ Hz for different values of time t. 43

3.1 Schematic diagram of the experimental setup. 47

3.2 Experimental pulse sequences. A: MOT operation; B: Compressed-MOT operation; C: Optical molasses formation; D: Optical pumping operation; E: Quadrupole trap initialization; F: Quadrupole trap ramping; G: Quadrupole equilibration; H: RF coupling. 54

3.3 Schematic diagram of the magnetic and radio frequency coils setup, QC-2: quadrupole coil for UHV- MOT, PBS: polarising beam splitter cube, CCD: charge coupled device camera, LA-1: multi-turn loop antenna for rf-dressing, LA-2: the loop antenna used for rf radiation, LA-3: pick-up loop antenna, AP: absorption probe beam. The absorption imaging optics is shown in the diagram. The coordinate axes (x, y, z) are also shown. . . 57

3.4 Observed absorption images of the cloud (in xy-plane) after evaporative cooling in quadrupole trap: (a) before rf-dressing and (b) after rf-dressing. The curves show the profiles of optical density along the selected diameters across the image. Different colours in an absorption image from blue to red represent the optical density values in the increasing order. 58

3.5 Observed variation in the ring radius with frequency ($\omega_0/2\pi$) of the dressing rf-field. Points show the experimentally measured values and the error bars show the deviation in the value in repeated measurements. The line curve represents the theoretical prediction of radius considering experimental parameters. The inset shows the absorption images (optical density) of the atom cloud for different frequencies of dressing field. . . . 59

1.4 Schematic diagram of magneto optical trapping (MOT) mechanism. The red arrows are the laser radiations of opposite circular polarizations. The magnetic field strength is depicted with the background color gradient. The movement of the atom in either direction reduces the effective detuning between the ground and the excited states and hence increases the force exerted on the atom. This position dependent force facilitates the trapping mechanism. 14

1.5 Schematic diagram of magnetic trapping and evaporative cooling using radio frequency radiation. The red dots represent the atoms whereas the black lines shows the spatial variation of the different Zeeman hyperfine magnetic sub levels. The trappable zeeman hyperfine states get converted upon being coupled using the rf-field and the modified states have position dependent trapping capabilities. Atoms outside the inflection point get removed, thereby reducing the average temperature of the atom clod. . . . 17

2.1 Contours of rf-dressed potential with $B_q = 100\, Gcm^{-1}$, $\omega_0 = 2\pi\times 1.5$ MHz for: (a) double well potential of Eq. (2.31) with $B_0^x = 700\, mG$ and $B_0^y = 0$, (b) split arc potential of Eq. (2.32) with $B_0^x = 700\, mG$ and $B_0^y = 350\, mG$ and (c) ring potential of Eq. (2.34) with $B_0^x = B_0^y = 700\, mG$. 34

2.2 Contours of rf-dressed potential of Eq. (2.36) with $B_q = 100\ Gcm^{-1}$, $\omega_0 = 2\pi \times 1.5$ MHz, $B_0^x = 700\, mG$, $B_0^y = 350\, mG$ and for: (a) $B_0^z = 0\, mG$, (b) $B_0^z = 100\, mG$ (c) $B_0^z = 200\, mG$. 36

2.3 Contours of rf-dressed potential of Eq. (2.38) with $B_q = 100\, Gcm^{-1}$, $\omega_0 = 2\pi \times 1.5$ MHz,$B_0^x = B_0^y = 700\, mG$ for: (a) $B_0^z = 0\, mG$, (b) $B_0^z = 300\, mG$ (c) $B_0^z = 500\, mG$. 37

2.4 Contours of rf-dressed potential of Eq. (2.41) with $B_q = 100\ Gcm^{-1}$, $\omega_0 = 2\pi \times 1.5$ MHz,$B_0^x = B_0^y = 700\, mG$, $B_0^z = 500\, mG$ and $\omega_l = 2\pi \times 1$ Hz for different values of time t. 40

List of Figures

1.1 D2 line transition in ^{87}Rb level scheme. The red arrows show the stimulated absorption of laser radiation from the ground state to the excited states. The blue arrows mark the spontaneous decay of atoms from the excited state to the ground states. $\Gamma = 2\pi \times 6$ MHz is the spontaneous decay rate which also marks the linewidth of the excited states. 8

1.2 Schematic diagram of the Doppler cooling method. The red arrows show the laser radiations of frequency ω, red detuned from the atomic transition frequency ω_0. Due to the Doppler effect, laser radiation from the counter propagating direction comes to resonance and drives transition between the ground and excited state. 8

1.3 Schematic diagram of sub-Doppler cooling technique. The superposition of the orthogonal and linearly polarized laser radiations create a periodically varying potential gradient depending on the resultant polarization at any specific point. The atoms looses kinetic energy while climbing the potential hills and then optically pumped back to the valley loosing the acquired potential energy. 11

(MMFT), have been presented. These rf-dressed potentials with polychromatic rf-field have shown a spatially periodic lattice like structure along with high two photon transition rates. Chapter 6 describes the conclusion and future scope of the thesis.

nected via quantum communication networks [28] is one of the many dreams that may come true in not so distant future [29]. Storage and retrieval of quantum informations in ultracold atoms trapped inside magnetic and optical fields is one of the complicated but promising fields in the present scenario [30]. Apart from designing of the quantum devices, research groups all over the worlds are currently in pursuit to realize precision measurement devices [31, 32, 33]. Some of these are among to measure fundamental constants accurately like gravitational constant G and gravitation acceleration g [34]. Sagnac like interferometers based on ultracold atoms [35, 36, 37, 38] to measure rotation have been predicted to be much more sensitive [39] than existing commercial devices. Some of these cold atom based devices have been demonstrated which are getting better day by day. The miniaturized atom cooling and trapping systems [40, 41, 42], also known as atom chips, are more reliable to produce higher maneuverability with smaller power consumptions[43].

Keeping an eye on these current trends and progresses made in the field it is evident that trapping and manipulation of cold atoms is an important issue. This thesis focuses on the generation of radio frequency dressed potentials, in which the ultracold atoms can be trapped and manipulated with much more freedom than that is not possible in the conventional static magnetic traps. In chapter 2, a detailed mathematical description has been provided for the radio frequency dressed potentials. Different types of potential geometries have been obtained using various polarization of the rf-field. Using a phase modulated rf-field, time dependent potentials are also predicted. Chapter 3 focuses on the experimental setup and procedure, using which some of the theoretically predicted rf-dressed potentials have been realized experimentally. The results on observed ring or toroidal trap have also been presented in this chapter. In chapter 4, the results on evolution of the quadrupole trap are presented. Using the direct simulation Monte Carlo method, the evolution is modeled. The time evolution of cold atom cloud after the formation of the dressed trap is also presented. In Chapter 5, results on the rf-dressed trapping potentials with a polychromatic rf-field, studied theoretically using the many mode Floquet theory

variation of the size of the expanding cloud being detected using CCD camera. As the detection techniques are in general invasive in nature, to obtain the complete variation, the release and imaging step requires to be repeated over several times while gradually increasing the time delay between the release and detection stages. The slope from the plot of the squared variation of the dimension of the atom cloud with respect to the squared time interval will then provide the temperature of the atom cloud.

1.5 Remarks

A significant progress has been made in the field of ultracold matter in the recent years due to availability of stable laser sources and efficient power supplies. The initial experiments performed by the atom cooling experts have shown the pathway to realize temperatures in the sub-micro Kelvin regime [8, 9]. These ultra cold matters have proven the existence of another state of matter theoretically proposed much earlier by Bose and Einstein [10, 11], so called Bose Einstein condensate. The realization of the Bose Einstein Condensation [12, 13, 14] in bosonic cold atoms was subsequently followed by observations of degenerate Fermi gases [15] in the fermionic counterparts of the bosonic atoms. Experimental observations of these degenerate states ignited a quest [16] to understand the quantum world using our classical minds. These ultra cold atomic systems offered the ultimate toolbox to create a quantum simulator hitherto unknown to the world of physics[17, 18]. The example of which includes optical lattices to mimic the periodic potential structure often found in condensed matters [19, 20],tunneling between Josephson junctions [21], self-trapping [22], Mott insulators [23]. The mimicking of the condensed matter systems with ultracold atoms has shown a path to incur new understanding in the field of high temperature superconductivity with the BEC-BCS cross-overs in fermionic atoms [24].

Another field in which the ultracold atoms are making an impact is the quantum information processing [25]. The realization of a quantum computation devices [26, 27] con-

a phase shift in the non-diffracted plane wave while detcting both the diffracted and the non-diffracted beams in a ccd camera. However, this technique has not been used in this thesis work [7].

1.4.4 Measurement of temperature of atom cloud

The temperature of a cold atom cloud in principle can be measured by using the free expansion technique. To understand this technique let us consider an initial atom cloud with a spatial density of Gaussian distribution trapped in a harmonic trap in such a way that the initial phase space density relative to the center of the atom cloud is given by,

$$\rho(\mathbf{r}_0, \mathbf{p}) \propto \prod_{i=x,y,z} \exp\left(-\frac{p_i^2}{2mk_BT}\right)\exp\left(-\frac{m\omega_i^2 r_{0i}^2}{2k_BT}\right), \tag{1.48}$$

where ω_i are the trap frequencies of the harmonic trap, k_B is the Boltzmann constant, m is the mass of the atoms and T is the temperature of the atom cloud. The density distribution after the removal of the harmonic trap after a time t is given by the convolution,

$$n(\mathbf{r}, t) = \int\int d^3\mathbf{r}_0 d^3\mathbf{p}\rho(\mathbf{r}_0, \mathbf{p})\delta\left(\mathbf{r} - \mathbf{r}_0 - \frac{\mathbf{p}t}{m}\right). \tag{1.49}$$

A simple integration over the complete momentum and position space reveals the density being given as,

$$n(\mathbf{r}, t) \propto \prod_{i=x,y,z} \exp\left(-\frac{r_i^2}{\omega_i^2(t)}\right), \tag{1.50}$$

where

$$\omega_i^2(t) = \omega_{i0}^2 + \frac{2k_BT}{m}t^2, \tag{1.51}$$

with

$$\omega_{i0} = \frac{2k_BT}{m\omega_i^2}. \tag{1.52}$$

To implement this technique, it is required to release the trapped atom cloud and the

1.4.2 Fluorescence imaging of the cold atom cloud

The fluoresence imaging technique works in a different manner than the absorption imaging technique. In this method a resonant light beam is shone on the atom cloud and the scattering of photons from this light beam is detected using a CCD camera module. Contrary to the absorption probe imaging only two images require to be captured in this technique. One with the atom cloud and another one without it to consider the background noise. The deduction of the later from the former one can give one an image of the atom cloud. The determination of the number of trapped atoms from this image is rather tricky as compared to its absorption imaging counterpart. The number of trapped atoms can be found in terms of the count of the CCD camera N_c as,

$$N = \frac{4\pi\left[1 + \left(\frac{2\delta}{\Gamma}\right)^2 + \frac{6I_0}{I_s}\right]}{3\Gamma t_e \eta \frac{I_0}{I_s} d\Omega} N_c, \tag{1.47}$$

where δ is the detuning of the fluoresence probe beam, Γ is the decay rate of the hyperfine level in interest, I_0 is the intensity of fluoresence probe beam, I_s is the saturation intensity, t_e is the exposure time during which photons are collected in the CCD camera, $d\Omega$ is the solid angle subtended by the CCD camera in which the photon collection occurred and η is the quantum efficiency of the CCD camera.

1.4.3 Phase contrast imaging of the cold atom cloud

Both the imaging techniques described earlier relies on the resonant interaction of a laser beam with the trapped atom cloud, resulting in a destruction of the atom cloud while imaging. The phase contrast imaging technique, in which the trapped atom cloud interact with a far detuned probe laser beam, is minimally destructive and allows obtaining phase information imparted on the probe beam by the atom cloud. In this imaging technique a phase spot, a small transparent object, is inserted in the probe beam path to introduce

1.4 Characterization of cold atom clouds

To characterize an atom cloud, a number of different techniques and methods exist, of which the most prominent three are discussed below. These techniques allow the determination of number of trapped atoms in the cloud along with the temperature of the atom cloud.

1.4.1 Absorption imaging of the cold atom cloud

The absorption probe imaging works exactly the same way a semi-opaque object cast a shadow to a screen when illuminated by a light beam. To capture a single absorption image of the cloud a CCD camera module is required to be triggered three times to capture three different type of images. The first image (I) is the absorption image containing the cloud and the absorption probe beam. The second image (I^0) does not contain any cloud, rather the effect of the absorption probe beam is recorded. The third image (I^{bg}) is taken as a background image contains neither the cloud nor the absorption beam. With the use of these three images a two dimensional density profile (column density) of the atom cloud is generated using the relation,

$$OD_{i,j} = -\log\left(\frac{I_{i,j} - I^{bg}_{i,j}}{I^{0}_{i,j} - I^{bg}_{i,j}}\right), \tag{1.45}$$

where i, j are the pixel indices in the CCD camera. Using the above equation, integrated column density for all the pixels of the CCD camera is obtained which finally results in the determination of the number of atoms trapped in the cloud by,

$$N = \frac{A}{\sigma}\sum_{i,j} OD_{i,j}\,, \tag{1.46}$$

where σ is the absorption cross section of the atoms at the probe wavelength and A is the area of an individual pixel.

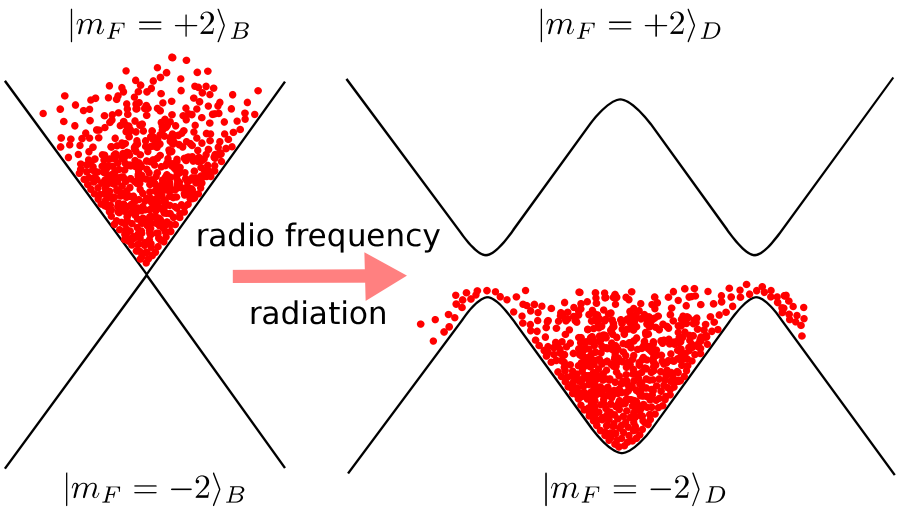

Figure 1.5: Schematic diagram of magnetic trapping and evaporative cooling using radio frequency radiation. The red dots represent the atoms whereas the black lines shows the spatial variation of the different Zeeman hyperfine magnetic sub levels. The trappable zeeman hyperfine states get converted upon being coupled using the rf-field and the modified states have position dependent trapping capabilities. Atoms outside the inflection point get removed, thereby reducing the average temperature of the atom clod.

energy is higher than the average kinetic energy or the temperature of the atom cloud. Use of a continually decreasing frequency of the rf-field, atoms with more lower velocities can be removed from the ensemble to reduce the final temperature below an arbitrary temperature value. The physics behind the forced rf-evaporation has been studied in the sufficiently ergodic regimes using both classical and quantum kinetic theory, in which a truncated Boltzmann distribution of the phase space has been considered [5, 6].

This cooling mechanism works well only in case of atom clouds where the initial number of atoms trapped in the atom cloud is much higher so that after a significant reduction during the cooling process, a sizable portion of the initial atoms remains trapped in the magnetic trap to be described statistically.

The simplest of the magnetic trapping geometry possible is the quadrupole trap, having the radial field gradient as B_q, in which the magnetic field varies as a function of the spatial coordinates as [4],

$$\mathbf{B}(\mathbf{r}) = B_q \left[x\hat{\mathbf{x}} + y\hat{\mathbf{y}} - 2z\hat{\mathbf{z}}\right] \tag{1.43}$$

obeying the maxwell's equation $\boldsymbol{\nabla}.\mathbf{B} = 0$ by satisfying,

$$\hat{x}\frac{\partial \mathbf{B}}{\partial x} = \hat{y}\frac{\partial \mathbf{B}}{\partial y} = -\frac{1}{2}\hat{z}\frac{\partial \mathbf{B}}{\partial z}. \tag{1.44}$$

Despite the advantages of the easier implementation methods, the quadrupole trap suffers from a severe drawback when it comes to trap ultra-cold atoms. Atom in the close vicinity of the trap minimum experiences transitions to spin states other than the trappable ones and fly out of the trap. These transitions, named as the Majorana transitions, are detrimental for realization of Bose Einstein condensation in quadrupole traps, which requires high density of atoms beside the lower temperature.

To remedy these losses a number of modifications has been made in magnetic traps like Ioffe Prichard trap (IP), Quadrupole Ioffe trap (QUIC), Time orbiting potential trap (TOP), optically plugged quadrupole trap, laser dipole trap and hybrid quadrupole trap.

1.3.5 Evaporative cooling

The state selective trapping obtained in the magnetic traps can be exploited to reduce the temperature of the trapped atom cloud further by removing hotter atoms selectively. As the separation between the Zeeman hyperfine states of the atoms varies spatially due to the position dependent inhomogeneous magnetic field, an rf-radiation of a particular frequency and narrow line width can be utilized to excite atoms from trappable to untrappable states. The rf-field frequency is chosen in such a way that the atoms undergoing transitions have velocities higher than the average velocity of the atomic distribution in the cloud. Hence, with every atom removed from the ensemble the reduction in kinetic

cooled atoms to other traps relying on either pure reactive force of light beams or intrinsic magnetic moment of the atoms in presence of a magnetic field. In the next section, the basic principles of all magnetic trapping is described.

1.3.4 Magnetic trapping of atoms

Magnetic trapping of neutral atoms is based on the interaction of the magnetic moment of the atoms $\boldsymbol{\mu}$ with a spatially varying magnetic field $\mathbf{B}(\mathbf{r})$ described by the interaction Hamiltonian,

$$H_B = -\boldsymbol{\mu}.\mathbf{B}(\mathbf{r}), \tag{1.39}$$

where the magnetic moment can be written as,

$$\boldsymbol{\mu} = -\frac{g_F \mu_B}{\hbar}\mathbf{F}. \tag{1.40}$$

Here $\mu_B = e\hbar/2m_e$ is the Bohr magnetron and $\mathbf{F}$ is the total angular momentum of the atom. The Lande g-factor g_F can be written in terms of the nuclear spin I and total angular momentum F as,

$$g_F = \frac{F(F+1) - I(I+1) + \frac{3}{4}}{F(F+1)}. \tag{1.41}$$

Hence Eq. (1.39) can be written in terms of the projection of the total angular momentum m_F as,

$$H_B = g_F m_F \mu_B \mathbf{B}(\mathbf{r}). \tag{1.42}$$

According to Maxwell's equations of classical electrodynamics, only magnetic field minimum are possible to create in a source free region in space. Hence to trap atoms with spatially varying magnetic fields, the product of the Lande g factor (g_F) and Zeeman hyperfine magnetic quantum number (m_F) should be greater than zero. States for which this criterion is satisfied, in general called *low field seeking states*.

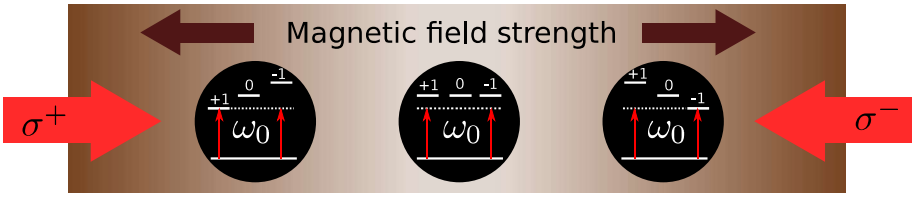

Figure 1.4: Schematic diagram of magneto optical trapping (MOT) mechanism. The red arrows are the laser radiations of opposite circular polarizations. The magnetic field strength is depicted with the background color gradient. The movement of the atom in either direction reduces the effective detuning between the ground and the excited states and hence increases the force exerted on the atom. This position dependent force facilitates the trapping mechanism.

In the limit $\mathbf{k}.\mathbf{v} \to 0$ and $\beta z \to 0$, the above expression reduces to,

$$\begin{aligned} F &\simeq 2\hbar k\Gamma\Omega^2 \frac{\delta(k.v + \beta z)}{[\delta^2 + (\Gamma/2)^2]^2} \\ &= -\eta v - m\omega_{trap}^2 z \end{aligned} \tag{1.35}$$

where η is a similar friction coefficient as obtained in the Doppler force and ω_{trap} is the frequency of harmonic confinement of the atoms around the trap center obeying the differential equation,

$$\frac{d^2z}{dt^2} + \frac{\eta}{m}\frac{dz}{dt} + \omega_{trap}^2 z = 0 \tag{1.36}$$

The explicit expressions for two parameters is given by,

$$\eta = 4\hbar k^2\Omega^2 \frac{|\delta|\Gamma/2}{[\delta^2 + (\Gamma/2)^2]^2}, \tag{1.37}$$

and

$$\omega_{trap}^2 = 2\hbar k\Gamma\Omega^2 \frac{|\delta|\beta}{m[\delta^2 + (\Gamma/2)^2]^2}. \tag{1.38}$$

Using three pairs of beams with circularly polarized σ^+ and σ^- combination, atoms can be trapped using the harmonic force experienced by them near the trap minimum. But neither the realizable atomic number density nor the temperature in this trap is suitable to achieve the quantum degenerate regime. Hence this trap acts as an initial step to load pre-

to the spontaneous emission of a single photon, this cooling mechanism cease to exist. So, the final temperature can not be lower than the recoil temperature $T_R = \hbar^2 k^2/2M$ in this method.

1.3.3 Magneto Optical Trap

The cooling mechanisms discussed in the previous section can reduce the temperature of the atoms theoretically upto the recoil temperature, but without providing any trapping mechanism whatsoever. The atoms whose movement are not axially aligned with the laser beams will fly off the interaction regime with out getting decelerated enough and the collision with the incoming atoms from the background will remove the colder atoms very fast. To remedy this situation, a novel trapping mechanism was proposed which relied on the multiplicity of the level structure of the atoms along with the dipole selection rules associated with those levels. In case of an atom with a ground state with angular momentum $J_g = 0$ and a degenerate excited state with $J_e = 1$ having magnetic sub-levels marked by $m_e = 0, \pm 1$, the degeneracy of the excited state can be lifted by applying a spatially linear varying magnetic field of strength βz while applying a pair of circularly polarized beams (*i.e.* σ_+ and $\sigma_$) a trap can be formed. Considering the selection rules associated with the σ_+ and $\sigma_$ transitions, it can be shown that the detuning of both the beams will get modified to $\delta_\pm = \delta \mp \mathbf{k}.\mathbf{v} \mp \beta z$ and the resulting dissipation force of the two beams will become,

$$\begin{aligned} F &= F_{\sigma^+}(\delta_+) + F_{\sigma}\text{-}(\delta_) \\ &= \frac{\hbar k \Gamma \Omega^2}{2} \times \left[\frac{1}{(\delta - \mathbf{k}.\mathbf{v} - \beta z)^2 + (\Gamma/2)^2} - \frac{1}{(\delta + \mathbf{k}.\mathbf{v} + \beta z)^2 + (\Gamma/2)^2} \right]. \end{aligned} \tag{1.34}$$

odically varying polarization can be described as,

$$\begin{aligned} H_{AL} = & \frac{i}{2}\hbar\Omega \sin(kz)\left[|e_{3/2}\rangle\langle g_{1/2}| + \frac{1}{\sqrt{3}}|e_{1/2}\rangle\langle g_{-1/2}|\right]e^{-i\omega t} \\ & + \frac{1}{2}\hbar\Omega \cos(kz)\left[|e_{-3/2}\rangle\langle g_{-1/2}| + \frac{1}{\sqrt{3}}|e_{-1/2}\rangle\langle g_{1/2}|\right]e^{-i\omega t} \\ & + H.c. \end{aligned} \tag{1.30}$$

The reactive force acting on the atoms due to this polarization gradient can be written as a function of the population (density) of the ground and excited states as,

$$\begin{aligned} F_{dipole} = & \frac{\hbar k\Omega}{2}\cos(kz)\left[\langle g_{1/2}|\rho|e_{1/2}\rangle e^{-i\omega t} + \frac{1}{\sqrt{3}}\langle g_{-1/2}|\rho|e_{1/2}\rangle e^{-i\omega t} + c.c.\right] \\ & + \frac{\hbar k\Omega}{2}\sin(kz)\left[\langle g_{-1/2}|\rho|e_{-3/2}\rangle e^{-i\omega t} + \frac{1}{\sqrt{3}}\langle g_{1/2}|\rho|e_{-1/2}\rangle e^{-i\omega t} + c.c.\right] \end{aligned} \tag{1.31}$$

In case lower velocities fulfilling the condition $kv \ll \Gamma$, we can approximate the reactive force as,

$$F_{dipole} = kU_0 \sin(2kz)\left[P_{1/2}(z,t) - P_{-1/2}(z,t)\right] \tag{1.32}$$

with $P_i = |i\rangle\langle i|$ being the projection operator and the potential depth variation of the two ground state levels given as,

$$U_0 = -\frac{2}{3}\hbar\delta\left(\frac{\Omega^2}{\delta^2 + (\Gamma/2)^2}\right) \simeq \frac{2}{3}\left(\frac{\hbar\Omega_0^2}{\delta}\right). \tag{1.33}$$

As the reactive force is proportional to the potential depth U_0, the final temperature achievable by this method relies on the ratio of the coupling strength to the absolute detuning. Hence, at first glance, it may appear that an arbitrary lower value of temperature can be achieved by suitable choosing the detuning and coupling values. The key approximation here is that the change in the kinetic energy of an atom during a complete absorption-emission cycle is small compared to the change in the potential energy. Hence, as soon as the potential energy becomes equal to the change in kinetic energy due

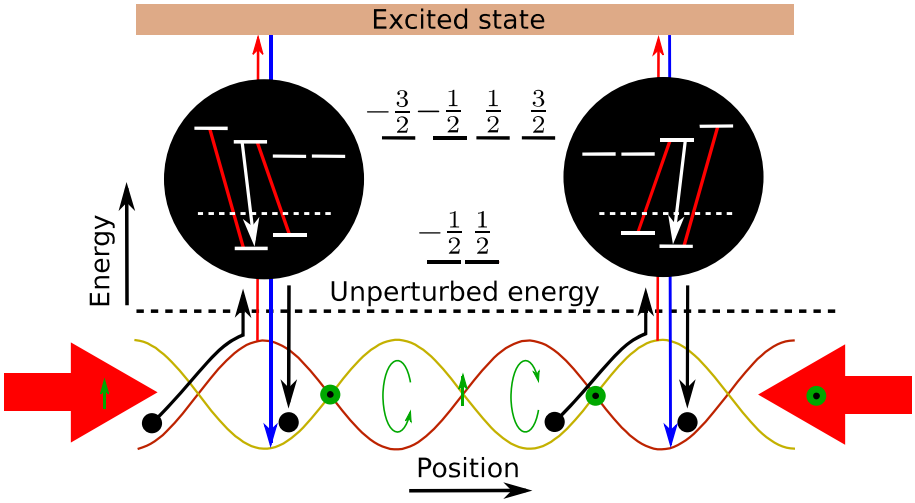

Figure 1.3: Schematic diagram of sub-Doppler cooling technique. The superposition of the orthogonal and linearly polarized laser radiations create a periodically varying potential gradient depending on the resultant polarization at any specific point. The atoms looses kinetic energy while climbing the potential hills and then optically pumped back to the valley loosing the acquired potential energy.

1.3.2 Sub-Doppler cooling of multilevel atoms

The combined electric field of a standing wave designed with two counter propagating laser beams having linear orthogonal polarization can be written as,

$$E(z,t) = \frac{1}{2}\left[\hat{\epsilon}(z)\mathcal{E}e^{-i\omega t} + c.c.\right] \tag{1.27}$$

where

$$\hat{\epsilon}(z) = \hat{\epsilon}_{-}\cos(kz) - i\hat{\epsilon}_{+}\sin(kz) \tag{1.28}$$

and

$$\hat{\epsilon}_{\pm} = \pm\frac{1}{\sqrt{2}}(\hat{\epsilon}_x \mp i\hat{\epsilon}_y) \tag{1.29}$$

The atom light interaction Hamiltonian in case of this electromagnetic field with the peri-

outcome. Due to this frictional force, atoms slow down while maintaining their propagation direction constant. The specific choice of red detuning prevents absorption of light beam from the co-propagating direction, in turn the further acceleration of the atoms. Hence, three orthogonal pairs of counter-propagating red detuned laser beams can slow atoms down in all directions.

From Eq. (1.23), it may appear that by increasing the detuning and Rabi frequency any level of colder temperature can be achieved, but so far we have not considered the effect of spontaneous emissions in the determination of the force. Effect of spontaneous emission generates momentum kicks of magnitude $\hbar k$ over any random direction surrounding the atom. These random momentum kicks result in diffusion of momentum of atoms in phase space consequently heating the atom. Hence, a lower bound for the temperature exists in which the cooling of atoms due to the momentum change balances this heating effect. Further cooling down of atomic sample below this point will not be possible. To determine this temperature, the rate of diffusion of momentum by the random kicks can be calculated and can be expressed in form,

$$\left\langle \frac{\delta p^2}{\delta t} \right\rangle = \frac{\hbar^2 k^2 \Gamma}{2} \left(\frac{s}{1+s} \right) \tag{1.25}$$

Equating this rate with the cooling rate one can obtain the Doppler limit of temperature T_D as,

$$T_D = \frac{\hbar \Gamma}{2k_B} \tag{1.26}$$

with k_B being the Boltzmann's constant and Γ being the spontaneous decay rate of the excited states. This is the lowest temperature achievable in the Doppler cooling method in case of a two level atom. For example, T_D of ^{87}Rb is 140 μK and 240 μK for ^{23}Na atoms. But in real multilevel atoms, a different type of cooling mechanism takes place by which temperatures colder than T_D can be achieved. In the next section this cooling mechanism, also known as sub-Doppler or Sisyphus cooling, is described in detail.

1.3.1 Doppler cooling of atoms and optical molasses

Doppler effect is the modification of the frequency of an electromagnetic field while the detector and/or the source is in motion. This effect has been exploited in the early days of atom cooling to reduce the velocity of the moving atoms while preventing the acceleration in the either direction.

For an atom moving at velocity $\mathbf{v}_0$, the electric field of the laser radiation can be expressed as,

$$\begin{aligned} E_L &= \hat{\epsilon}\mathcal{E}\cos(\omega t - \mathbf{k}.\mathbf{v}_0 t) \\ &= \hat{\epsilon}\mathcal{E}\cos\left[(\omega - \omega_D)t\right] \end{aligned} \tag{1.22}$$

where $\omega_D = \mathbf{k}.\mathbf{v}_0$ is the Doppler frequency.

The dissipative force for this particular velocity group of atoms can be expressed in terms of the Doppler shifted detuning $\delta_D = \omega - \mathbf{k}.\mathbf{v}_0 - \omega_0 = \delta - \omega_D$ as,

$$\begin{aligned} F_{scatter} &= \frac{\hbar k\Gamma}{2}\left(\frac{\Omega^2/2}{\delta_D^2 + (\Gamma/2)^2 + \Omega^2/2}\right), \\ &\simeq F_{scatter}(|\mathbf{v}_0| = 0) - \eta|\mathbf{v}_0|, \end{aligned} \tag{1.23}$$

where the first term is a constant accounting for the standing atoms and the second term is a friction generating force with the friction constant η given as,

$$\eta = -\hbar k^2\Gamma\left[\frac{\delta\Omega^2/2}{\delta^2 + (\Gamma/2)^2 + \Omega^2/2}\right]. \tag{1.24}$$

Utilization of this frictional force can be made with a pair of counter-propagating red detuned laser beam (*i.e.* $\delta < 0$), in which the atoms moving towards the direction of propagation of light percept the frequency of the applied light beam higher than the original frequency due to the Doppler effect. This results in absorption of light by the atoms from the counter propagating direction, consequently experiencing the frictional force as an

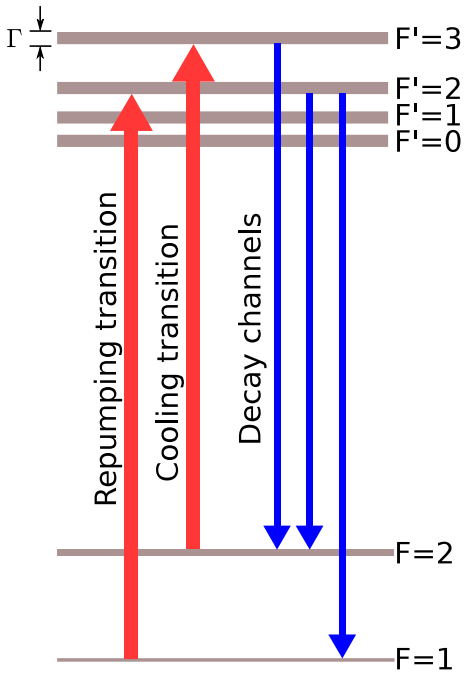

Figure 1.1: D2 line transition in ^{87}Rb level scheme. The red arrows show the stimulated absorption of laser radiation from the ground state to the excited states. The blue arrows mark the spontaneous decay of atoms from the excited state to the ground states. $\Gamma = 2\pi \times 6$ MHz is the spontaneous decay rate which also marks the linewidth of the excited states.

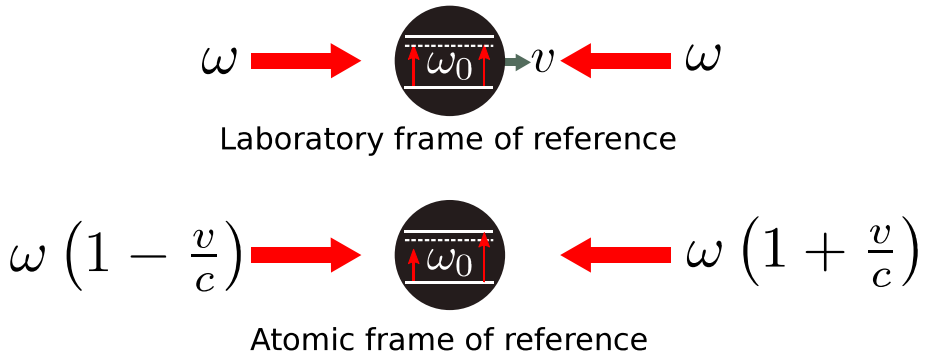

Figure 1.2: Schematic diagram of the Doppler cooling method. The red arrows show the laser radiations of frequency ω, red detuned from the atomic transition frequency ω_0. Due to the Doppler effect, laser radiation from the counter propagating direction comes to resonance and drives transition between the ground and excited state.

Eq. 1.7, we obtain the explicit form of these two component of the light force as,

$$F_{dipole} = -\frac{\hbar\delta}{4}\left(\frac{\nabla\Omega^2}{\delta^2 + (\Gamma/2)^2 + \Omega^2/2}\right), \tag{1.20}$$

$$F_{scatter} = \frac{\hbar k\Gamma}{2}\left(\frac{\Omega^2/2}{\delta^2 + (\Gamma/2)^2 + \Omega^2/2}\right). \tag{1.21}$$

The reactive component of the light force F_{dipole} can be expressed as $F_{dipole} = -\nabla U$ where U is a conservative potential. The origin of F_{dipole} does not involve absorption of field energy and operates on the redistribution of momentum between atom and field modes. On the other hand, the dissipative component of the light force $F_{scatter}$ transfers energy between the atom and the field modes finally saturating at large coupling strength to $F_{scatter} \rightarrow \hbar k\Gamma/2$. This scattering force when applied against the motion of the moving atoms, can be utilized to decrease the velocity or corresponding temperature of a group of atoms. To ensure that only the atoms moving opposite to the direction of the light beams, a specific mechanism is developed, named Doppler cooling method in which the Doppler shift of the frequency of the source beam for a moving atom is exploited.

1.3 Basic cooling and trapping techniques

All the cooling and trapping mechanisms described in this section is valid for all the atomic species commonly used for atom cooling purposes. However, as in our experimental facilities we use ^{87}Rb atoms, examples will include specifications of this particular atomic sample extensively. The level diagram of the ground and excited state of the outer electron of ^{87}Rb is shown in Fig. 1.1.

1.2 Force exerted on atoms by radiation fields

Staring from Plank's, it is well known that photons with a wave vector $\mathbf{k}$ have a momentum of $\hbar k$. By using this momentum imparted by incident photons, laser beams can modify the trajectory of the atoms interacting with these beams. To obtain the time evolution of the momentum operator $\mathbf{p}$, we utilize the Heisenberg equation of motion [3],

$$\begin{aligned}\frac{d\mathbf{p}}{dt} &= \frac{i}{\hbar}[H,\mathbf{p}] \\ &= \frac{i}{2}\left[\Omega(\mathbf{r})\left(e^{-i\phi(r)}e^{-i\omega t}|e\rangle\langle g| + H.c.\right), i\hbar\boldsymbol{\nabla}\right]\end{aligned} \tag{1.17}$$

where the momentum operator $\mathbf{p}$ is replaced with the $\boldsymbol{\nabla}$ operator using the relation $\mathbf{p} = i\hbar\boldsymbol{\nabla}$. The total force exerted on atoms by this change in momentum can be written as,

$$\begin{aligned}F &= \left\langle\frac{d\mathbf{p}}{dt}\right\rangle \\ &= \frac{\hbar}{2}\langle|e\rangle\langle g|\rangle_{internal}\left\langle\nabla\left(\Omega(\mathbf{r})e^{-i\phi(\mathbf{r})}e^{-i\omega t}\right)\right\rangle_{external}.\end{aligned} \tag{1.18}$$

Here the separation of time evolution of internal and external degrees relies on the approximation that the characteristic time scales associated with internal $\left(\Gamma^{-1} \equiv 4\pi\epsilon_0\left(3\hbar c^3/4\omega_0^3 d^2\right)\right)$ and external ($\omega_{rec}^{-1} \equiv 2M/\hbar k^2$) degrees are different in origin and order of magnitude. In case of well localized particles (*i.e.* classical atoms), we can express the final form of the force exerted on the atoms in terms of the steady state Bloch vector components $\mathcal{U}_{st}$ and $\mathcal{V}_{st}$ as,

$$\begin{aligned}F &= -\hbar\Omega(\mathbf{r})\left[\frac{\nabla\Omega(\mathbf{r})}{\Omega(\mathbf{r})}\mathcal{U}_{st} + \nabla\phi(\mathbf{r})\mathcal{V}_{st}\right], \\ &= F_{dipole} + F_{scatter}.\end{aligned} \tag{1.19}$$

Considering the polarization and field amplitude spatially independent (*i.e.* $\hat{\epsilon} \equiv \hat{\epsilon}(\mathbf{r})$ and $\mathcal{E} \equiv \mathcal{E}(\mathbf{r})$) and the phase $\phi(\mathbf{r}) = \mathbf{k}.\mathbf{r}$ in the expression of the electric field of laser given in

$\mathcal{U}, \mathcal{V}, \mathcal{W}$ as,

$$\mathcal{U}(t) = \Re(\tilde{\rho}_{eg} e^{i\phi(\mathbf{r})}), \tag{1.13a}$$

$$\mathcal{V}(t) = -\Im(\tilde{\rho}_{eg} e^{i\phi(\mathbf{r})}), \tag{1.13b}$$

$$\mathcal{W}(t) = \frac{1}{2}\left(\rho_{ee} - \rho_{gg}\right). \tag{1.13c}$$

we obtain the optical Bloch equations in matrix form as,

$$\begin{bmatrix} \dot{\mathcal{U}} \\ \dot{\mathcal{V}} \\ \dot{\mathcal{W}} \end{bmatrix} = \begin{bmatrix} -\Gamma/2 & \delta + \dot{\phi}(r) & 0 \\ -\delta - \dot{\phi}(r) & -\Gamma/2 & -\Omega(r) \\ 0 & \Omega(r) & -\Gamma \end{bmatrix} \begin{bmatrix} \mathcal{U} \\ \mathcal{V} \\ \mathcal{W} \end{bmatrix} - \begin{bmatrix} 0 \\ 0 \\ \Gamma/2 \end{bmatrix}. \tag{1.14}$$

We define the saturation parameter in terms of the detuning δ, Rabi frequency Ω and natural linewidth Γ as,

$$s = \frac{1}{2}\left(\frac{\Omega^2(r)}{\delta^2 + (\Gamma/2)^2}\right). \tag{1.15}$$

In case of steady state, the Block vector components can be expressed in terms of δ, Ω and s as,

$$\mathcal{U}_{st} = \frac{\delta}{\Omega(r)}\left(\frac{s}{1+s}\right) \tag{1.16a}$$

$$\mathcal{V}_{st} = \frac{\Gamma/2}{\Omega(r)}\left(\frac{s}{1+s}\right) \tag{1.16b}$$

$$\mathcal{W}_{st} = -\frac{1}{1+s} \tag{1.16c}$$

These steady state Bloch vectors will be utilized rigorously in proceeding sections to derive the forces experienced by an atom while interacting with a light beam.

and

$$H_{AR} = -id \sum_{\mu} (\hat{\epsilon}_z.\hat{\epsilon}_\mu)\mathcal{E}_\mu \hat{a}_\mu e^{ik_\mu.r}|e\rangle\langle g| + H.c. \tag{1.9}$$

Here we have denoted the coupling strength (commonly reffered as Rabi frequency) of the transition between the two levels as,

$$\Omega(\mathbf{r}) = -\frac{\hat{\epsilon}_z.\hat{\epsilon}(\mathbf{r})}{\hbar}\mathcal{E}(\mathbf{r}) \tag{1.10}$$

The evolution of the internal degrees of the atoms can be described in terms of the density matrices $\rho = |\psi\rangle\langle\psi|$ as,

$$i\hbar\frac{d\rho}{dt} = [H_{AF}, \rho] = [H_{AL} + H_{AR}, \rho] \tag{1.11}$$

The contribution of the reservoir Hamiltonian H_{AR} leads to the coupling of the atoms to continuum modes which results in the spontaneous emission processes involved in the atomic system. Considering these dissipation effects phenomenologically with a decay constant $\Gamma = (1/4\pi\epsilon_0)\left(4\omega_0^3 d^2/3\hbar c^3\right)$, time evolution of density matrix elements can be written as,

$$\dot{\rho}_{ee} = -\Gamma\rho_{ee} - \frac{i\Omega(r)}{2}\left(e^{-i\phi(r)}\hat{\rho}_{ge} - c.c.\right) \tag{1.12a}$$

$$\dot{\rho}_{gg} = \Gamma\rho_{ee} + \frac{i\Omega(r)}{2}\left(e^{-i\phi(r)}\hat{\rho}_{ge} - c.c.\right) \tag{1.12b}$$

$$\dot{\rho}_{eg} = -(i\omega_0 + \Gamma/2)\rho_{eg} + \frac{i\Omega(r)}{2}e^{-i\phi(r)}e^{-i\omega t}(\rho_{ee} - \rho_{gg}) \tag{1.12c}$$

where $\rho_{gg} = \langle g|\rho|g\rangle$, $\rho_{ee} = \langle e|\rho|e\rangle$ and $\rho_{eg} = \langle e|\rho|g\rangle$ along with $\rho_{eg} = \rho^*_{ge}$.

After transforming the above equations to a frame co-rotating with the laser frequency (*i.e.* transforming the variable $\rho_{eg} \rightarrow \tilde{\rho}_{eg}e^{i\omega t}$) and defining the Bloch vector components

radiation mode μ as,

$$H_F = \sum_{\mu} \hbar\omega_\mu \hat{a}_\mu^\dagger \hat{a}_\mu \tag{1.4}$$

where ω_μ is the frequency of a particular mode μ. In terms of these radiation modes, the electric field of the applied electromagnetic radiation can be described as,

$$\hat{E}(\mathbf{r}) = i \sum_{\mu} \epsilon_\mu \mathcal{E}_\mu \hat{a}_\mu e^{i\mathbf{k}_\mu \cdot \mathbf{r}} + H.c. \tag{1.5}$$

where $\mathbf{k}_\mu$ is the wave vector of mode μ and the electric field per photon is,

$$\mathcal{E}_\mu = \sqrt{\frac{\hbar\omega_\mu}{2\epsilon_0 L^3}}. \tag{1.6}$$

with L^3 being the quantization volume and ϵ_0 is the permittivity of free space.

In case of radiation field of Lasers which operate in a photon abundance condition, a classical treatment of the electromagnetic field becomes sufficient and the electric field expression of Eq. (1.5) can be rewritten in this approximation as,

$$E_L(\mathbf{r}, t) = \hat{\epsilon}(\mathbf{r})\mathcal{E}(\mathbf{r}) \cos(\omega t + \phi(r)), \tag{1.7}$$

where $\hat{\epsilon}$ determines the polarization direction of the field with $\mathcal{E}(\mathbf{r})$, ω and ϕ being amplitude, frequency and initial phase of the light field.

The rest of the modes which are not included in the Laser radiation (in general called 'reservoir' modes) should be treated quantum mechanically as the photon abundance condition becomes void for these modes. Hence, the interaction of the atoms with the field modes can be decomposed into interaction with Laser modes (denoted as H_{AL}) and reservoir modes (denoted as H_{AR}). The expressions of these Hamiltonians under the rotating wave approximation (RWA) can be written as,

$$H_{AL} = \frac{\hbar\Omega(\mathbf{r})}{2} \left(e^{-i\phi(\mathbf{r})} e^{-i\omega t} |e\rangle\langle g| + H.c. \right), \tag{1.8}$$

magnetic fields have reached to such an advanced stage that it has started a new area of fundamental research named atom-optics. Several new applications have emerged of which to name a few, include precise determination of time and inertial sensors to detect gyration and rotation.

1.1 Fundamentals of atom light interaction

In order to obtain an insight into the effect of atom-light interaction on the internal and external dynamics of interacting atoms, the time evolution of the constituent Hamiltonians require to be investigated [3]. A monochromatic electromagnetic radiation interacting with a two level atom (consisting a ground state $|g\rangle$ and excited state $|e\rangle$) can be described by the interaction Hamiltonian H_{AF},

$$H_{AF} = -\mathbf{d}.\hat{\mathbf{E}}(\mathbf{r}, t). \tag{1.1}$$

The atomic dipole moment is $\mathbf{d}$ and $\hat{\mathbf{E}}(\mathbf{r}, t)$ represents the electric field of the laser radiation. The complete Hamiltonian can be written as,

$$H = H_A + H_F + H_{AF}. \tag{1.2}$$

with H_A and H_F being the Hamiltonian containing contributions for an atom and field respectively. In terms of the external (*i.e.* momentum $\mathbf{p}$) and the internal degrees of freedom (*i.e.* spin), the atomic Hamiltonian takes the form,

$$H_A = \frac{\mathbf{p}^2}{2m} + \hbar\omega_0|e\rangle\langle e|. \tag{1.3}$$

The field Hamiltonian can be written in terms of the annihilation and creation operator $\hat{a}_\mu$ and $\hat{a}_\mu^\dagger$ respectively obeying the commutator relation $[\hat{a}_\mu, \hat{a}_\nu^\dagger] = \delta_{\mu\nu}$ for any individual

Chapter 1

An introduction to laser cooling

In this thesis, radio frequency dressed state potentials to trap cold neutral atoms in various geometries have been studied. The use of single and multi-frequency rf-fields in presence of a static quadrupole magnetic trap have been considered both theoretically and experimentally to demonstrate the novel atom trapping potentials. In the proceeding chapters a detail description of all the theoretical models developed and used along with the detail description of the experimental apparatus and results are provided. The aim of this chapter is to provide some familiarity with the light atom interaction and generation of cold atoms using laser cooling and other techniques.

The interaction of light with atoms has an extensive history. From the beginning of spectroscopy, it was established that the internal degrees of freedom of atoms can be probed and modified by the use of light beams of specific wavelength and intensity. It was not before last part of the nineteenth century when the effect of atom-light interaction was first time observed to alter the trajectories of the atoms. With the advent of lasers, the subject of atomic spectroscopy grew over multiple directions. In 1970 Ashkin [1] first demonstrated the manipulation of mechanical momentum of atoms using lasers. Subsequently, several works demonstrated the cooling of atoms in a gas by using lasers [2]. Nowadays, the field of generations and manipulations of cold atoms using lasers and other electro-

2.3 Conclusion

In this chapter, we have discussed the general theoretical approach to calculate the rf-dressed potentials for atoms arising due to a static magnetic field of quadrupole trap and an oscillating rf-field. It has been shown that by changing the polarization and amplitude of the rf-field, a number of specialized trapping geometries can be constructed. The potential applications of these trapping geometries have also been discussed.

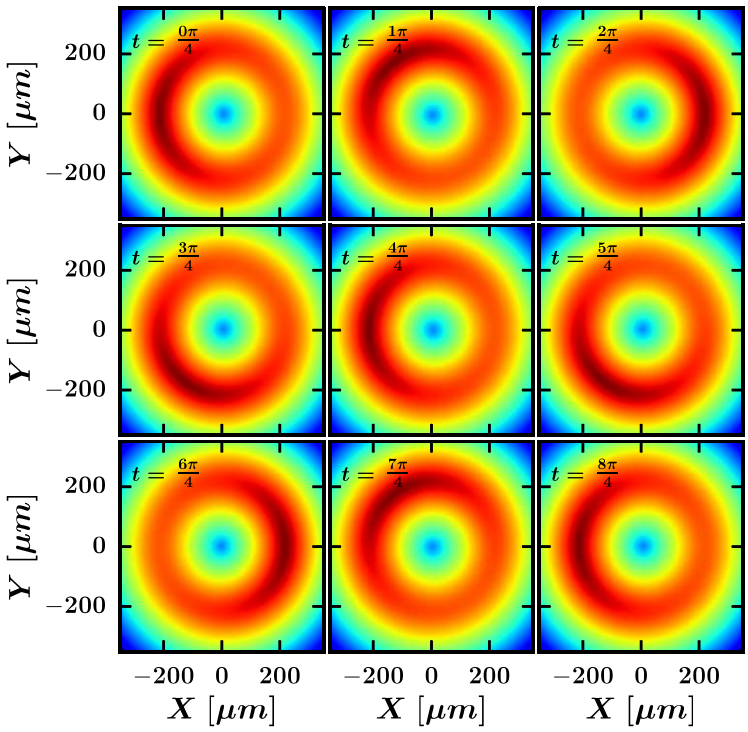

Figure 2.5: Contours of rf-dressed potential of Eq. (2.44) with $B_q = 100\ Gcm^{-1}$, $\omega_0 = 2\pi \times 1.5$ MHz,$B_0^x = B_0^y = 700\ mG$, $B_0^z = 500\ mG$ and $\omega_m = 2\pi \times 1$ Hz for different values of time t.

With the above rf-field, the oscillating potential for ^{87}Rb atoms in the $|F, m_F\rangle$ state takes the form,

$$\epsilon_{osc}(\mathbf{r}) = m_F \hbar \sqrt{\delta_0(\mathbf{r})^2 + |\Omega_{osc}(\mathbf{r})|^2}, \tag{2.44}$$

where

$$|\Omega_{osc}(\mathbf{r})|^2 = \left(\frac{g_F \mu_B}{2\hbar}\right)^2 \left[(B_0^x)^2 \left(\frac{4z^2}{x^2+y^2+4z^2} + \frac{4z}{\sqrt{x^2+y^2+4z^2}} + 1\right) + (B_0^z)^2 \left(\frac{x^2+y^2}{x^2+y^2+4z^2}\right) - \frac{2B^x B^z \left[x\cos(\pi\cos\omega_m t) - y\sin(\pi\cos\omega_m t)\right]}{\sqrt{x^2+y^2+4z^2}} \left(\frac{2z}{\sqrt{x^2+y^2+4z^2}} + 1\right)\right]. \tag{2.45}$$

Plots of the potentials given by Eq. (2.44) with Eq. (2.45) are shown in Fig. 2.5. Here it can be noted that the position of the minimum of the potential evidently moves along the ring's circumference and completes one rotation in the time $T_r = \pi/\omega_m$. After a complete rotation in the time T_r, the sense of rotation gets reversed. Hence, the next rotation is completed in the same time T_r, but the direction of rotation is opposite. This continues, and the sense of the rotation of the potential minimum keeps on changing after a time interval of T_r. Thus, the atom cloud trapped in this potential undergoes an oscillatory motion along the circumference of the ring, with a time period of oscillation of $2T_r$.

The rotating potential described above can be utilized to initiate motion in a Bose Einstein condensate or in a cold atom cloud along a circular path to study super-fluidity, which is otherwise achieved using laser beams of appropriate frequency to transfer momentum from photons to atoms [59, 60, 61]. The use of laser beams to initiate the rotation of a cloud also leads to some heating of the cloud due to the finite scattering rate. A rotating cloud in a ring can serve as a singly-charged vortex state with its vortex core coinciding with the center of the ring. Such singly-charged vortices have also been proposed to serve as qubits in quantum information processing [62, 63].

rotating potential can be described as,

$$\epsilon_{rot}(\mathbf{r}) = m_F \hbar \sqrt{\delta_0(\mathbf{r})^2 + |\Omega_{rot}(\mathbf{r})|^2}, \tag{2.41}$$

where

$$|\Omega_{rot}(\mathbf{r})|^2 = \left(\frac{g_F \mu_B}{2\hbar}\right)^2 \left[(B_0^x)^2 \left(\frac{4z^2}{x^2+y^2+4z^2} + \frac{4z}{\sqrt{x^2+y^2+4z^2}} + 1 \right) + (B_0^z)^2 \left(\frac{x^2+y^2}{x^2+y^2+4z^2} \right) - \frac{2B_0^x B_0^z \left[x\cos(\omega_l t) - y\sin(\omega_l t) \right]}{\sqrt{x^2+y^2+4z^2}} \left(\frac{2z}{\sqrt{x^2+y^2+4z_0^2}} + 1 \right) \right]. \tag{2.42}$$

In Eq. (2.42), the last term in the Rabi frequency expression contains the time dependence, which causes the potential of Eq. (2.41) to be time dependent so that the position of the potential minimum changes with time. The contours in Fig. 2.4 show that the position of the minimum of the potential $\epsilon_{rot}(\mathbf{r})$ moves along a circular path on the ring with time. Thus, the linear phase modulation discussed above converts the ring potential into a rotating well potential. The rate of rotation is governed by the modulation parameter ω_l. As the rotation takes place, experimentally, the temperature of the cloud will likely increase due to the non-adiabatic following of the potential by the atoms in the cloud. This may lower the lifetime of the atoms in the trap. However, this rotation provides excellent opportunities for studying motion-dependent physics phenomenon like super-fluidity in the condensate cloud.

Next, we consider the periodic phase modulation in which the phase of the z-component of the rf-field is considered to vary periodically. Taking the modulation frequency ω_m, we can express the rf-field with phase modulation in z-component as,

$$\mathbf{B}_0(t) = \begin{pmatrix} B_0^x \cos\omega_0 t \\ B_0^y \cos(\omega_0 t + \frac{\pi}{2}) \\ B_0^z \cos(\omega_0 t - \pi\cos(\omega_m t)) \end{pmatrix} \tag{2.43}$$

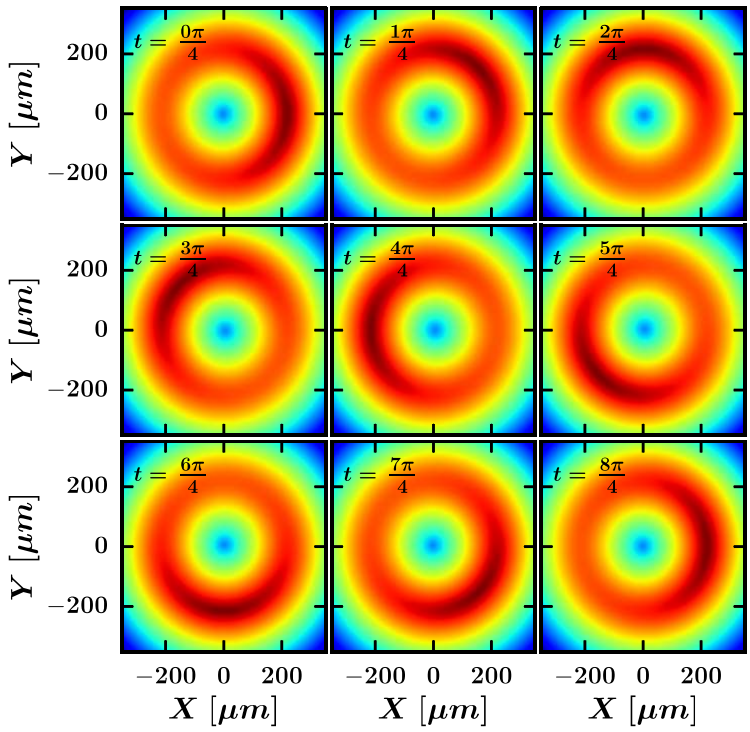

Figure 2.4: Contours of rf-dressed potential of Eq. (2.41) with $B_q = 100\ Gcm^{-1}$, $\omega_0 = 2\pi \times 1.5$ MHz,$B_0^x = B_0^y = 700\ mG$, $B_0^z = 500\ mG$ and $\omega_l = 2\pi \times 1$ Hz for different values of time t.

the applications such as atom-interferometry for rotation sensing [33].

2.2.3 Rotating traps

As we discussed in the previous subsection, the inclusion of the z-component of the rf-field in the generation of the ring trap results in a potential well on the ring. The atoms from the whole ring can be accumulated in this well. Because the position of this potential well on the ring depends on the phase angle ϕ_z, by varying the value of ϕ_z with time, we can move the position of the well (and atom cloud trapped in it) along the circumference of the ring. This rotational motion of the atom cloud seems controllable by controlling the phase modulation in the z-component of the rf-field. In the following, we consider two types of phase modulations in the z-component of the rf-field. One is a linear phase modulation, and the other is a periodic phase modulation. These phase modulations can result in two different types of rotational motions of the potential well and the atom cloud trapped in it and will be discussed in the following.

The linear phase modulation in the z-component of the rf-field results in a rotation of the potential well on the ring's circumference at a rate that is determined by the modulation frequency. For ^{87}Rb atoms in the $|F, m_F\rangle$ state, first, we consider here a linear phase-modulated rf-field of the form,

$$\mathbf{B}_0(t) = \begin{pmatrix} B_0^x \cos\omega_0 t \\ B_0^y \cos(\omega_0 t + \pi/2) \\ B_0^z \cos(\omega_0 t - \omega_l t) \end{pmatrix}, \tag{2.40}$$

where the value of the modulation frequency ω_l is very small compared to ω_0, so that the modified potential due to the phase-modulation can be adiabatically followed by the atoms. Using the rf-field in Eq. (2.40) with $B_0^x = B_0^y$ and the static field in Eq. (2.4), the

$B_0^x = B_0^y$ and the phase difference between these components being $\pi/2$. The incorporation of a z-component in the rf-field results in an anisotropy in the isotropic ring potential. For the case with $B_0^x = B_0^y$ in Eq. (2.35) and static quadrupole trap field, the dressed-state potential for an atom (*e.g.*, ^{87}Rb) in the state $|F, m_F\rangle$ can be calculated to be,

$$\epsilon_{ar}(\mathbf{r}) = m_F \hbar \sqrt{\delta_0(\mathbf{r})^2 + |\Omega_{ar}(\mathbf{r})|^2}, \tag{2.38}$$

where

$$\begin{aligned}|\Omega_{ar}(\mathbf{r})|^2 = \left(\frac{g_F \mu_B}{2\hbar}\right)^2 \Bigg[& \frac{4z^2}{x^2+y^2+4z^2}\left(\frac{(B_0^x)^2 x^2 + (B_0^y)^2 y^2}{x^2+y^2}\right) + \left(\frac{(B_0^x)^2 y^2 + (B_0^y)^2 x^2}{x^2+y^2}\right) \\ & - \frac{4B_0^x B_0^y z}{\sqrt{x^2+y^2+4z^2}} + (B_0^z)^2\left(\frac{x^2+y^2}{x^2+y^2+4z^2}\right) + \frac{2B_0^z x\cos\phi_z}{\sqrt{x^2+y^2+4z^2}}\left(\frac{2B_0^x z}{\sqrt{x^2+y^2+4z^2}} - B_0^y\right) \\ & + \frac{2B_0^z y \sin\phi_z}{\sqrt{x^2+y^2+4z^2}}\left(B_0^x - \frac{2B_0^y z}{\sqrt{x^2+y^2+4z^2}}\right)\Bigg]. \end{aligned} \tag{2.39}$$

Plots of the potentials given by Eqs. (2.38) and (2.39) are shown in Fig. 2.3 for different values of the rf-field amplitude B_0^z at a given value of ϕ_z. Due to the presence of the z-component in the rf-field, a potential well is formed at a particular position on the ring. In an earlier work [53], the asymmetric ring potential due to presence of this z-component in rf-field was experimentally observed in an rf-dressed quadrupole trap.

Here we note that, the depth of the potential well on the ring depends on the value of B_0^z whereas the position of the well (*i.e.*, the potential minimum) on the ring depends on the phase angle ϕ_z. Figure 2.3 shows that, as B_0^z is increased, the ring-shaped potential becomes more asymmetric (*i.e.*, tilted) with increasing well depth. The atoms from the whole ring can be forced to drain to this well position by suitably adjusting the value of B_0^z. This allows the transfer of cold atoms to a particular site on the ring just by adjusting the rf-field z-component. By changing the value of ϕ_z, the position of this potential minimum (*i.e.*, the well) can be changed to our choice, which can be made to act as a 'conveyor belt' for the cold atom cloud. The transport of the atoms along the ring may also be useful in

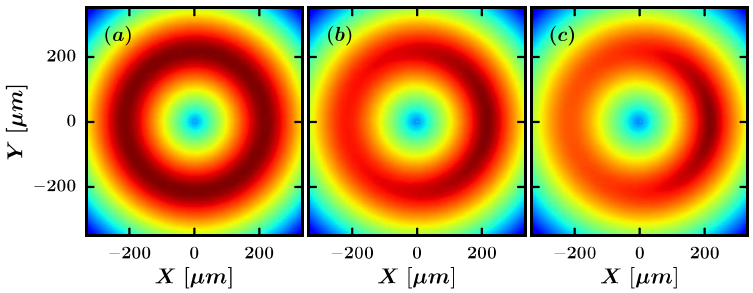

Figure 2.3: Contours of rf-dressed potential of Eq. (2.38) with $B_q = 100\ Gcm^{-1}$, $\omega_0 = 2\pi \times 1.5$ MHz,$B_0^x = B_0^y = 700\ mG$ for: (a) $B_0^z = 0\ mG$, (b) $B_0^z = 300\ mG$ (c) $B_0^z = 500\ mG$.

$$|\Omega_{aa}(\mathbf{r})|^2 = \left(\frac{g_F\mu_B}{2\hbar}\right)^2 \left[\frac{4z^2}{x^2+y^2+4z^2}\left(\frac{(B_0^x)^2x^2+(B_0^y)^2y^2}{x^2+y^2}\right)+\left(\frac{(B_0^x)^2y^2+(B_0^y)^2x^2}{x^2+y^2}\right)\right.$$
$$-\frac{4B_0^xB_0^yz}{\sqrt{x^2+y^2+4z^2}}+(B_0^z)^2\left(\frac{x^2+y^2}{x^2+y^2+4z^2}\right)+\frac{2B_0^zx\cos\phi_z}{\sqrt{x^2+y^2+4z^2}}\left(\frac{2B_0^xz}{\sqrt{x^2+y^2+4z^2}}-B_0^y\right)$$
$$\left.+\frac{2B_0^zy\sin\phi_z}{\sqrt{x^2+y^2+4z^2}}\left(B_0^x-\frac{2B_0^yz}{\sqrt{x^2+y^2+4z^2}}\right)\right]. \quad (2.37)$$

The contours of the rf-dressed potentials given by Eq. (2.36) with Eq. (2.37) for different values of B_0^z are shown in Fig. 2.2. These graphs clearly reveal that the split-arcs become asymmetric by the inclusion of a z-component in the rf-field. The ultracold atoms trapped in these asymmetric split-arcs may be useful for studying tunnelling and Josephson oscillations [57, 58, 22], with tunnelling along a circular path. As described in Ref. [22], the asymmetry of the two trapping potentials can be used to control the Josephson oscillations of the population between trapping potentials. If the asymmetry is increased, the Josephson oscillations can be suppressed, and self trapping can be reached. In our proposed asymmetric split-arc potential, the asymmetry can be controlled by adjusting the amplitude and the phase of third component of the field. The separation between the minima of arcs depends upon the arc length, which can be controlled by controlling the radius of the ring as well as the phase angle ϕ_z.

We know that an isotropic ring potential can be generated by the use of the rf-field with

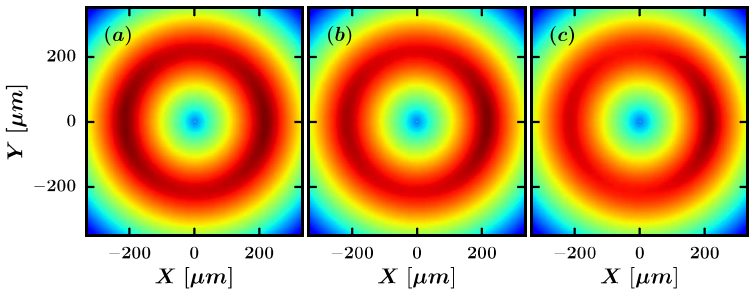

Figure 2.2: Contours of rf-dressed potential of Eq. (2.36) with $B_q = 100\ Gcm^{-1}$, $\omega_0 = 2\pi \times 1.5$ MHz, $B_0^x = 700\ mG$, $B_0^y = 350\ mG$ and for: (a) $B_0^z = 0\ mG$, (b) $B_0^z = 100\ mG$ (c) $B_0^z = 200\ mG$.

2.2.2 Asymmetric ring traps

Split-arcs with unequal depths of the trapping potential are expected to be useful for studying quantum-mechanical tunneling with cold atoms trapped in the arcs. We note that such arcs with unequal potential depths can be created by incorporating a z-component in the rf-field. Thus, if the rf-field is taken as

$$\mathbf{B}_0(t) = \begin{pmatrix} B_0^x \cos\omega_0 t \\ B_0^y \cos(\omega_0 t + \pi/2) \\ B_0^z \cos(\omega_0 t - \phi_z) \end{pmatrix} \tag{2.35}$$

with $B_0^x \neq B_0^y$, then the corresponding rf-dressed potential can be written as

$$\epsilon_{aa}(\mathbf{r}) = m_F \hbar \sqrt{\delta_0(\mathbf{r})^2 + |\Omega_{aa}(\mathbf{r})|^2}, \tag{2.36}$$

with

The expression for this split-arc trapping geometry is given as,

$$\epsilon_{sa}(\mathbf{r}) = m_F\hbar\sqrt{\delta_0(\mathbf{r})^2 + |\Omega_{sa}(\mathbf{r})|^2}, \tag{2.32}$$

where

$$|\Omega_{sa}(\mathbf{r})|^2 = \left(\frac{g_F\mu_B}{2\hbar}\right)^2\left[\frac{4z^2}{x^2+y^2+4z^2}\left(\frac{(B_0^x)^2x^2}{x^2+y^2}\right) + \left(\frac{(B_0^x)^2y^2 + (B_0^y)^2x^2}{x^2+y^2}\right) - \frac{4B_0^xB_0^yz}{\sqrt{x^2+y^2+4z^2}}\right]. \tag{2.33}$$

A plot of Eq. (2.32) is shown in Fig. 2.1 (b) for unequal values of B_x and B_y. We should point out that the orientation of the arcs depend on the values of B_x, B_y, and the phase (ϕ_y). Heathcote *et al.* [52] have experimentally demonstrated the variation in the orientation of the split-arcs by varying the relative phase between the two perpendicular components of the rf-field.

Similarly, a well-known trapping geometry with rf-dressed potentials is a ring-shaped trapping potential [56, 52, 53]. The ring-shaped trapping potential can be generated by using a circularly-polarized rf-field of the form $\mathbf{B}_0(t) = (B_0^x\cos\omega_0 t, B_0^y\cos(\omega_0 t + \frac{\pi}{2}), 0)$, with $B_0^x = B_0^y$ and the static magnetic field. For these fields, Eqs. (2.22) and (2.30) evidently result in an rf-dressed potential (for an atom in the state $|F, m_F\rangle$) with a spatial variation:

$$\epsilon_r = m_F\hbar\sqrt{\delta_0^2 + (B_0^x)^2\left(\frac{g_F\mu_B}{2\hbar}\right)^2\left[\frac{4z^2}{x^2+y^2+4z^2} + \frac{4z}{\sqrt{x^2+y^2+4z^2}} + 1\right]}. \tag{2.34}$$

The potential given by Eq. (2.34) is independent of the polar angle ϕ, and its plot in the xy-plane is shown in Fig. 2.1 (c). From the graph, the minimum of the potential evidently lies on a circular ring in the xy-plane. Therefore, this potential is useful to trap an atom cloud in a ring or toroidal shape.

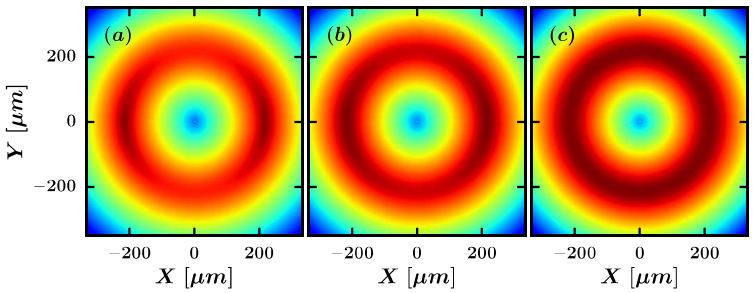

Figure 2.1: Contours of rf-dressed potential with $B_q = 100\ Gcm^{-1}$, $\omega_0 = 2\pi \times 1.5$ MHz for: (a) double well potential of Eq. (2.31) with $B_0^x = 700\ mG$ and $B_0^y = 0$, (b) split arc potential of Eq. (2.32) with $B_0^x = 700\ mG$ and $B_0^y = 350\ mG$ and (c) ring potential of Eq. (2.34) with $B_0^x = B_0^y = 700\ mG$.

2.2.1 Symmetric traps

A number of 2D symmetric trapping geometries can be realized by considering various forms of the rf-field. For example, a double-well potential can be generated by taking a linearly polarized rf-field along the x-axis, *i.e.*, $\mathbf{B}_0(t) = (B_0^x \cos\omega_0 t, 0, 0)$, in the presence of the static field of quadrupole magnetic trap. The double-well-type rf-dressed potential for an atom in the state $|F, m_F\rangle$ can be evaluated from Eqs. (2.22) and (2.30) as

$$\epsilon_{dw} = m_F \hbar \sqrt{\delta_0^2 + \left(\frac{g_F \mu_B}{2\hbar}\right)^2 \left[\frac{(B_0^x)^2}{x^2+y^2}\left(\frac{4x^2z^2}{x^2+y^2+4z^2} + y^2\right)\right]}, \tag{2.31}$$

where δ_0 is the detuning given by Eq. 2.20. Fig. 2.1 (a) shows the double-well potential landscape of the rf-dressed potential given by Eq. 2.31. Here colors from blue to red show potential energy in decreasing order with dark red being the minimum of the potential.

Further, instead of a linearly-polarized rf-field, if an elliptically-polarized rf-field is chosen, the generated potential will be of arc shaped. With an rf-field of the form $\mathbf{B}_0(t) = (B_0^x \cos\omega_0 t, B_0^y \cos(\omega_0 t + \frac{\pi}{2}), 0)$, with $B_0^x \neq B_0^y$, and with a static field as given by Eq. (2.4), the rf-dressed potential for the atoms looks like the split-arcs as shown in Fig. 2.1 (b).

the vector $\hat{e_3}$. Hence, using Eq. (2.21) and Eq. (2.29), one gets the expression for the Rabi frequency as

$$|\Omega_0(\mathbf{r})|^2 = \left(\frac{g_F\mu_B}{2\hbar}\right)^2 \Bigg[\frac{4z^2}{x^2+y^2+4z^2}\left(\frac{(B_0^x)^2x^2+(B_0^y)^2y^2}{x^2+y^2}\right)+\left(\frac{(B_0^x)^2y^2+(B_0^y)^2x^2}{x^2+y^2}\right)$$
$$+(B_0^z)^2\left(\frac{x^2+y^2}{x^2+y^2+4z^2}\right)-\frac{2B_0^xB_0^yxy\cos\phi_y}{x^2+y^2+4z^2}+\frac{4B_0^xB_0^yz\sin\phi_y}{\sqrt{x^2+y^2+4z^2}}+\frac{4B_0^yB_0^zyz\cos(\phi_y-\phi_z)}{x^2+y^2+4z^2}$$
$$+\frac{2B_0^yB_0^zx\sin(\phi_y-\phi_z)}{\sqrt{x^2+y^2+4z^2}}+\frac{4B_0^zB_0^xzx\cos\phi_z}{x^2+y^2+4z^2}+\frac{2B_0^zB_0^xy\sin\phi_z}{\sqrt{x^2+y^2+4z^2}}\Bigg]. \quad (2.30)$$

With this expression for Rabi frequency $|\Omega_0(\mathbf{r})|$ (*i.e.*, Eq. (2.30)), the dressed-state potential (Eq. (2.22)) for an atom interacting with an rf-field and a static quadrupole trap field can be obtained.

2.2 Trapping geometries

Equations (2.22) and (2.30) provide a general expression for the rf-dressed potential ($\epsilon(\mathbf{r})$) for an atom in a Zeeman hyperfine sub-level $|F, m_F\rangle$ interacting with a static magnetic field $\mathbf{B}_s(\mathbf{r})$ and an rf-field $\mathbf{B}_0(t)$ given by Eq. (2.4) and Eq. (2.6) respectively. In this section, the formalism developed in the previous section has been utilized to obtain the rf-dressed potentials for selected configurations of the rf-field and the static magnetic field of a quadrupole trap. Based on this, we discuss different geometries for trapping and manipulating cold atoms, with a particular example of the ^{87}Rb atom in $|F=2, m_F=2\rangle$ state.

and

$$\mathfrak{R}^{-1}(\theta,\phi) = \begin{pmatrix} \cos\theta\cos\phi & \cos\theta\sin\phi & \sin\theta \\ sin\phi & -cos\phi & 0 \\ \sin\theta\cos\phi & \sin\theta\sin\phi & -\cos\theta \end{pmatrix} \tag{2.26}$$

can be used to relate the basis vectors $\hat{e}_1$, $\hat{e}_2$ and $\hat{e}_3$ to the basis vectors $\hat{e}_x$, $\hat{e}_y$ and $\hat{e}_z$ using the relations,

$$\mathfrak{R}(\theta,\phi)\hat{e}_x = \hat{e}_1;\ \mathfrak{R}(\theta,\phi)\hat{e}_y = \hat{e}_2;\ \mathfrak{R}(\theta,\phi)\hat{e}_z = \hat{e}_3, \tag{2.27}$$

$$\mathfrak{R}^{-1}(\theta,\phi)\hat{e}_1 = \hat{e}_x;\ \mathfrak{R}^{-1}(\theta,\phi)\hat{e}_2 = \hat{e}_y;\ \mathfrak{R}^{-1}(\theta,\phi)\hat{e}_3 = \hat{e}_z. \tag{2.28}$$

With the above transformation matrices, $\mathfrak{R}(\theta,\phi)$ and $\mathfrak{R}^{-1}(\theta,\phi)$, any arbitrary vector (e. g. an applied rf-field) can also be transformed from one coordinate system ($(\hat{e}_x,\hat{e}_y,\hat{e}_z)$ to another $(\hat{e}_1,\hat{e}_2,\hat{e}_3)$). Thus, the expression of the rf-field vector, which is given in the laboratory coordinate system by Eq. (2.6), can be transformed to the expression in the local coordinate system as a vector $\mathfrak{R}^{-1}(\theta,\phi)\mathbf{B}_0(t)$. This is given as,

$$\begin{aligned} \mathfrak{R}^{-1}(\theta,\phi)\mathbf{B}_0(t) &= \begin{pmatrix} B_0^{\perp 1}(t) \\ B_0^{\perp 2}(t) \\ B_0^{\parallel}(t) \end{pmatrix} \\ &= \begin{pmatrix} B_0^x\cos\theta\cos\phi\cos\omega_0 t + B_0^y\cos\theta\sin\phi\cos(\omega_0 t-\phi_y) + B_z\sin\theta\cos(\omega_0 t-\phi_z) \\ B_0^x\sin\phi\cos\omega_0 t - B_0^y\cos\phi\cos(\omega_0 t-\phi_y) \\ B_0^x\sin\theta\cos\phi\cos\omega_0 t + B_0^y\sin\theta\sin\phi\cos(\omega_0 t-\phi_y) - B_0^z\cos\theta\cos(\omega_0 t-\phi_z) \end{pmatrix}. \end{aligned} \tag{2.29}$$

Evidently, the first and the second elements of the column vector in Eq. (2.29) give $B_0^{\perp 1}(t)$ and $B_0^{\perp 2}(t)$, which are required to evaluate the Rabi frequency by using Eq. (2.21). The third element of the column vector $\mathfrak{R}^{-1}(\theta,\phi)\mathbf{B}_0(t)$ in Eq. 2.29 represents the rf-field along

It is important to note that the Rabi frequency given by Eq. (2.21) does not have a contribution from the parallel component of the rf-field $B_0^{\parallel}(t)$. Thus, only the components of the rf-field perpendicular to the local static field (*i.e.*, $B_0^{\perp 1}(t)$ and $B_0^{\perp 2}(t)$) are important for the evaluation of the Rabi frequency. For a time-varying rf-field of form given in Eq. 2.6, the calculation of the Rabi frequency involves the calculation of $B_0^{\perp 1}(t)$ and $B_0^{\perp 2}(t)$. This is briefly discussed as follows.

In the laboratory coordinate system, the unit vectors along the x-, y-, and z-axes (*i.e.*, $\hat{e}_x$, $\hat{e}_y$, and $\hat{e}_z$) can be expressed in the column vector form as,

$$\hat{e}_x = \begin{pmatrix} 1 \\ 0 \\ 0 \end{pmatrix}, \ \hat{e}_y = \begin{pmatrix} 0 \\ 1 \\ 0 \end{pmatrix}, \ \hat{e}_z = \begin{pmatrix} 0 \\ 0 \\ 1 \end{pmatrix}. \tag{2.23}$$

For a quadrupole magnetic trap with its static magnetic field given by Eq. (2.4), the basis vectors ($\hat{e}_1$, $\hat{e}_2$ and $\hat{e}_3$) of the local coordinate system can be expressed in the laboratory coordinate system as [55],

$$\hat{e}_1 = \begin{pmatrix} cos\theta\, cos\phi \\ cos\theta\, sin\phi \\ sin\theta \end{pmatrix}, \ \hat{e}_2 = \begin{pmatrix} sin\phi \\ -cos\phi \\ 0 \end{pmatrix}, \ \hat{e}_3 = \begin{pmatrix} sin\theta\, cos\phi \\ sin\theta\, sin\phi \\ -cos\theta \end{pmatrix}, \tag{2.24}$$

where $\cos\phi = \frac{x}{\sqrt{x^2+y^2}}$, $\sin\phi = \frac{y}{\sqrt{x^2+y^2}}$, $\cos\theta = \frac{2z}{\sqrt{x^2+y^2+4z^2}}$, and $\sin\theta = \frac{\sqrt{x^2+y^2}}{\sqrt{x^2+y^2+4z^2}}$.

The rotation matrices $\mathfrak{R}(\theta,\phi)$ and $\mathfrak{R}^{-1}(\theta,\phi)$ defined by

$$\mathfrak{R}(\theta,\phi) = \begin{pmatrix} \cos\theta\cos\phi & \sin\phi & \sin\theta\cos\phi \\ \cos\theta\sin\phi & -\cos\phi & \sin\theta\sin\phi \\ \sin\theta & 0 & -\cos\theta \end{pmatrix} \tag{2.25}$$

be written in the matrix form as,

$$\frac{H_R}{g_F\mu_B} = \begin{bmatrix} 2(|B^S| - \frac{\hbar\omega_0}{g_F\mu_B}) & \frac{1}{2}(B^{RF}_{\perp 1} - iB^{RF}_{\perp 2}e^{i\gamma}) & 0 & 0 & 0 \\ \frac{1}{2}(B^{RF}_{\perp 1} + iB^{RF}_{\perp 2}e^{-i\gamma}) & (|B^S| - \frac{\hbar\omega_0}{g_F\mu_B}) & \frac{\sqrt{6}}{4}(B^{RF}_{\perp 1} - iB^{RF}_{\perp 2}e^{i\gamma}) & 0 & 0 \\ 0 & \frac{\sqrt{6}}{4}(B^{RF}_{\perp 1} + iB^{RF}_{\perp 2}e^{-i\gamma}) & 0 & \frac{\sqrt{6}}{4}(B^{RF}_{\perp 1} - iB^{RF}_{\perp 2}e^{i\gamma}) & 0 \\ 0 & 0 & \frac{\sqrt{6}}{4}(B^{RF}_{\perp 1} + iB^{RF}_{\perp 2}e^{-i\gamma}) & -(|B^S| - \frac{\hbar\omega_0}{g_F\mu_B}) & \frac{1}{2}(B^{RF}_{\perp 1} - iB^{RF}_{\perp 2}e^{i\gamma}) \\ 0 & 0 & 0 & \frac{1}{2}(B^{RF}_{\perp 1} + iB^{RF}_{\perp 2}e^{-i\gamma}) & -2(|B^S| - \frac{\hbar\omega_0}{g_F\mu_B}) \end{bmatrix}. \quad (2.18)$$

The diagonalization of the matrix in Eq. (2.18) gives the energy eigenvalues of the Hamiltonian H_R in Eq. (2.17). These eigenvalues give the adiabatic dressed-state potentials ϵ for the atom-radiation system. After the matrix in Eq. (2.18) is diagonalised, the dressed-state potentials (*i.e.* eigen-energy values of matrix in Eq. (2.18)) for the Zeeman sub-levels $|F, m_F\rangle$ can be written as,

$$\epsilon(\mathbf{r}) = m_F g_F \mu_B \sqrt{\left(|\mathbf{B}_s(\mathbf{r})| - \frac{\hbar\omega_0}{g_F\mu_B}\right)^2 + \frac{1}{4}\left[(B_0^{\perp 1})^2 + (B_0^{\perp 2})^2 + 2B_0^{\perp 1}B_0^{\perp 2}\sin\gamma\right]}. \quad (2.19)$$

Now identifying the detuning (δ_0) and Rabi frequency (Ω_0) of the rf-field as

$$\delta_0 = \omega_0 - \frac{g_F\mu_B}{\hbar}|\mathbf{B}_s| \quad (2.20)$$

and

$$|\Omega_0|^2 = \left(\frac{g_F\mu_B}{2\hbar}\right)^2\left[(B_0^{\perp 1})^2 + (B_0^{\perp 2})^2 + 2B_0^{\perp 1}B_0^{\perp 2}\sin\gamma\right]. \quad (2.21)$$

With the definition of the coupling strength (i.e. Rabi frequency) in Eq. (2.21) and detuning in Eq. (2.20), we can rewrite the dressed state potential as,

$$\epsilon(\mathbf{r}) = m_F\hbar\sqrt{\delta_0^2 + |\Omega_0|^2}. \quad (2.22)$$

and the Schrödinger equation as,

$$i\hbar\frac{\partial|\psi\rangle_R}{\partial t} = H_R|\psi\rangle_R, \tag{2.12}$$

where

$$H_R(t) = UHU^\dagger + i\hbar\frac{\partial U}{\partial t}U^\dagger. \tag{2.13}$$

We can write the time dependent components of the rf-field in the local coordinate system $(\hat{e}_1, \hat{e}_2, \hat{e}_3)$ as,

$$B_0^{\perp 1}(t) = B_0^{\perp 1}\cos(\omega_0 t) \tag{2.14}$$

$$B_0^{\perp 2}(t) = B_0^{\perp 2}\cos(\omega_0 t + \gamma_1) \tag{2.15}$$

$$B_0^{\parallel}(t) = B_0^{\parallel}\cos(\omega_0 t + \gamma_2) \tag{2.16}$$

where γ_1 and γ_2 are the phase difference of the components along the $\hat{e}_2$ and the $\hat{e}_3$ with respect to $\hat{e}_1$ direction respectively. After applying the rotating-wave approximation and using Eq. (2.13), we can convert the time dependent Hamiltonian of Eq. (2.13) into a time independent Hamiltonian as,

$$\begin{aligned} H_R(t) &= H_R \\ &= \frac{g_F\mu_B}{\hbar}\left[F_3\left(|\mathbf{B}_s| - \frac{\hbar\omega_0}{g_F\mu_B}\right) + \left\{\frac{F_+}{4}(B_0^{\perp 1} - iB_0^{\perp 2}e^{i\gamma}) + \frac{F_-}{4}(B_0^{\perp 1} + iB_0^{\perp 2}e^{-i\gamma})\right\}\right]. \end{aligned} \tag{2.17}$$

Here, $F_+ = F_1 + iF_2$ and $F_- = F_1 - iF_2$ are the raising and the lowering operators for the hyperfine angular momentum, respectively. $\gamma = \gamma_2 - \gamma_1$ is the relative phase separation between the two perpendicular components of the rf-field. For an atom in the $|F, m_F\rangle$ manifold, e.g. ^{87}Rb in $F = 2$ and $m_F = \{2, 1, 0, -1, -2\}$, the interaction Hamiltonian can

At any spatial point $\mathbf{r} \equiv (x, y, z)$, the staic field direction can be denoted by the unit vector $\hat{e}_s = \mathbf{B}_s/|\mathbf{B}_s|$. In order to evaluate adiabatic potentials for an atom in the magnetic field given by Eq. (2.8), we follow the theoretical approach described earlier [54]. In this approach, first, the Hamiltonian of Eq. (2.7) is evaluated in a new coordinate system whose one basis vector is parallel to the local magnetic-field's direction (*i.e.* $\hat{e}_s$). In this new local coordinate system, represented by unit basis vectors $(\hat{e}_1, \hat{e}_2, \hat{e}_3)$, the unit vector $\hat{e}_3$ is along the direction of the local static magnetic field $(\hat{e}_s)$, and the other two unit vectors (*i.e.* $\hat{e}_1$ and $\hat{e}_2$) are perpendicular to $\hat{e}_s$, as well as to each other. Due to variation of $\mathbf{B}_s(\mathbf{r})$ in space, these unit vectors $(\hat{e}_1, \hat{e}_2, \hat{e}_3)$ turn out to be position dependent when expressed in the laboratory coordinate system. In the new local coordinate system $(\hat{e}_1, \hat{e}_2, \hat{e}_3)$, the static magnetic field from the quadrupole trap is given by $(0, 0, |\mathbf{B}_s(\mathbf{r})|)^T$ and the applied rf-field by $(B_0^{\perp 1}(t), B_0^{\perp 2}(t), B_0^{\parallel}(t))^T$. The Hamiltonian in Eq. (2.7) in this local coordinate system can be given as,

$$H(t) = \frac{g_F \mu_B}{\hbar}\left[F_3|\mathbf{B}_s| + F_3 B_0^{\parallel}(t) + F_1 B_0^{\perp 1}(t) + F_2 B_0^{\perp 2}(t)\right]. \tag{2.9}$$

Here F_1, F_2 and F_3 are components of $\mathbf{F}$ along $\hat{e}_1, \hat{e}_2$ and $\hat{e}_3$. Because $\hat{e}_3$ is the unit vector along the vector $\hat{e}_s$, it represents the local quantization axis.

In the next step, the Hamiltonian in Eq. (2.9)is transformed to a frame rotating about F_3 by applying an unitary transformation,

$$U = \exp\left[\frac{i}{\hbar}(\omega_0 t F_3)\right], \tag{2.10}$$

which modifies the state $|\psi\rangle$ to $|\psi\rangle^R$ as,

$$|\psi\rangle_R = U|\psi\rangle \tag{2.11}$$

For a quadrupole magnetic trap in which the atoms are considered to be trapped, the form of the $\mathbf{B}_s(\mathbf{r})$ near the trap center can be approximated as,

$$\mathbf{B}_s(\mathbf{r}) = B_q \begin{pmatrix} x \\ y \\ -2z \end{pmatrix}, \tag{2.4}$$

where B_q is the radial field gradient of the quadrupole trap. The resulting Larmor frequency ω_L is then inherently position dependent and can be described as,

$$\omega_L(\mathbf{r}) = \frac{g_F \mu_B}{\hbar} B_q \sqrt{x^2 + y^2 + 4z^2}. \tag{2.5}$$

In the Cartesian coordinate system, the monochromatic rf-field of angular frequency ω_0 interacting with the atoms trapped in the quadrupole trap can be written as,

$$\mathbf{B}_0(t) = \begin{pmatrix} B_0^x cos(\omega_0 t) \\ B_0^y cos(\omega_0 t - \phi_y) \\ B_0^z cos(\omega_0 t - \phi_z) \end{pmatrix}, \tag{2.6}$$

where B_0^x, B_0^y and B_0^z are the rf-field strengths along the Cartesian axes and ϕ_y, ϕ_z are the phase difference of the y and z component respectively with respect to the x-component.

For an ultra cold atomic sample, we can neglect the field free Hamiltonian $\mathcal{H} \approx -\frac{\hbar^2}{2m}\nabla^2$, and obtain the time-dependent Hamiltonian $H(t)$ responsible for the interaction of the atoms with static and rf-fields as,

$$H(t) = -\boldsymbol{\mu} \cdot \mathbf{B}(\mathbf{r}, t) = \frac{g_F \mu_B}{\hbar} \mathbf{F} \cdot \mathbf{B}(\mathbf{r}, t), \tag{2.7}$$

where,

$$\mathbf{B}(\mathbf{r}, t) = \mathbf{B}_s(\mathbf{r}) + \mathbf{B}_0(t). \tag{2.8}$$

tion, frequency and phase. Since the first proposal by Zobay and Garraway [45], atom trapping in these rf-dressed potentials has been studied theoretically, as well as experimentally, by several groups worldwide [47, 48, 42, 49]. Using this approach, atoms have been trapped in different geometries that include double-well [42], quasi-two-dimensional traps [48, 50, 51] and ring traps [52, 53, 54].

In this chapter, we present an appropriate theoretical background to understand the generation of rf-dressed potentials using a static magnetic field of a quadrupole trap and an rf-field with different polarization components and different relative phases. It is found that the trapping geometries can be manipulated by changing the strength of the rf-field components and their relative phases.

2.1 Theory

We consider an arbitrary N-level atomic system in presence of a static magnetic field interacting with a monochromatic rf-field having an arbitrary polarization. The atomic system is treated quantum mechanically and the radiation field is treated classically. The evolution of the atomic system can be determined by knowing the interaction Hamiltonian of the time-dependent schrödinger equation,

$$i\hbar\frac{\partial}{\partial t}|\psi\rangle = H|\psi\rangle. \tag{2.1}$$

where

$$H(t) = H_0 - \boldsymbol{\mu}.\mathbf{B}_0(t) \tag{2.2}$$

with

$$H_0 = \mathcal{H} - \boldsymbol{\mu}.\mathbf{B}_s(\mathbf{r}) \tag{2.3}$$

Here, $\mathcal{H}$ represents the Hamiltonian without any field, $\boldsymbol{\mu}$ represents the magnetic dipole moment of the atoms and $\mathbf{B}_s(\mathbf{r})$ represents the static magnetic field of a quadrupole trap.

Chapter 2

Radio-frequency dressed potentials

It is well known from the basic electrodynamics that an atom with a finite magnetic dipole moment can be trapped in an inhomogeneous static magnetic field at the position of the minimum potential energy [44]. The potential energy of the atom in the magnetic field B in the linear regime is $V = m_F g_F \mu_B B$, where m_F is the Zeeman hyperfine quantum number for the state with hyperfine number F, g_F is the Lande's g factor for the hyperfine state and μ_B is the Bohr magneton [4]. States with $m_F g_F > 0$ are called low-field-seeking states because the atoms will achieve the minimum of the potential at the lowest field strength. The reverse is true for the case with the states having $m_F g_F < 0$, aptly named as high-field-seeking states. Maxwell's equation ($\nabla.B = 0$), together with the Earnshaw's theorem, denies the existence of the maximum of a magnetic field in free space. Hence, trapping with a static magnetic field is possible only for atoms in low-field-seeking states at the minimum of the magnetic field. Therefore, the trapping geometries achievable using a static magnetic field alone remain severely limited. To overcome this limitation, Zobay and Garraway [45, 46] proposed the use of the radio-frequency (rf) field in the presence of the static magnetic field to generate the rf-dressed potentials to trap atoms in potential landscapes difficult to produce by static traps alone. These potentials, offer extensive control over trapping geometries through rf-field parameters such as amplitude, polariza-

experimentally observed. A reasonable agreement between the theoretical predictions in chapter 2 and the experimental observations shown in this chapter is found.

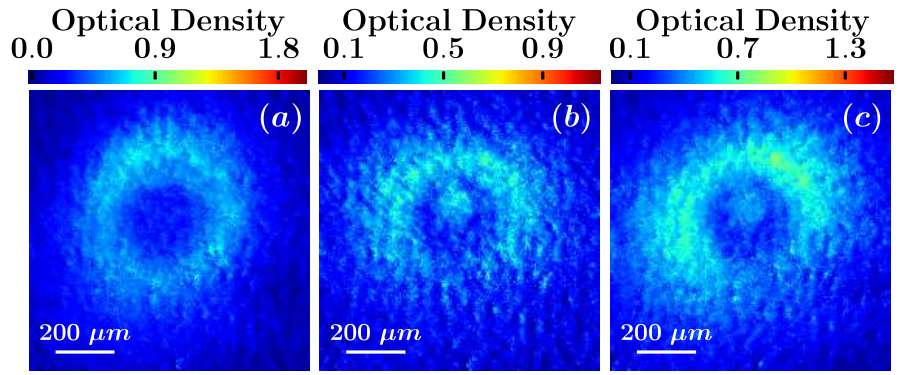

Figure 3.8: (a) Absorption images of the atom cloud in a ring trap formed by a single rf-field of frequency $\omega_0 = 2\pi \times 1.5$ MHz. (b) and (c) shows absorption images while applying a second weak rf-field of frequency $\omega_1 = 2\pi \times 1$ MHz. The central cloud is trapped in the $|F = 2, m_F = -2\rangle_A$ state while the concentric ring cloud is in state $|F = 2, m_F = 2\rangle_A$.

absorption images are shown in Figure. 3.8. The function of this weak rf-field is to change the states of the atom from upper dressed states ($|F = 2, m_F = 2\rangle_A$ and $|F = 2, m_F = 1\rangle_A$, having minimum potential at the ring) to lower dressed states ($|F = 2, m_F = -2\rangle_A$ and $|F = 2, m_F = -1\rangle_A$, having minimum potential at the quadrupole trap center). Figure 3.8 (a) shows the image of the cloud trapped in the ring when only the first rf-field was applied with final frequency as $\omega_0 = 2\pi \times 1.5$ MHz. The resulting cloud image after the rf-field irradiation from the multi-turn coil was a ring as shown in Fig. 3.8 (a). As the rf-field from the second coil was also applied independently, some of the atoms return back to the central region from the ring circumference. This results in concentric trapping of atom cloud. The increase of optical density at the central hollow portion bears the signature of trapping in the adiabatic potential corresponding to different dressed states.

3.4 Conclusion

In this chapter, the experimental results on the formation of the ring shaped trap for cold atoms using rf-dressed potentials have been presented. Various ring traps including symmetric ring traps of variable radius, asymmetric ring and concentric ring traps have been

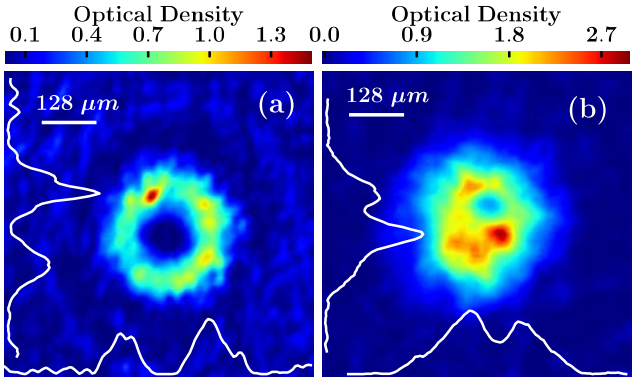

Figure 3.7: (a) The absorption image of the cloud after evaporative cooling and rf-dressing using the multi-turn coil (frequency of the rf-field is ramped down from 15 MHz to 1 MHz). (b) The absorption image of the cloud when both the single and multi turn coils are simultaneously used with frequency of the rf-field ramped down from 15 MHz to 1 MHz. The image shows the formation of asymmetric ring traps with two rf-fields of different polarizations. The curves show the variation of optical density in the images across the horizontal and vertical diameters.

and shifts the atom cloud in one arc of the ring, as shown in Fig. 3.7 (b). This result is consistent with the results of calculations performed by incorporating z-component in the rf-field along with the linearly polarized rf-field (x-component). The asymmetry arises due to inhomogeneity of the coupling strength around the ring/toroid. As predicted in an earlier work [77], the position of the potential minimum can be changed by changing the value of phase β of the z-component of the rf-field. Thus, insertion of a phase modulation unit between the two amplifiers driving the single and multi tun coils can be used as a technique to modulate β, and rotate the atom cloud along the toroidal ring [77, 73]. This method of rotation would be more easy than the use of a laser dipole potential to stir the cloud, commonly used for super-fluidity experiments.

3.3.5 Concentric atom trapping clouds using two rf-fields

Exploiting the independent tunability of frequency and amplitude of both the rf-sources, we have subjected an atom cloud trapped in the rf-dressed adiabatic ring potential due to the multi-turn coil to a second rf-field of low amplitude (due to the single turn coil). The

high rf-field amplitude only at lower frequencies (~1 MHz). This makes it possible to use the single antenna and single rf-source for evaporative cooling as well dressing of the atoms in the trap. The Rabi frequency in the multi-turn antennae coil with the frequency of the rf-field is shown in Fig. 3.6. In order to determine the Rabi frequency, peak rf-field strength $|B^{rf}|$ was obtained using a high precision Gaussmeter. During the frequency ramp from 15 MHz to 1 MHz, the rf-field of low amplitude (due to low current in the antenna) is emitted to irradiate the trapped atom cloud in the beginning, which is suitable for rf evaporative cooling. In the trailing part of the ramp (near 1 MHz), a high amplitude rf-field is obtained due to multi-fold increase in the current in the antenna coil. This high amplitude rf-field converts the quadrupole trap into an rf-dressed quadrupole trap which provides ring shaped trapping potential. Figure 3.7 (a) shows a typical image of the cloud trapped in the ring/toroidal rf-dressed potential, using this single coil and single rf-source configuration for rf-dressing purpose. In single coil configuration, the rf evaporation and rf-dressing are achieved starting from $\sim 1 \times 10^7$ atoms at temperature ~250 μK in the quadrupole trap. Finally $\sim 2 \times 10^5$ atoms at temperature of ~40 μK are obtained in the toroidal ring trap. Therefore single coil configuration is more efficient in terms of number of atoms than the double coil configuration. This is an expected result due to adiabatic nature of conversion of quadrupole trap into rf-dressed toroidal trap in the case of single coil configuration.

3.3.4 Formation of tilted ring cloud

As predicted theoretically in the previous chapter, the use of an rf-field with a component along the direction of the quadrupole trap can result in a ring trap of asymmetrical/tilted shape. To verify this, the experiments have been performed using both the single and multi turn coils simultaneously with rf-field frequency ramped down from 15 MHz to 1 MHz. In this case, the rf-field due to multi-turn coil is stronger than the single turn coil. The presence of the z-component of rf-field, destroys the radial symmetry of the ring potential

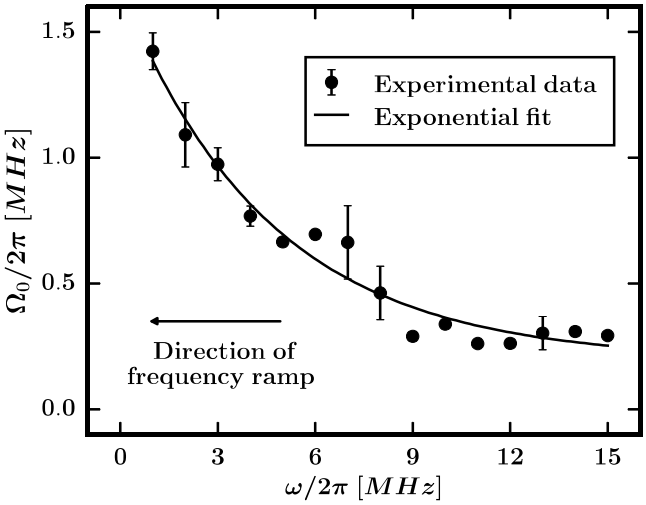

Figure 3.6: Variation in the rf-coupling strength (*i.e.* the peak Rabi frequency, $\Omega_0 = (g_F\mu_B/\hbar)|B^{rf}|$) with frequency, during the frequency variation in the rf-field ramp. The circles show the experimental data and continuous curve shows an exponential fit. The error-bars show the standard deviation between multiple experimental observations.

of the ring shape, the optical density profile along a selected diameter across the image was plotted. The measured optical density profile was fit to two Gaussian profiles at the two ends of this diameter. The peak to peak separation between two Gaussian profiles has been used as the diameter (twice the radius) of the ring. An average over different diameters along different directions was performed to obtain the mean radius of the cloud in the ring shape. The radius values obtained this way are shown in Fig. 3.5, as a function of the rf frequency ω_0 of the dressing rf-field. The experimental (dots) and theoretical (line) values shown in the figure are in reasonable agreement.

3.3.3 Formation of ring trap using single rf source

In further experiments, we have used a multi-turn coil as an rf-antennae for evaporative cooling as well as for generation of the rf-dressed potential for cold atoms. The rf-frequency ($\nu = \omega_0/2\pi$) in this case is ramped down from 15 MHz to 1 MHz linearly in a duration of 5 s. The impedance matching circuit which couples the rf-signal to the antennae is kept resonant near the end of the frequency ramp at 1 MHz. This results in

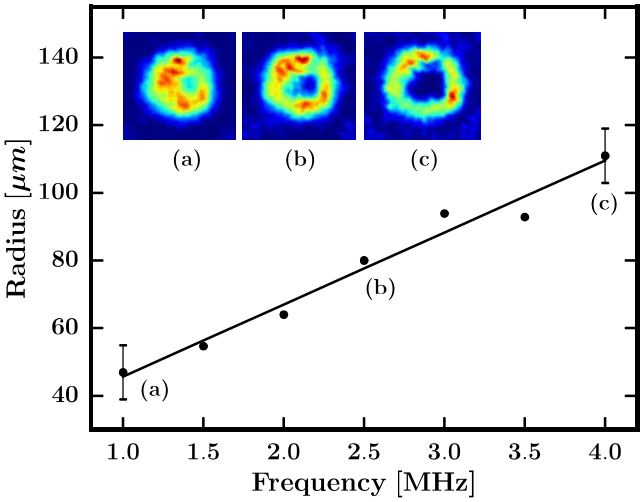

Figure 3.5: Observed variation in the ring radius with frequency ($\omega_0/2\pi$) of the dressing rf-field. Points show the experimentally measured values and the error bars show the deviation in the value in repeated measurements. The line curve represents the theoretical prediction of radius considering experimental parameters. The inset shows the absorption images (optical density) of the atom cloud for different frequencies of dressing field.

is higher than 1 (estimated using the approach described in [49]). Hence the confinement along the z-direction is stronger than that in the radial direction. This indicates that the trapped cloud is quasi-2D type.

Due to the non-uniform potential depth around the toroid, distribution of atom cloud is expected to be non-uniform which is also observed experimentally. The observed asymmetric cloud distribution pattern was shot to shot repeatable, with negligibly small variations in the density distribution. In the measurements, a single image of the cloud was stored and analyzed to retain the original density distribution intact, instead of taking multiple images and then averaging. The measurements were repeated for a number of times to check the reproducibility and derive the statistical errors.

3.3.2 Ring radius measurements

After the trapping of atoms in ring trap, the absorption images of cloud were taken to study the parameters associated with toroidal geometry. To estimate the radius of the atom cloud

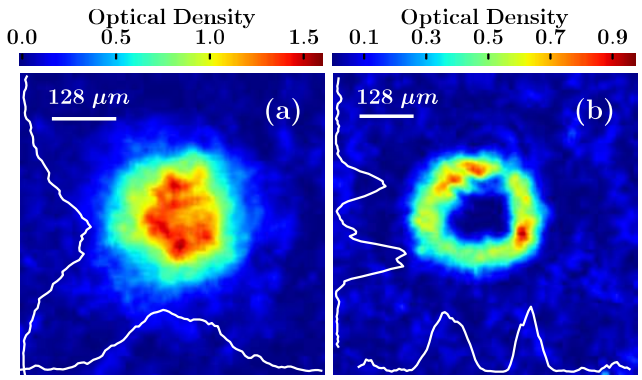

Figure 3.4: Observed absorption images of the cloud (in xy-plane) after evaporative cooling in quadrupole trap: (a) before rf-dressing and (b) after rf-dressing. The curves show the profiles of optical density along the selected diameters across the image. Different colours in an absorption image from blue to red represent the optical density values in the increasing order.

temperature of $\sim$ 20 μK in the quadrupole trap. The increased temperature in the rf-dressed quadrupole trap is expected due to gain in energy by atoms from the modified potential, after the rf-dressing. The number of atoms trapped in the toroidal trap was typically $\sim 1.3 \times 10^5$, giving the transfer efficiency of $\sim$ 50% from quadrupole trap to toroidal trap. Figure 3.4(a) shows the absorption image of the cloud in the quadrupole magnetic trap after the evaporative cooling and before the rf-dressing. Fig. 3.4(b) shows the image of the atom cloud in the rf-dressed trap of toroidal geometry. The low density in the centre of the absorption image of the cloud in the rf-dressed quadrupole trap (Fig. 3.4(b)) shows the trapping of atoms in the toroidal geometry.

One may note that, since the dressing rf-field is linearly polarized, the rf-dressed potential in this case is expected to have a double-well structure on a circular ring, with two potential barriers separating the wells in the azimuthal direction. We have observed the toroidal (or ring shaped) atom cloud because the temperature ($\sim$ 40 μK) of the atom cloud is higher than the height (few μK) of these azimuthal potential barriers. Due to higher temperature, atoms in the cloud can ride the barriers and move throughout the circumference of the ring. In our dressed quadrupole trap, under the harmonic potential approximation near the trap minimum on the ring, the ratio of axial and radial trap frequencies (ω_z/ω_ρ)

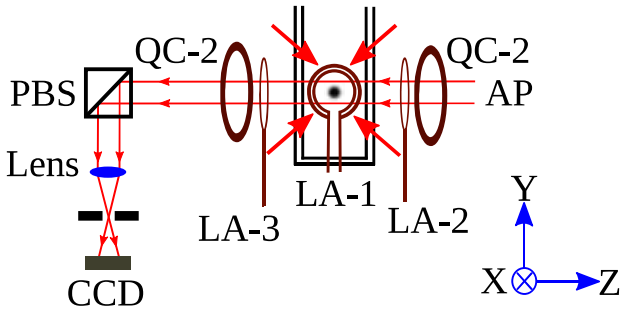

Figure 3.3: Schematic diagram of the magnetic and radio frequency coils setup, QC-2: quadrupole coil for UHV- MOT, PBS: polarising beam splitter cube, CCD: charge coupled device camera, LA-1: multi-turn loop antenna for rf-dressing, LA-2: the loop antenna used for rf radiation, LA-3: pick-up loop antenna, AP: absorption probe beam. The absorption imaging optics is shown in the diagram. The coordinate axes (x, y, z) are also shown.

3.3 Observations on ^{87}Rb atom cloud trapped in rf-dressed potential

3.3.1 Formation of ring trap using two rf-fields

In the experiments, the effect of the applied dressing rf-field on cold ^{87}Rb atoms trapped in the quadrupole magnetic trap has been studied and the coil configuration is shown in Fig. 3.3. To start with, the atom cloud trapped in the quadrupole trap was first evaporatively cooled to reduce the temperature from $\sim$ 250 μK (number of atoms $\sim$ 1×10^7) to $\sim$ 20 μK (number of atoms $\sim$ 2.5×10^5), by applying the rf-field through a single-turn antennae. The rf evaporation is implemented by ramping down the source frequency ($\nu = \omega_0/2\pi$) from 12 MHz to 3 MHz in a duration of 5 s. When this evaporatively cooled atom cloud in the quadrupole trap was exposed to the dressing rf-field emitted from a multi-turn antenna, the trapping of atoms in a toroidal geometry was clearly observed after appropriate adjustment of power in the dressing rf-field. The axis of ring is parallel to the symmetry axis of the trap and also along the imaging direction. The estimated temperature of atoms in the toroidal trap was ~40 μK, which is higher than the initial

3.2.4 Radio frequency dressing of trapped atoms

The rf-field is switched-on after the ^{87}Rb atom cloud is settled in the quadrupole trap for more than 50 ms. This 50 ms time is long enough for untrappable hot atoms to escape the quadrupole trap and generate an equilibrium to remove any undesired observations. The rf-field is ramped to change its frequency from a higher value to a lower value to perform the evaporative cooling and rf-dressing of the atom cloud in the quadrupole trap. In order to achieve the desired outcome, the rf-synthesizers are directly driven by the PC through the GPIB connections. The output of the synthesizers are amplified using rf-amplifiers whose output is connected to copper loop antennaes. The radiation from the antennae is used for the evaporative cooling as well as for the rf-dressing.

3.2.5 Imaging of the atom cloud

A CCD camera (Pixelfly USB, PCO Germany) was used in conjunction with an optical imaging setup to capture the absorption images of the cloud. The camera was connected to the industrial PC via a universal serial bus (USB) interface. The CCD camera had a 2D array of 1392×1024 pixels with the area of each pixel being $6.4\ \mu m \times\ 6.4\ \mu m$. As the absorption probe imaging is an invasive technique, a fresh cycle of experiment starting from MOT loading to rf-field exposure is run to capture the image of the atom cloud after changing any experimental parameter. In each experimental cycle, the atom cloud image is recorded by setting an appropriate delay in CCD trigger with respect to start of the frequency ramp of rf-field.

of 20 ms.

3.2.2 Optical molasses and optical pumping

The compressed MOT stage is followed by an optical molasses stage, in which the the magnetic field is switched off and the detuning of cooling laser beams is increased from -5Γ to -7.5Γ. The removal of the magnetic field helps the atoms to cool further from the compressed MOT stage to allow to reach $\sim 40\mu K$ temperature. This reduction in temperature increases the loading efficiency of the cold atom cloud in the quadrupole magnetic trap.

In order to increase the loading efficiency of the quadrupole trap further, an optical pumping stage is performed. In presence of a small magnetic field of $\sim$ 2 G, a laser beam of σ^+ polarization with respect to the magnetic field direction induces the population transfer between Zeeman sub-levels which pump the atoms to the state $|5S_{1/2}, F = 2, m_F = 2\rangle$. This state is the most trappable state of all the five Zeeman hyperfine sub-levels of state F=2. This optical pumping stage lasts for 500 μs.

3.2.3 Loading of quadrupole magnetic trap

After the optical pumping stage, the current in the UHV-MOT coils (*i.e.* quadrupole trap coils) is switched-on (0 to 15 A in 2 ms) to trap atoms in the magnetic trap with a radial gradient of $\sim$ 75 Gcm^{-1}. Subsequently, the current in the quadrupole trap coils is ramped slowly in a 1 s duration from 15 A to 23 A, to increase the radial field gradient from ~75 to ~115 $G\ cm^{-1}$. This completes the formation of the quadrupole trap. The atom cloud in the final quadrupole trap has $\sim 1\times10^7$ atoms with an approximate temperature $\sim$ 250 μK and trap lifetime of ~18 s.

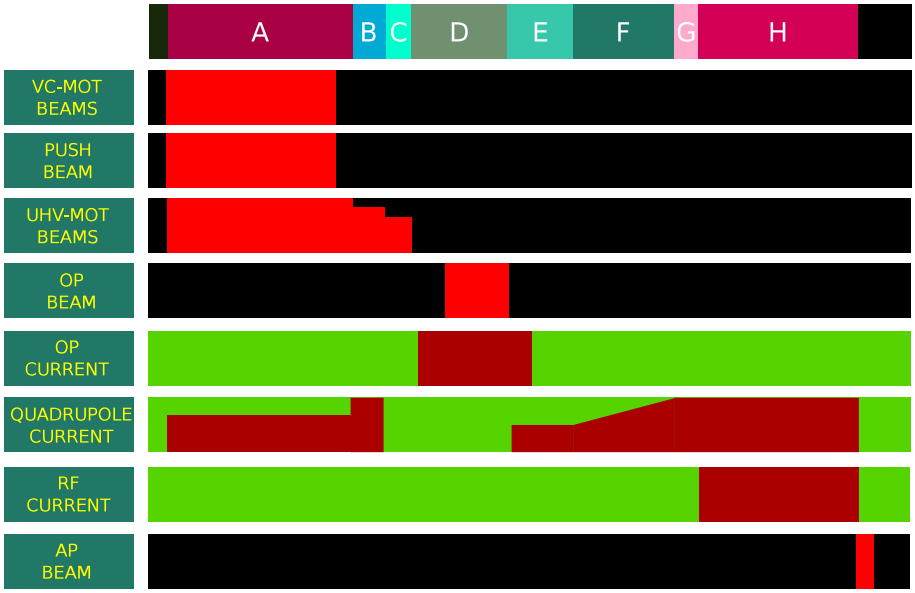

Figure 3.2: Experimental pulse sequences. A: MOT operation; B: Compressed-MOT operation; C: Optical molasses formation; D: Optical pumping operation; E: Quadrupole trap initialization; F: Quadrupole trap ramping; G: Quadrupole equilibration; H: RF coupling.

3.2.1 Formation of magneto-optical traps

As the first step in the experiments, VC-MOT was loaded from the background *Rb* vapor in the octagonal vapor chamber using the three retro-reflected laser beams in presence of a magnetic field gradient of 4 Gcm^{-1}. The VC-MOT acts as a source for loading the UHV-MOT. To load the UHV-MOT from this VC-MOT, atoms are transferred simultaneously using a 1 GHz red detuned focused push beam for a duration of $\sim$ 20 s. The UHV-MOT has higher number of atoms ($\sim 2 \times 10^8$) than the VC-MOT ($\sim 1 \times 10^8$). The typical temperature of the cloud in MOTs at this stage is in range 200 to 400 μK.

In order to increase the density of the atom cloud, an instantaneous compression of the UHV-MOT is performed after the complete loading of the UHV-MOT. This compression of the MOT has been achieved by the introduction of larger detuning of the cooling laser beams along with the increase in the magnetic field gradient. During this compressed MOT stage, the detuning of the cooling laser beams are increased from -2.5Γ to -5Γ, along with the increase in the magnetic field gradient from 6 to 8 Gcm^{-1} in a time duration

3.1.4 Controller system

The generation and manipulation of the cold atoms in the rf-dressed traps, a series of steps were required to be performed with an accurate temporal sequence. This was accomplished by a control system programmed through a PC. The generation of magneto optical traps, loading atoms in the quadrupole trap and finally loading the rf-dressed trap after the forced rf-evaporative cooling of the atoms in the magnetic trap. The controller system controlled various instruments such as accousto optic modulators, mechanical shutters, power supplies and rf-synthesizers. The in-house designed electronic control system facilitated the control of the complete setup from a computer front-end with the help of a number of field programmable gate array (FPGA) cards programmed by the LabVIEW software. The FPGA cards were connected to a control system consisting data acquisition (DAQ) cards which in turn provided all the analog and digital outputs with controllable amplitude and pulse sequences. These analog and digital control outputs were fed to the AOM modules, shutter module, power supplies and CCD cameras to perform the desired functions with as low as 1 μs time resolve capabilities.

3.2 Sequence of experimental procedure

The complete experimental procedure involves execution of a series of tasks with the help of the electronic controller system described above to trigger and operate all the instruments in desired sequence. The time delayed sequences which were used in the experiments are shown in Fig. 3.2 (not to actual time scale). The different steps used in the experiments are discussed as follows [76].

3.1.3 Magnetic trap and rf-field sources

The coils for the VC-MOT operation had an external diameter of 66 mm and internal diameter of 57 mm having 150 turns in each and separated by 55 mm from each other. With a current flow of 3 A the generated radial quadrupole field gradient for VC-MOT was 10 Gcm^{-1}. The UHV-MOT coil was used for generating the quadrupole magnetic trap apart from the MOT preparation. Each UHV-MOT coils had an external diameter of 70 mm and internal diameter of 34 mm. These coils each with 230 turns were kept at a distance of 46 mm and produced the 10 Gcm^{-1} with 1 A current. Due to the large current passing through these UHV-MOT coils during the operation of the quadrupole trap, the copper windings of these coils were surrounded by a heat resistant jacket with water cooling facilities to remove the generated heat. A low current power supply was used to provide a smaller magnetic field at the time of optical pumping of the trapped atoms through another set of Helmholtz coils. The three different power supplies all connected to an insulated gate bipolar transistor (IGBT) based high speed switching circuit were used to achieve fast switching of currents in coils used for magnetic trapping. Two of the power supplies (Xantrex make) delivered high current to the pair of anti-Helmholtz coils surrounding the glass cell of the UHV-MOT to provide the magnetic fields required for the functioning of the magneto-optical trap and quadrupole magnetic trap.

The rf system consisted two different rf-synthesizers (Agilent 335220A and 33522A) which were connected to two different rf-amplifier systems. One of these two amplifiers, one broadband amplifier was connected to an inductance matching circuit to balance the input impedance with that of the rf-coil connected to it. This inductance matching circuit had a gain profile peaking at the 1 MHz frequency. The other amplifier was built in-house to perform optimized evaporative cooling in the magnetic trap.

probe beam, is detected on a photo diode. Due to the higher strength of the pump beam, the population in the ground state gets depleted and the absorption of the probe beam gets reduced for the zero velocity group atoms. Hence the obtained frequency scanned spectrum observed in the oscilloscope shows transmission peaks at the frequencies where the probe beam is resonant with the hyperfine levels. In case of the other velocity group atoms, the absorption of the probe beam prevails while the frequency of the probe beam seen by the atoms is Doppler shifted. A situation may also arise in which the Doppler shifted frequencies of the probe and the pump beams match with each other. This can provide a transmission peak in the observed spectrum, commonly known as the cross-over peak. In order to lock the laser frequency near any of these particular transmission peaks, the SAS spectrum serves as a reference signal.

The laser beams were passed through the accousto optic modulators (AOMs) in a double pass arrangement, in which the first order of the diffracted beams were propagated further after blocking the zeroth order. The AOM driver module was capable to operate in CW or pulsed mode while being able to shift the frequency of the laser beam in a total range of 200 MHz and vary the power of the laser beam from a maximum value to a negligible level. This power variation mechanism enabled us to use these AOM's as switches to initiate or stop any beam for any desired interval during the experimental procedure.

Though the AOM's were used for performing the switching operations, the complete removal of the light from AOM seemed impossible during the magnetic trapping of atoms. To remedy the situation, a secondary switching mechanism was also employed by the means of a series of mechanical shutters. These mechanical shutters were switched ON using trigger pulses (5 V) with the default state being OFF. The trigger pulse controlled the driver circuit which in turn operated the knife edges attached to the solenoid based actuators.

with 9 mW power and 6 mm $1/e^2$ diameter were used to form the UHV-MOT. Two more laser systems (150 mW Toptica DL-100 and 100 mW Sacher) were used to derive two re-pumping laser beams operating in the $F = 1 \rightarrow F' = 2$ transition of the ^{87}Rb atoms. These re-pumping beams were mixed with cooling laser beams headed towards the vapor chamber and glass cell.

The loading of the UHV-MOT in the glass cell was achieved by transfer of atoms from the VC-MOT [75]. The transfer of the atoms from the VC-MOT to the glass cell was facilitated by the use of a pushing laser beam (PB) which was derived from a laser (150 mW Toptica DL-100) operated at 1 GHz detuning from the $F = 2 \rightarrow F' = 3$ transition (*i.e.* cooling transition) of ^{87}Rb atoms. The initial $1/e^2$ diameter of the push beam was 2 mm with a power of 25 mW. To generate the dipole radiation force, the beam was focused with a 300 mm lens to a diameter of 35 μm on the VC-MOT cloud to eject a flux of atoms from the VC-MOT.

The optical pumping (OP) beam, required for necessary state preparation for magnetic trapping, was obtained by mixing one beam derived from the master laser and one from the re-pumping laser (DL-100) to transfer atoms to $5S_{1/2}|F = 2, m_F = 2\rangle$ state. The final optical pumping beam had a $1/e^2$ radius of 3 mm with a power of 500 μW and a polarization of σ^+ with respect to an applied magnetic field along the z-direction.

Another beam with 2 mW power was derived from the master laser to perform the absorption imaging of the atom cloud. The expanded absorption imaging beam had $1/e^2$ radius of $\sim$ 6 mm. A 100 μm diameter aperture was used at the focal position of the expansion optics to achieve a good quality beam through spatial filtering.

In order to fix the laser beam frequencies at the desired transitions, all the lasers were stabilized using the saturation absorption spectroscopy (SAS) technique. In the SAS technique, the Doppler broadening of the spectral features were eliminated by using two counter propagating beams derived from the same laser source. Of these two beams, one is more stronger than the other one and act as a pump beam. The weaker beam, used as a

(de-gassing). Also at this stage, the NEG pump was activated with a repeated flow of current of 6 to 8 A through the module. Finally, after the completion of the baking stage, the gate valve connected with the TMP was closed to isolate the TMP from the vacuum chambers and the vacuum system was allowed to cool to reach the required pressure at room temperature (always kept fixed at 20°C). All the SIPs are kept in switched on condition to maintain the vacuum at the particular pressure.

3.1.2 Laser systems and optical layout

A collection of four extended cavity diode laser (ECDL) systems, all operated at the D2 transition line of ^{87}Rb atoms (*i.e.* $\sim$ 780 nm), along with a plethora of different optical elements like polarizing beam splitters (PBS), half and quarter wave plates, mirrors and lenses comprised the whole optical system. The main part of the ECDL system is a semiconductor laser diode housed in the diode holder and is provided a stabilized current supply. The base of the diode holder serves as a heat sink which is mounted on Peltier coolers to provide necessary cooling to achieve desired temperature for laser diode. The output emission of the laser diode is incident on a grating controlled by a piezoelectric transducer (PZT) to provide necessary frequency tunning. The output of the laser system is obtained through the beam steering mirror which is finally collimated through a lens combination. To protect the semiconductor diode from backscattered light, a Faraday isolator was also installed in front of the output laser beam.

The output of a master laser (150 mW Toptica DL-100) was fed to a tapered amplifier (Toptica TA Boosta) to obtain an output power of almost 700 mW which was split in two halves to deliver laser beams to both the magneto optical traps formed inside the vapor chamber and the quartz cell. In the octagonal vapor chamber, three laser beams of $1/e^2$ diameter $\sim$ 7 mm and individual power $\sim$ 20 mW in each beam were used in a retro-reflecting configuration to realize the vapor chamber magneto optical trap (VC-MOT). In case of the magneto optical trap formed inside the glass cell, six laser beams each

sufficient vapour inside the chamber to allow the formation of magneto-optical trap in the chamber (called VC-MOT) when laser beams and magnetic fields are applied.

The second part of the vacuum system is a stainless steel hollow cube with six ports each of which has a dimension of NW35CF. The octagonal chamber was connected to this cube at one port through a differential pumping tube of length 122 mm. To the opposite part of the cube, a glass cell (Optiglass, UK) was connected. The base pressure in the glass cell was 10^{-11} achieved, in which the experiments like formation of UHV-MOT, magnetic trapping and rf-dressing were performed. To create a pressure gradient between the octagonal chamber and the cube, the inner diameter of the differential pumping tube was kept at 2.25 mm for the initial 60 mm from the octagonal chamber side and the rest of the tube was with 5 mm inner diameter. A combination pump consisting an SIP of 150 liter/sec with a non-evaporable getter (NEG) pump module (VacIon plus 150 l/s starcell, Varian) was connected to one of the open ports of the six way cube. An independent NEG pump (GP-100 MK5, SORB-AC MK5 type cartridge pump from SAES getters, Italy) was also connected to the cube. To monitor the pressure inside this cube an extractor type gauge (Oerlikon leybold) was used.

In order to reach the desired vacuum in both parts of the vacuum system, a series of steps were followed for more than a week. A brief summary of these steps is as follows. Initially the TMP connected to the octagonal chamber was switched on along with a rotary pump acting as a roughing pump and was kept on for almost 24 hours. This method reduces the pressure in the octagonal chamber to $\sim 10^{-7}$ Torr and in the cube to $\sim 10^{-4}$ Torr. After the completion of this step, the complete vacuum chamber is baked at 200°C for almost a week using heating strips wrapped on the chamber covered with protective Al foil layers. The covering with the Al foil also provides equal distribution of the heat throughout the vacuum system. The glass cell, being fragile, was heated using a non-contact hot air blower type heater. During the final stage of the baking procedure, the SIP was also activated to remove the gas particles adsorbed in the inner parts of the pump

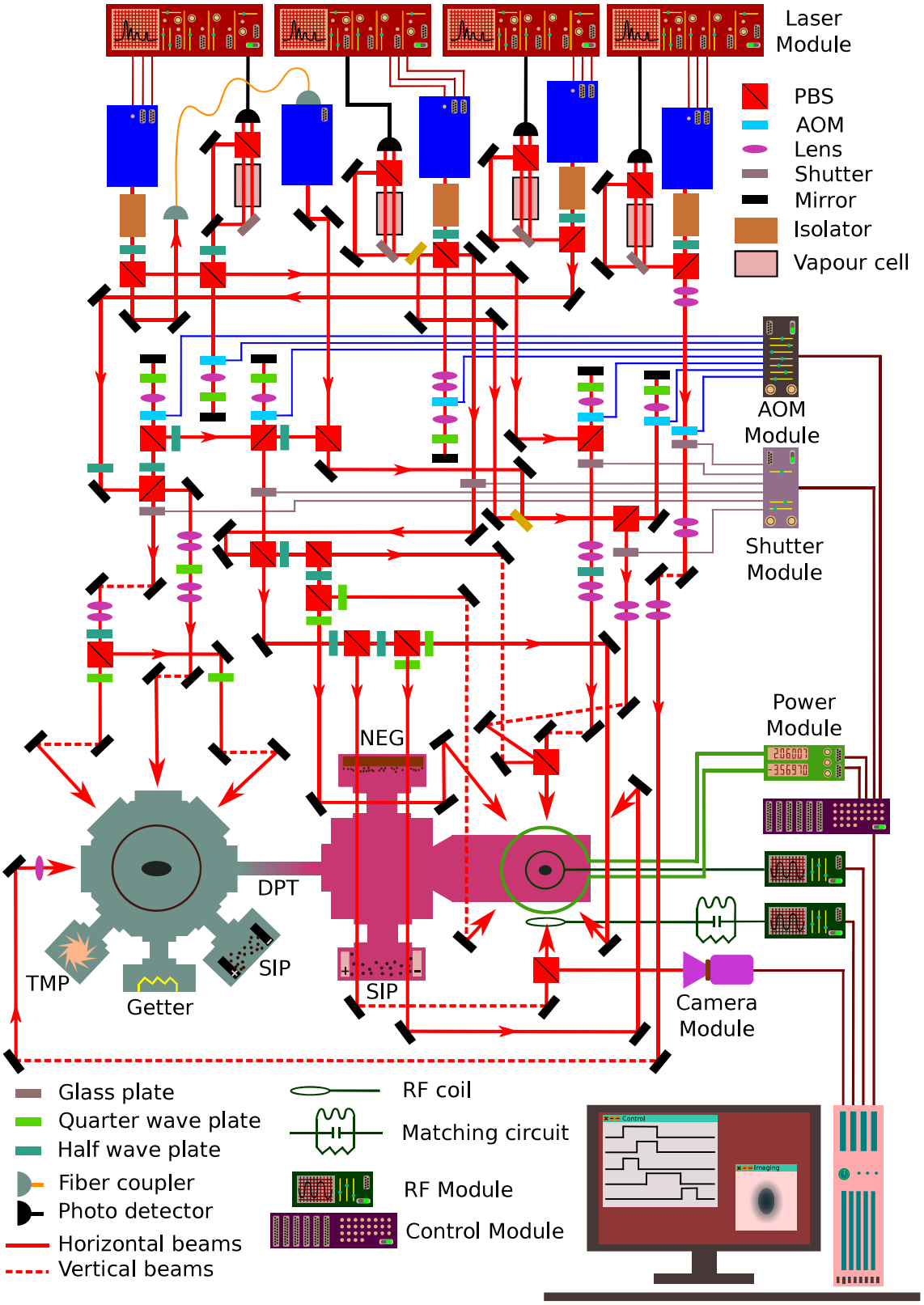

Figure 3.1: Schematic diagram of the experimental setup.

described. In particular, the results on demonstration of rf-dressed potential with toroidal geometry for cold ^{87}Rb atoms are highlighted here. The results on the variation of the radius of the toroidal trap with rf-field frequency are also presented in this chapter.

3.1 Experimental Setup

The experimental setup used to realize some of the radio frequency dressed potentials outlined in the previous chapter is experimentally realized in a setup shown in the schematic diagram of Fig. 3.1. The schematic has accommodated all the major segments, namely, the vacuum system,the optical system, and the electronic control system. A detailed description of the different segments is provided as following.

3.1.1 Vacuum systems

The vacuum system of the experimental setup consists of two separate parts along with different pumps and gauges [74]. The first part of the vacuum system is an octagonal stainless steel (SS) chamber with ten faces having knife-edges of different sizes. There are eight faces with size NW25CF and two faces with size NW63CF. A turbo molecular pump (TMP) of 70 liter/sec (Turbo-V70LP, Varian) is connected with a pneumatic gate valve of NW63CF size to one of the faces of the octagonal chamber. A sputter ion pump (SIP) of capacity 20 liter/sec (VacIon starcell) is also connected to this octagonal chamber for pumping the chamber to a base pressure of 10^{-8} Torr using a SS T-joint. To monitor the pressure inside the vacuum chamber a Bayerd-Alpert gauge is used. To dispense Rubidium atoms inside the octagonal chamber, a getter module was connected through a T-joint of NW35CF dimension. The getters (Rb/NF/3.4/12 FT10+10, SAES getters) were welded on a copper feed-through via brazed SS strips before fixing the feed-through on the T-joint. The getters were activated using a DC power supply (Testronix 0-15 V/ 0-10 A) with a driving current ranging from 2.5 A to 4.1 A. This gave rise to generation of

Chapter 3

Experimental realization of rf-dressed potentials for cold ^{87}Rb atoms

The experimental realizations of the ring shaped atom traps have been reported by several groups in recent past employing various techniques [64, 65, 66, 67]. These reports also include the use of a specially designed magnetic coils for a ring shaped quadrupole trap [68], an rf-dressed magnetic trap in combination with a standing wave pattern of an optical beam [69], an rf-dressed magnetic trap in combination with a sheet type dipole laser beam [52] and an optical dipole traps using Laguerre Gaussian beams [70]. The use of a time orbiting potential superimposed with a strong rf field to generate the rf-dressed ring potentials appears promising compared to other techniques [71, 50, 72, 53, 73]. One of the many reasons for developing ring traps is to study the superfluid behaviors in periodic boundary systems [57, 58] and the physics of degenerate gases in low dimensions [51, 49].

In this chapter, the description of the experimental setup and the experiments performed to verify some of our theoretical results obtained in the previous chapter are presented. The techniques employed by us, discussed in this, promises easier implementation to realize ring traps using time varying rf-fields. The experimental setup, the sequence of experimental steps, the trapping in the rf-dressed potentials and various measurements are

background collisions (life time ~ 18 s).

It is evident from these experimental observations (Fig. 4.8) that rf-dressed trap holds more number of atoms than the bare quadrupole trap, implying lower loss of atoms in rf-dressed magnetic trap. The results of comparison between the rf-dressed trap and the bare trap (Fig. 4.8) clearly establish the working of the rf-dressing in our experiments. The rf-dressed traps of this kind can be useful for trapping atoms in different geometries and performing evaporative cooling to achieve degeneracy in the cold gas samples in unconventional potential landscapes [52, 85, 43, 90].

4.5 Conclusion

We have studied the time evolution of an atom cloud exposed to the time varying rf-dressed potential. The experimental observations have been qualitatively explained by the numerical simulations involving DSMC method. These numerical simulations can be used to understand the evolution of an atom cloud with more sophisticated variations in the potential. The lower loss rates observed in the rf-dressed potentials is also useful to achieve quantum degeneracy in these exotic potentials.

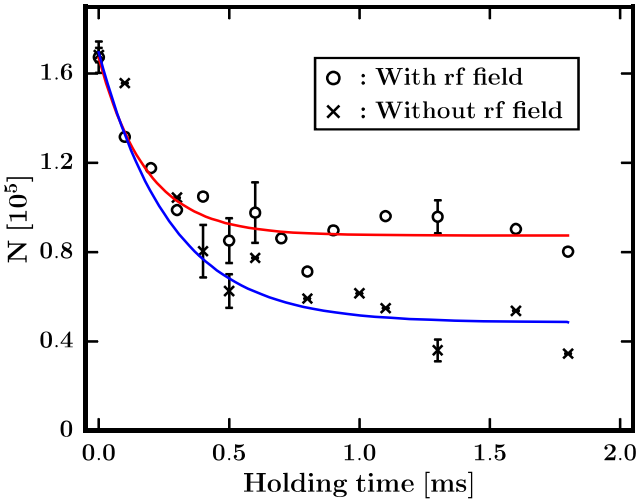

Figure 4.8: Measured variation in number of atoms with holding time. Circles show number of atoms trapped in the rf-dressed quadrupole trap and crosses show number of atoms trapped in the bare quadrupole trap. Error bars are shown for some data points generated after repeated measurements. The continuous curves are to guide eyes.

For a comparison with the bare quadrupole trap, the rf-field was switched-off after the completion of the rf-field ramp, and number of atoms was measured again as a function of holding time. These data are shown by crosses in Fig. 4.8.

In case of the rf-dressed trap, the initial fast decrease in number of atoms with time has been observed which later slowed down. this loss in the rf-dressed trap has been earlier attributed to an evaporation process via Landau-Zener losses at positions of weak rf-coupling [89]. We believe that similar mechanism could be responsible for the initial fast decrease in number of atoms in the rf-dressed trap in our case also (Fig. 4.8) and slowly become weak as the cloud gets colder.

However a different mechanism can be visualised for the high loss of atoms (occurring initially) in the bare trap (shown by crosses in Fig. 4.8). Since the rf-dressed states are superposition of trappable as well as untrappable magnetic hyperfine spin states, the bare trap rejects atoms in untrappable states, leading to high loss of atoms when rf-dressed atoms are left in the bare quadrupole trap. At longer holding time, the slow variation in number of atoms with time in both the traps can be attributed to the loss limited by

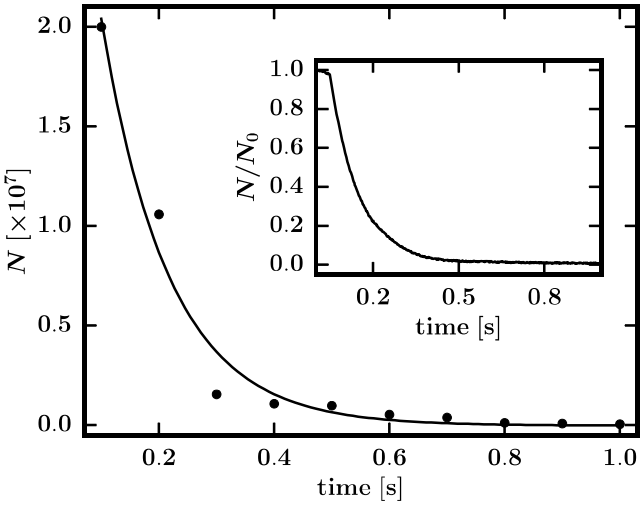

Figure 4.7: The experimentally measured variation in number of atoms (circles) in the trapped cloud with time when frequency of dressing rf-field was varied from 15 MHz to 1 MHz in 1 sec duration. The continuous curve is exponential fit to the data and guide to eyes. The inset shows a similar variation obtained from simulations for $N_0 = 1 \times 10^5$ atoms.

number of atoms in the trap (as shown in Fig. 4.7), with final number of atoms remaining in the trap after 1 sec was only 0.2% of the initial number. At the same time, the formation of the cloud ring was poor. The numerical simulations for this fast rf ramp (*i.e.* 1 sec) have also provided the similar results, which shows the ability of our simulation to handle such a fast and non-equilibrium trap dynamics.

4.4 Evolution after trap formation

Next, we studied the loss of number of atoms with time trapped in the rf-dressed potential after the complete formation of the rf-dressed trap (*i.e.* life time in steady state rf-dressed trap). For these measurements, atoms trapped in the quadrupole trap were first exposed to an rf-field of changing amplitude and frequency as shown in Fig. 3.6, and then at the end of the frequency ramp, the rf-field was left ON at 1 MHz frequency, and number of atoms in the trap was measured as a function of time (holding time). The measured variation in number of atoms in this rf-dressed trap with holding time is shown by circles in Fig. 4.8.

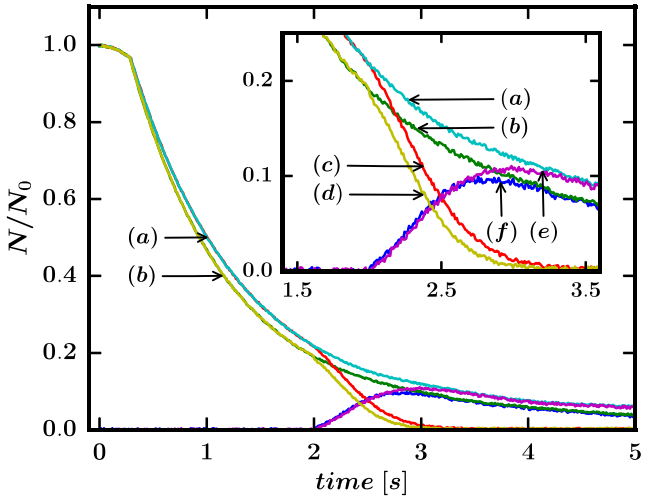

Figure 4.6: Results of numerical simulations showing the variation in number of atoms with time during the ramp down of rf-field frequency. The curves (a), (c) and (e) show results of simulations for initial number N_0=1 $\times$ 10^6, whereas (b), (d) and (f) show the results for 1 $\times$ 10^5. The curves (c) and (d) show number of atoms in $|m_F = -2\rangle_A$ state whereas (e) and (f) show atom numbers in $|m_F = 2\rangle_A$ state. The inset shows the magnified view of the evolution of number of atoms in different states.

in the loss rate during the ramp process, with a higher loss rate in the beginning of the ramp than that towards the end of the ramp (Fig. 4.6). These results of simulations are similar to the experimental observations depicted in Fig. 4.4. This is indicative of the trapping atoms in rf-dressed potential towards the end of the ramp, after initial loss due to rf-field induced evaporation. The rise of population in $|m_F = 2\rangle_A$ state in Fig. 4.6 after 2 sec is further confirming this argument. Towards the end of the rf ramp, the population in $|m_F = -2\rangle_A$ state drops to an extremely small fraction of the initial total number of trapped atoms, whereas population in $|m_F = 2\rangle_A$ state reaches the maximum value and becomes the sole contributor to the trapped atom cloud. In addition to this, the hollowness of the atom cloud in Fig. 4.5 also suggests the trapping of atoms in the potential landscape of the dressed state $|m_F = 2\rangle_A$.

In order to explore the results with a more fast ramp of the rf-field, the experiments were conducted on same setup and the rf-ramp of frequency from 15 MHz to 1 MHz was completed in just 1 sec duration. This fast ramping resulted in much faster decrease in the

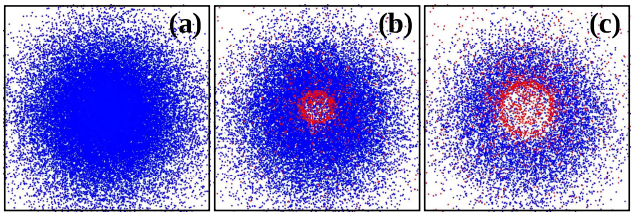

Figure 4.5: Simulated atom cloud pictures at different instants of time during the rf-frequency ramp from 15 MHz to 1 MHz in 5 sec. The simulation results are for initial number of atoms 5×10^4 at temperature 200 μK in quadrupole trap. The blue colour dots represent particles in the $|m_F = -2\rangle_A$ state and red dots represent particles in $|m_F = 2\rangle_A$ state. The ring with red dots indicates the cloud trapped in the toroidal geometry. Figures (a) to (c) show the simulated cloud shapes as frequency ramp progresses.

chosen close to their experimental values, except the number of atoms. The number of atoms was lower than the experimental value due to the limited computational speed. At each time interval, the total number of trapped atoms were calculated by the region of interest method, described in the earlier section along with their state. To start with, all the atoms are considered in $|m_F = -2\rangle_A$ state, which is confined by an rf-dressed state potential having a single minimum at the quadrupole trap center as shown in Fig. 4.5 (a). The atom cloud in this potential has a nearly Gaussian profile for the number density, similar to that in the bare quadrupole trap. As the frequency of rf-field is changed during the ramp of the rf-field, the parameters of the rf-field responsible for trapping of atoms in the state $|m_F = -2\rangle_A$ changes as shown in Fig. 3.6. Initially at high frequency and low amplitude of rf-field, the evaporation process takes place which removes atoms having velocity higher than the average velocity. As the frequency decreases and the amplitude increases further, the non-adiabatic LZ transition probability to $|m_F = 2\rangle_A$ state is increased. This results in trapping atoms in a different potential landscape corresponding to this new state $|m_F = 2\rangle_A$, which is reflected in the number density and cloud shape. Fig. 4.5 (b) and (c) shows the simulated evolution in the shape and number density distribution of the simulated atom cloud.

Fig. 4.6 shows the simulated variation in the number of atoms trapped during the ramp of rf-field amplitude and frequency. An important feature observed here is the change

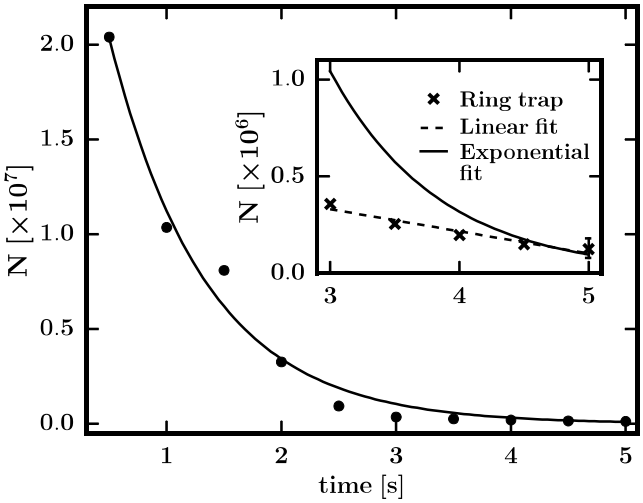

Figure 4.4: The measured variation in number of atoms (dark circles) in a trapped cloud during the rf-field ramp from 15 MHz to 1 MHz in 5 sec duration. The initial faster decay of number of atoms in the trap bears the signature of the rf induced forced evaporation, whereas the slow variation at the trailing edge shows the trapping of atoms in the rf-dressed potential with lower losses. The continuous curve shows the exponential decay in number of atoms. The inset shows the magnified view of the evolution of number of atoms in the rf-dressed ring potential.

the rf-dressed potential of modified landscape. Low loss rates in this potential landscape is also expected due to low Majorana losses in the rf-dressed trap, due to atoms being located away from the quadrupole trap center.

4.3 Numerical results and comparison with experimental observations

In simulations, we have considered the interaction of ^{87}Rb atoms, trapped in a quadrupole magnetic trap, with an rf-field having a time varying amplitude and frequency similar to the one used in the experiments (refer Fig. 3.6). We start from an atom cloud with randomized Gaussian distribution both in position and momentum spaces, where the rms width parameters (σ_i,σ_{v_i}, $i = x, y, z$) are governed by the temperature of the cloud ($200\mu K$) and the magnetic field gradient of the trap. All the parameters used in the simulations were

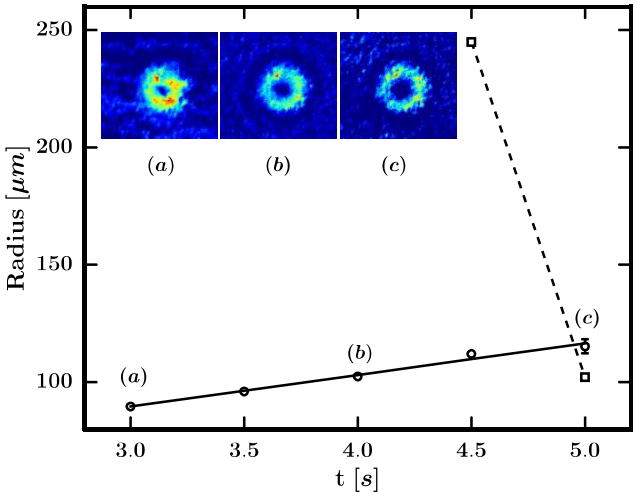

Figure 4.3: Observed variation in the ring radius with time during the evolution of the dressing rf-field. Points show the experimentally measured values and the error bars show the deviation in the value in repeated measurements. The solid line represents the linear fit whereas the dahsed line shows the steady state theoretical values of radius. The inset shows the absorption images (optical density) of the atom cloud at different times of evolution.

by the rf-field frequency alone as the Rabi frequency is strong enough to trap atoms in rf-dressed potentials. This final radius of the atom cloud (at $t \approx 5$ s and $\omega_0 \approx 2\pi \times 1MHz$) is in reasonable agreement with the theoretically predicted value of radius (dashed curve in Fig. 4.3) for a steady state cloud at that value of frequency.

In the experiments the atom cloud shows a fast decrease in number of trapped atoms with time, in the beginning of the rf-field ramp. This bears the signature of forced evaporative cooling of the atom cloud. However, in the later part of the ramp, as the frequency of rf-field reaches to $\sim$ 6 MHz at time $\sim$3 sec, the exponentially increasing coupling strength dominates to modify the potential landscape. The modified potential is dominated by rf-dressed potential with different spatial variation than that of the quadrupole trap potential at the high value of coupling strength. The trapping of atoms in the rf-dressed potential is also reflected in the reduced loss rate of atoms after 3 sec of frequency ramp, as shown in Fig. 4.4. Reshaping of the atom cloud, with low density in the central region, after a duration of 3 sec (Fig. 4.2, images (e)-(j)) is a clear signature of trapping of atoms in

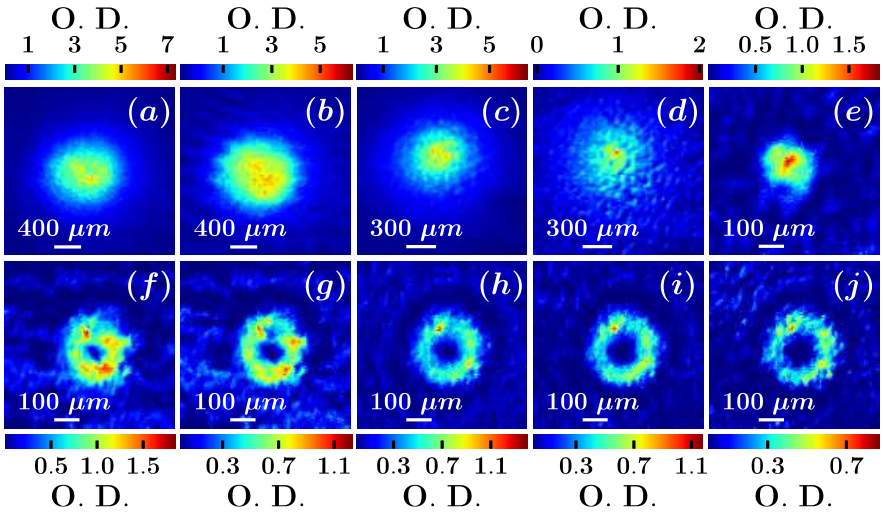

Figure 4.2: Experimentally observed absorption images of the cold atom cloud at different instants of time after starting the ramp of the rf-field : (a) t = 0.5 sec, (b) t = 1.0 sec, (c) t = 1.5 sec, (d) t = 2.0 sec, (e) t = 2.5 sec, (f) t = 3.0 sec, (g) t = 3.5 sec, (h) t = 4.0 sec, (i) t = 4.5 sec, (j) t = 5.0 sec. The colours from blue to red in all the images show optical density in increasing order.

in the rf-dressed potential $|F = 2, m_F = 2, 1\rangle_A$ whose minimum lies around the ring.

Fig. 4.3 shows the variation of the ring cloud radius during the process of frequency ramp of the rf-field. The radius of the ring trap increases linearly with time (*i.e.* decreasing with frequency) during the rf ramp down process. This is because of temporally varying potential with which the atoms are interacting during the frequency ramp down process. With a steady state potential, the variation of ring radius of the trapping potential and the trapped cloud is expected to be linearly increasing with the frequency of dressing rf-field [88], as shown by the dashed line in Fig. 4.2. The observed increase in the radius of ring with time during the frequency ramp down can be understood as follows. In the higher frequency regime, *i.e.* in the beginning of ramp, the lower field strength limits the height of the central hump in the adiabatic potential which is not sufficient to push atoms away from the trap center (Fig. 4.2). As frequency decreases during the ramp, the field strength increases which gives rise to an increase in the potential hump at the trap center and results in the cold atoms moving away from the center. Finally towards the end of rf-ramp, when rf frequency is stabilized to the final value, the radius of the ring potential is governed

the physical ones. To minimise these fluctuations, simulations are repeated for a number of times and average results are used for the study.

4.2 Experimental observations on time evolution of atom cloud trapped in rf-dressed potentials

We have studied experimentally, in the time resolved measurements, the evolution of the shape of the atom cloud during the variation in the rf-dressed potential for atom trapping arising due to the ramping of the rf-field amplitude and frequency. During the ramp of the rf-field in our experiments, the frequency ($\omega_0/2\pi$) of the rf-field from synthesizer was varied linearly with time, from 15 MHz to 1 MHz in 5 sec duration. By using an appropriate impedance matching circuit, the rf-field amplitude B_0^x increased exponentially from 0.1 G to 2 G during the above variation in the rf-field frequency. Fig. 3.6 shows the variation in the rf-field strength (in terms of peak Rabi frequency $\Omega_0 = (g_F\mu_B/\hbar)|B_0^x|$) as a function of the rf-field frequency ($\omega_0/2\pi$), during this frequency variation from 15 MHz to 1 MHz in 5 sec duration. After this ramp of the rf-field, we have observed that the spherical atom cloud trapped in the quadrupole trap gets the shape of a ring or toroid. The high value of Rabi frequency associated with the strong rf-field enhances the non adiabatic Landau Zener tunneling rate that transfers atoms to trappable dressed state $|m_F = 2\rangle_A$ from the other states. As a result of the rf ramp, the temperature of the atom cloud reduces to $\sim 40\,\mu K$ in the rf-dressed trap, after the evaporative cooling phase, from the initial ~ 200 μK temperature in the quadrupole trap.

As evident from the Fig. 4.2 (a)-(e), the size of the atom cloud decreases as a function of time (with decreasing frequency of the rf-field) while no noticeable change arises in the shape of the cloud. After 3 second of evolution, a low density at the center of the atom cloud appears and this region of low density increases with time as shown in Fig. 4.2 (f)-(j). The appearance of the hollow center in the cloud is a signature of trapping the atoms

i^{th} atom in the ensemble,

$$\begin{aligned}
\mathbf{q}_i &= \mathbf{r}_i(t) + \frac{\Delta t}{2m}\mathbf{p}_i(t), \\
\mathbf{p}_i(t+\Delta t) &= \mathbf{p}_i(t) - \Delta t \nabla_{q_i} V(\mathbf{q}_i, t), \\
\mathbf{r}_i(t+\Delta t) &= \mathbf{q}_i + \frac{\Delta t}{2m}\mathbf{p}_i(t+\Delta t).
\end{aligned} \tag{4.5}$$

After deriving the new phase space coordinates of all the atoms in the ensemble, the collisions are considered by calculating the collisional probability between the ith and j^{th} atom in a cell as,

$$P_{ij} = \alpha \frac{\Delta t}{\Delta V_c} v_r \sigma(v_r), \tag{4.6}$$

where α denotes the ratio between the number of test particles to the actual number of atoms simulated, ΔV_c is the volume of the cell and $\sigma(v_r)$ is the total cross section. The actual collision event is then performed based on an acceptance-rejection method. The momentum components of the colliding atoms are then updated with new momentum values calculated from the classical momentum conservation principle. Repeating this procedure over all the time steps constituting the total simulation time results in the complete dynamics of the atom cloud in the trapping potential.

Further, the DSMC method calculates all the positions of all the atoms, irrespective of whether an atom, after the simulation contributes to the formation of the cloud or not. Hence a region of interest is set to count the number of atoms in the vicinity of the main atom cloud. This region is taken wide enough to avoid any critical dependence of the atom number on the selected region. Hyperfine spin states are treated semi-classically with all the atoms initially in the sate $|m_F = -2\rangle_A$ and any atom changes its state only when the transition probability P_{LZ} for the corresponding atom passes an acceptance-rejection algorithm.

We note that finding solution of Eq. (4.5), instead of solving Eq. (4.1) which describes the continuous evolution of the distribution $f(\mathbf{p}, \mathbf{r}, t)$, can result in fluctuations other than

where the scattering function $f_{sc}(\theta)$ is given as,

$$f_{sc}(\theta) = \frac{\hbar}{imv_r} \sum_{l=0}^{\infty} (2l+1)(e^{2i\delta_l} - 1)P_l(cos\theta), \tag{4.4}$$

with v_r being the relative velocity of colliding particles, δ_l being the phase shift associated with partial wave of order l, $P_l(cos\theta)$ as the lth order Legendre polynomial and θ being the center-of-mass scattering angle.

Out of various ways to solve the above equations, one approach is to replace this ensemble with a swarm of test particles having discrete positions and momentum consistent with the initial trap configuration and temperature, as per the Bird's proposal [78]. These test particles can represent more than one atoms in the ensemble as "macro atoms" and reduce the simulation cost of large atom clouds significantly. We used Direct Simulation Monte Carlo (DSMC) method which simulates the phase space variables, *i.e.* position and momentum, of all atoms in the ensemble for all time steps during the evolution time. The key approximation in this method is the decoupling of collision free evolution of the atomic trajectories with the trajectories incorporating inter-atomic collisions. The time evolution of an atom cloud of cold ^{87}Rb atoms has been studied as the trapping potential evolved due to the variations in amplitude of the rf-field. In this, the time steps were kept smaller than the mean collision time to ensure the validity of the decoupling approximation.

To begin with, the whole initial atom cloud is divided spatially into a large number of cells to have uniformity of the number density and trapping potential over a cell. These cells are further split in sub-cells to increase the efficiency of the collision detection algorithm and parallel processing [84]. In order to get the collision-less trajectories of the atoms, a symplectic algorithm has been used, which can conserve the total energy of the system over a time scale much longer than the total simulation time. To evaluate the phase-space variables in collision-less evolution over a time interval Δt, the following set of equations in terms of position ($\mathbf{r}$), momentum ($\mathbf{p}$) and time estimated position ($\mathbf{q}$) are used for any

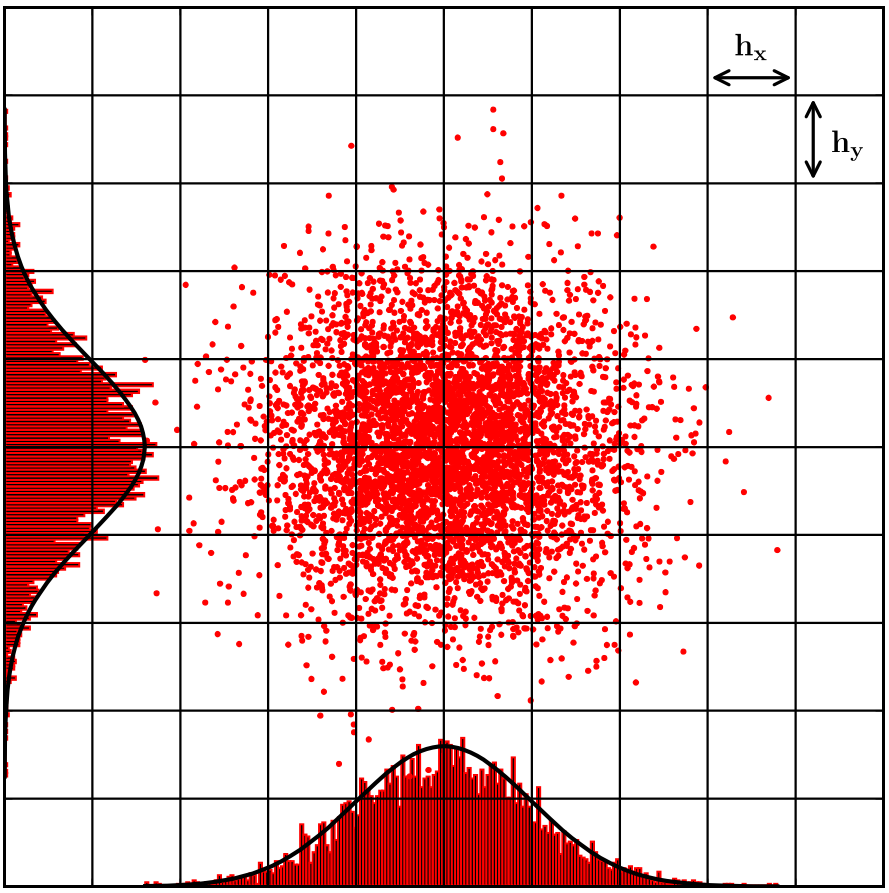

Figure 4.1: Two dimensional representation of the DSMC scheme. The dots represent the atoms with the histograms showing the number of occurrence of atoms in a specific spatial bin. Here h_x and h_y denotes the cell width and height respectively.

quadrupole magnetic trap and an rf-field having time varying amplitude and frequency. The experimental and simulation results in this study show that, as the time dependent trapping potential evolves, the shape and the number of atoms in the cloud vary. The experimental and simulation results show a qualitative agreement with respect to time evolution in the shape and number of atoms in the atom cloud.

4.1 Direct Simulation Monte Carlo Technique

The process of trapping of the atoms in the rf-dressed potential has been studied numerically with the help of a DSMC algorithm, after knowing the time dependent rf-dressed potential $V(\mathbf{r}, t)$ and LZ transition probability for the atom. An atom cloud interacting with a time varying potential $V(\mathbf{r}, t)$ can be well described by knowing the evolution of the Bosonic ensemble distribution function $f(\mathbf{p}, \mathbf{r}, t)$ which is given by the Boltzmann equation [86, 87] in terms of position ($\mathbf{r}$), momentum ($\mathbf{p}$) and time (t) as [84],

$$\left[\frac{\partial}{\partial t} + \frac{\mathbf{p}}{m}.\nabla_r - \frac{1}{m}\nabla_r V(\mathbf{r}, t).\nabla_p\right] f = I[f]. \tag{4.1}$$

The collision integral $I[f]$ can be calculated in terms of the differential scattering cross section $\frac{d\sigma}{d\Omega}$ and two distribution function f_1 and f_2 by using the equation,

$$I[f] = \frac{1}{m}\int \frac{d^3 p_2}{h^3}\int d\Omega \frac{d\sigma}{d\Omega}|\mathbf{p}_2 - \mathbf{p}_1|[f_1' f_2' - f_1 f_2], \tag{4.2}$$

where m is the mass of the atoms, $\mathbf{p}_1$ and $\mathbf{p}_2$ are the momenta of the two atoms with their respective distribution functions f_1 and f_2. The primed notation denotes distribution functions after collision. The differential cross section can be calculated as,

$$\frac{d\sigma}{d\Omega} = |f_{sc}(\theta) \pm f_{sc}(\pi - \theta)|^2, \tag{4.3}$$

Chapter 4

Evolution of atom clouds in time varying rf-dressed potentials

In this chapter, the time evolution of a cold ^{87}Rb atom cloud in a rf-dressed potential is investigated. The dynamics of the formation of the toroidal trap is studied using the Direct Simulation Monte Carlo (DSMC) technique. The DSMC technique is based on an extension of the original proposal of Bird [78]. Different variants of DSMC methods have already been used to understand the evaporative cooling [79, 80] and expansion cooling [81] in conventional trapping geometries. Both classical and quantum kinetic theory of truncated Boltzmann distribution of the phase-space provide the alternate approaches to understand the evaporative cooling mechanism [5, 6]. This applies only within the regime of validity of "sufficient ergodicity" [82, 83]. "Sufficient ergodicity" means that the phase-space density is only a function of energy. The DSMC method does not rely on this approximation and thus can simulate atomic ensembles far from their equilibrium conditions. The ergodicity assumption also fails if the mixing time of the atomic samples is longer than the elastic collision time [84]. In an earlier report the evaporative cooling in the rf-dressed traps was treated using Merkov chains [85].

The rf-dressed potential considered in this chapter is dynamically formed with a static

squares (left lobe) and triangles (right lobe). A closer inspection of the Floquet spectrum enables us to identify the source of the formation of these transition probability lobes. As stated earlier, at the position of the avoided crossings, the transition probability drops significantly, as compared to that at the positions of the real crossings. Here, the variation in ω_r leads to a periodic variation in the avoided crossing positions (as discussed in the subsection 5.3.2), which finally results in the periodic variation in the transition probabilities. Hence, the recurring lobes of the transition probability are only an outcome of the periodic spatial shifting of the avoided and real crossings as a function of the separation frequency ω_r. This specific variation of the transition probability on the mode separation frequency ω_r can be exploited to either suppress or excite transitions between different states by only tuning the ω_r to a desired frequency value.

5.4 Conclusion

In this chapter we have studied the atom field interaction using many mode Floquet theory (MMFT). Using this, the generation of rf dressed potentials with a polychromatic rf-field is investigated. The composite atom-field system has shown a number of exquisite features like periodic potential minimas and large two photon transition probabilities which can be controlled by controlling rf-field parameters. The obtained periodic potentials are easier to maneuver than their optical counterpart, and the separation between the consecutive wells can also be controlled easily. The large two photon transition probabilities can be used to characterize the cold atom cloud trapped in a static magnetic trap [90, 94].

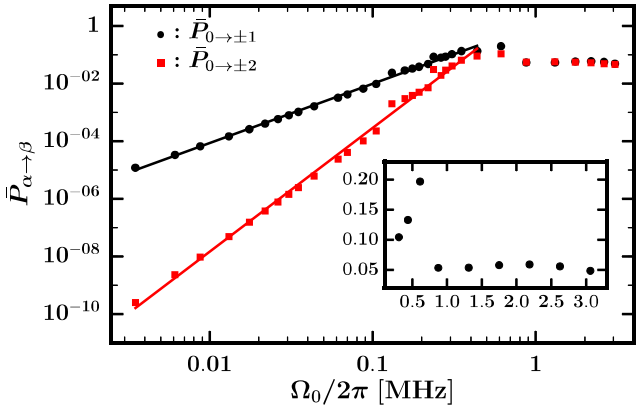

Figure 5.13: Single (black) and two (red) photon transition probability as a function of Rabi frequency $\Omega_0/2\pi$. The solid lines are linear fit to the logarithmic variation. The inset shows a sharp dip in the transition probabilities which is due to the splitting of the avoided crossings.

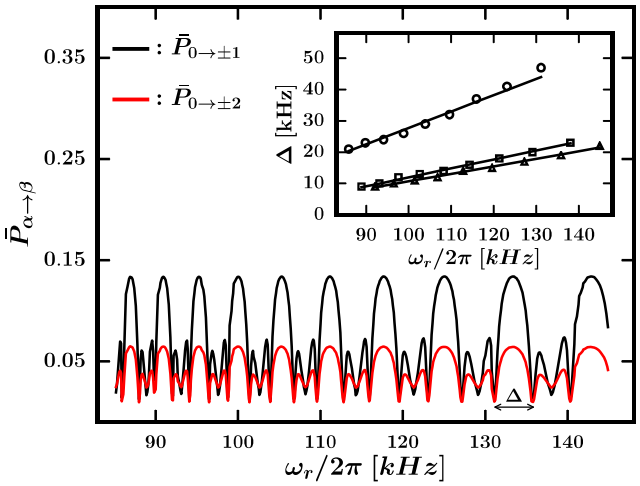

Figure 5.14: Variation of the single (black curve) and two (red curve) photon transition probabilities as a function of the separation frequency ω_r at the central resonance $\xi = 0$. The inset shows the width (Δ) of the single photon transition probability lobe as a function of the separation frequency ω_r. In the inset, circles, squares and triangles denote the width of the central, left and right lobes in the transition probability. The solid lines depict the linear fit.

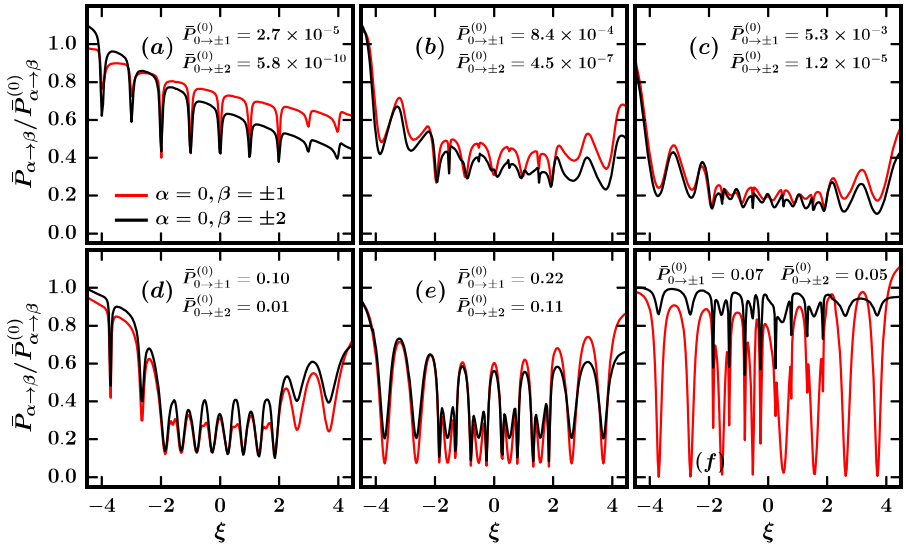

Figure 5.12: Transition probabilities $\bar{P}_{\alpha\to\beta}$ normalized by the off resonant transition probability $\bar{P}^{(0)}_{\alpha\to\beta}$ for different rf-field strengths : (a) B^x_0=10 mG, (b) B^x_0=50 mG, (c) B^x_0=0.1 G, (d) B^x_0=0.5 G, (e) B^x_0=1 G, (f) B^x_0=5 G. Here, $B^y_0 = B^z_0 = 0$, $\omega_0 = 2\pi \times$ 2 MHz, $\omega_r = 2\pi \times$ 100 kHz, $B_q = 100\ G\ cm^{-1}$, $N_o = 5$.

the studied atom-field composite system peak due to the very small separation between the energy levels, these transitions can be considered as Majorana like transitions with finite energy offset and non-zero level separation energy. The sharp decrease of the transition probabilities beyond $\Omega_0 = 2\pi \times 0.75$ MHz as shown in the inset of Fig. 5.13 is due to the splitting of the avoided crossing as shown in Fig. 5.9. This splitting of the secondary avoided crossing affects the resonance condition leading to reduction in the overall transition probability.

Further we have also studied the effect of variation in ω_r on the transition probabilities. The results of this variation are shown in Fig. 5.14. Both the transition probabilities periodically repeat a basic pattern which consists one central lobe accompanied by two smaller side lobes. The widths of these transition probability lobe (Δ) increases with the separation frequency ω_r, whereas the peak height of the lobes remain same. The width of the individual lobes are plotted in the inset of Fig. 5.14 where a linear increase in the width values is evident. The widths of the smaller lobes are not equal with each other and the difference also increases linearly as a function of ω_r, as shown by the curves with

5.3.3 Dependence of transition probabilities on rf-field parameters

A higher trap depth can not completely ensure the minimization of the trap losses as transition of atoms to other non trappable states can significantly reduce the population of trapped atom cloud. Ergo, a lower transition probability between the bare states (*i.e.* states belonging to $\{|\alpha\rangle\}$) is required for efficient trapping. On the other hand, large transition probabilities are preferable for the spectroscopic purposes to characterize the properties of the atom cloud. Hence, it is crucial to obtain the dependence of the transition probabilities on the field parameters to determine the working regimes suitable for the trapping and spectroscopic applications.

We have varied the peak coupling strength Ω_0 in a wide but experimentally feasible regime and calculated the single and two photon transition probabilities. The spatial variation of these transition probabilities are shown in Fig. 5.12 for six different values of the rf-field strength B_0^x. Apart from the expected sharp variations present near the resonance points, the absolute values ($\bar{P}_{\alpha\to\beta}$) also shows a large variation as a function of the rf-field strength. To obtain a detailed understanding of the variation of the peak transition probability with the coupling strength, the coupling strength has been varied in finer intervals as shown in Fig. 5.13. Initially, with a smaller coupling strength ($\Omega_0 = 2\pi \times 2$ kHz), the two photon transition probabilities are 5 orders of magnitude smaller than that of the single photon transition probabilities ($\approx 10^{-5}$). The avoided crossings formed at this coupling strength are of primary type as shown by the black curves in Fig. 5.8. The large separation between the energy levels results in the smaller values of transition probabilities between the atomic states in this regime. As the coupling strength is increased, both (single and two photon) transition probabilities initially grow linearly but with different rates. At $\Omega_0 = 2\pi \times 0.75$ MHz, both the transition probabilities become comparable. At this coupling strength, all the avoided crossings are completely transformed from primary to secondary type of avoided crossing with very narrow energy separation between the energy levels, as shown by the red curves in Fig. 5.8. As the transition probabilities in

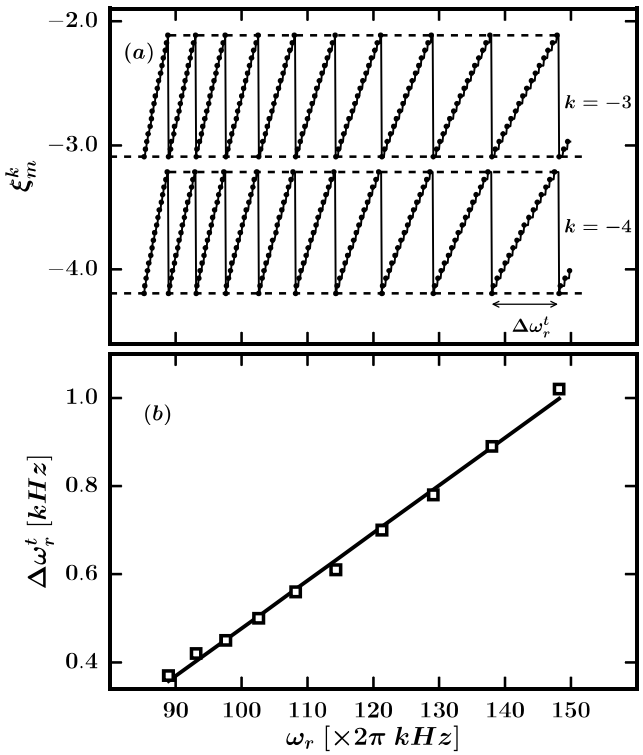

Figure 5.11: (a) Variation in position of local eigen-energy minimum ξ_m^k (ξ_m^{-3} and ξ_m^{-4}) as a function of ω_r. The dashed lines show the lower and upper ends of ξ_m^k values. (b) Variation in the separation between the terminal frequencies (ω_r^t), *i.e.* $\Delta\omega_r^t$, as a function of the separation frequency ω_r (open square). The continuous line is a linear fit. The other parameters are $\omega_0 = 2\pi \times$ 2 MHz, $B_0^x = 1$ G, $B_0^y = B_0^z = 0$ and $B_q = 100\ G\ cm^{-1}$, $N_o = 5$, $N = 4$.

The mode separation frequency ω_r in the multi-mode rf-field has been varied and the effect on the eigen-energies has been studied. It has been found that the variation in the ω_r results in a variation in the spatial profile of the eigen-energies. In Fig. 5.11 (a), the variation in the position of the third and forth eigen-energy minima (*i.e.* ξ_m^{-3} and ξ_m^{-4}) has been plotted as a function of ω_r. It can be noted that (Fig. 5.11 (a)), the position of any energy minimum shows a "saw-tooth" type oscillatory behaviour accompanied by sudden jumps at particular values of ω_r (denoted as ω_r^t). As evident from this figure, the position of an eigen-energy minimum first increases with ω_r, then jumps back to the initial lower value for a particular value of $\omega_r = \omega_r^t$, while the separation between the position of the consecutive minima (*e.g.* ξ_m^{-3} and ξ_m^{-4}) remains equal. This oscillatory feature in the position of eigen-energy minimum can be explained as follows. For a ω_r lying in between two adjacent ω_r^t values, the energy of the system should increase with an increase in the ω_r. To keep the energy-level separation unchanged with this increase in ω_r, the position of all the eigen-energy minima ξ_m^k gets shifted. At a particular value of $\omega_r = \omega_r^t$, this adiabatic shifting reaches to an extreme when the resonance condition $\omega_L = \omega_0 \pm \omega_r$ is achieved in the system, where the ξ_m^k jumps back to the initial value. It is also noted that, the separation between the adjacent ω_r^t (*i.e.* $\Delta\omega_r^t$) increases linearly which is shown in Fig. 5.11 (b). As the resonance condition $\omega_L = \omega_0 \pm \omega_r$ is position dependent, the separation $\Delta\omega_r^t$ is expected to vary as a function of ω_r.

To summarize, it is possible to improve the trap depth and alter the spatial position of the trap minima by modifying the rf-field strength and mode separation frequency respectively. Due to the dependence of the distance between the wells on the separation frequency ω_r, these lattice like traps offer more control and can be maneuvered more easily than the optical lattices.

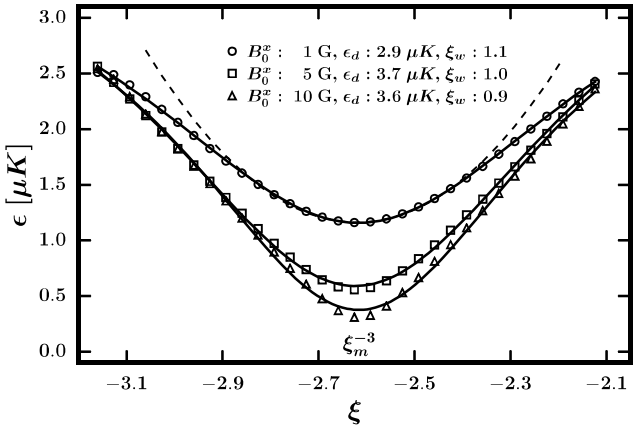

Figure 5.10: Variation in the depth of the calculated trapping potential for different field strength. The hollow markers (circle, square and triangle) shows the obtained numerical values whereas the solid curves denote the analytical fitting using Eq. (5.32). The dashed curve corresponds to a parabolic fit to the eigen-energy variation for $B_0^x = 1$ G. The other parameters are $\omega_0 = 2\pi \times 2$ MHz, $B_0^y = B_0^z = 0$, $B_q = 100\ G\ cm^{-1}$, $N_o = 5$ and $N = 4$.

the applied rf-field parameters. These results are shown in Fig. 5.10 for different values of field strengths. The spatial variation of the obtained eigen-energies were fit using the following analytical expression,

$$\epsilon(\xi) = \epsilon_\infty - \epsilon_d \left[1 + 4\left(\frac{\xi - \xi_m^k}{\xi_w}\right)^2\right]^{-1}. \tag{5.32}$$

For a particular trap potential formed at a position ξ_m^k, ϵ_∞ is the eigen-energy at $\xi \to \infty$ (arising in absence of all the other components of the polychromatic field), ϵ_d and ξ_w are the trap depth and trap width respectively. The fitted curves using this analytical equation are shown in Fig. 5.10 with continuous curves. The numerically calculated eigen-energy values are shown by the squares, circles and triangles. The fit between the numerical and the analytical results enables us to determine the parameters of interest, *i.e.* trap depth ϵ_d and trap width ξ_w, and the obtained values for the three different field strengths are marked in the figure. The numerical values have also been fit with the parabolic shape potential which is shown by the dashed curve in Fig. 5.10. This fit allows us to determine the trap frequency, for a particular potential minimum.

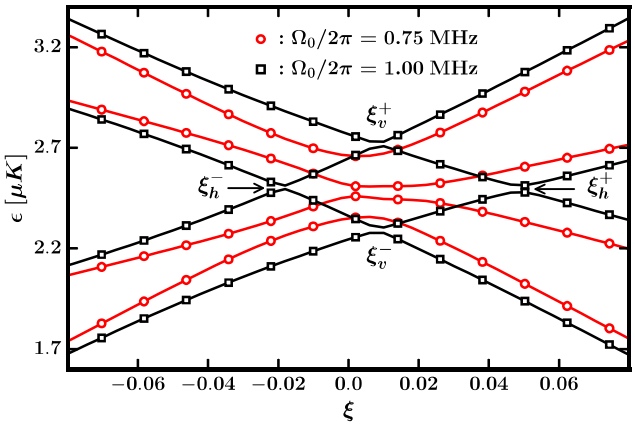

Figure 5.9: Variation in the minima positions as a function of the coupling strength $\Omega_0/2\pi$. At the crossing coupling strength Ω_0^c, the single minimum splits in to two minimas asymmetrically. The inset shows the spatial variation of the eigen-energies ϵ as a function of ξ, showing the splitting of the secondary avoided crossing formed at the 2.5 μK at $\xi = 0$. The dashed and the solid curve shows the eigen-energies at $\Omega_0 = 2\pi \times 0.75$ MHz and $\Omega_0 = 2\pi \times 1.0$ MHz respectively.

arbitrary close to one another due to the fact that the total energy is already conserved by the primary avoided crossings.

The secondary avoided crossings were studied by increasing the coupling strength further. In Fig. 5.9 the energy levels associated with a secondary avoided crossing are shown with the red curve for a coupling strength of $\Omega_0 = 2\pi\times0.75$ MHz. At a higher coupling strength $\Omega_0 = 2\pi \times 1$ MHz, the single secondary avoided crossing split into four different avoided crossings which unfurl in different directions as shown by the black curves in Fig. 5.9. The vertically formed avoided crossings at ξ_v^+ and ξ_v^- retain their spatial position while getting separated in the energy values. The horizontally formed avoided crossings shift to opposite spatial positions at ξ_h^- and ξ_h^+. This horizontal spread of these avoided crossings is asymmetric with respect to the initial crossing position at $\xi(\mathbf{r} = 0)$. This asymmetric spread of the split avoided crossings is due to the inherent asymmetry of the eigen-values of the static-field Hamiltonian H_0 in the quadrupole trap.

To characterize the traps formed by the eigen-energy minima values in Fig. 5.7, we have considered a particular minima ξ_m^{-3} and have obtained the dependence of the trap depth on

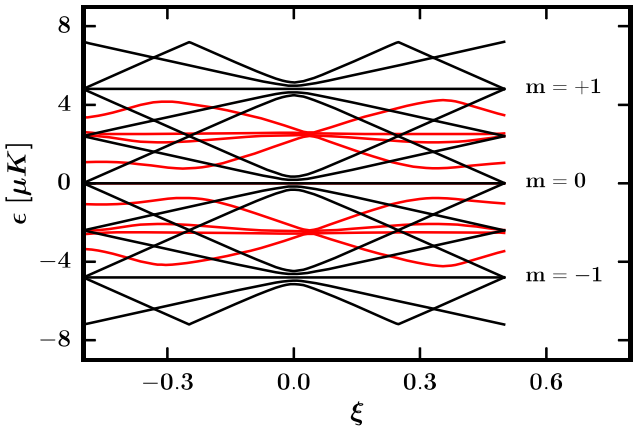

Figure 5.8: Eigen-energy levels as a function of the dimensionless scale ξ for three different sub-manifolds (*i.e.* $m = 0, \pm 1$) of the first FBZ (*i.e.* $n = 0$). The black curves corresponds to eigen-energies for $\Omega_0 = 2\pi \times 2$ kHz and the red curves corresponds for $\Omega_0 = 2\pi \times 400$ kHz.

shown by red curves) values of the coupling strength. This choice of $\xi(\mathbf{r})$, a dimensionless parameter defined as $\xi(\mathbf{r}) = (\omega_L(\mathbf{r}) - \omega_0)/\omega_r$, takes into account the spatial variation in the relevant frequency components involved in the process which makes the interpretation of the results easier. The coupling strengths are chosen to represent two separate regimes in which the formed avoided crossings are different in nature and provides the best overall visibility of the Floquet eigen-spectrum.

In case of a very small coupling strength (*e.g.* $\Omega_0 \approx 2\pi \times$ 2 kHz), the avoided crossings formed at the center (*i.e.* $\xi(\mathbf{r}) = 0$) belong to a particular sub-manifold with a single m value as shown by the black curves in Fig. 5.8. The separation between the energy levels in these avoided crossings depend on the coupling strengths as a consequence of the conservation of energy. Hence, at the intermediate coupling strengths, an increase in Ω_0 increases the eigen-energy values monotonically. However, at a larger coupling strength (*e.g.* $\Omega_0 \approx 2\pi \times$ 400 kHz) a situation can arise where the energy levels from adjacent sub-manifolds (with different m values) can come close to each other to form a different kind of avoided crossing known as the 'secondary avoided crossing'. The secondary avoided crossings formed by levels with different m values are shown by the red lines in the Fig. 5.8. The energy levels in the secondary avoided crossing can be

process which makes the interpretation of the results easier. This plot shows a plethora of avoided crossings in the spatial variation of the eigen-energies. As expected, the number of avoided crossings across the zero energy is proportional to the number of side frequency modes in the rf-field, which is 8 (for $k = \pm 1 \rightarrow \pm 4$). Therefore, the field mode index k can be used to mark the position of the local eigen-energy minimum as ξ_m^k. Out of these 8 minima (Fig. 5.7 (a)), there are four minima at the edge of the spectrum (marked as $\xi_m^{\pm 3}$ and $\xi_m^{\pm 4}$) and four minima in the central region of the spectrum. The central region minima are split into eight structures. This additional splitting of the eigen-energy minima in the central region is due to the additional avoided crossings which are generated across the lower (solid red) and upper (solid black) eigen-energy curves. Due to the comparatively large separations between the avoided crossings, the transition probability P_{LZ} for these wells is almost zero for an atom cloud of temperature $\sim\ 10\mu K$. The low value of P_{LZ}, which is one of the key requirements for atom trapping, makes these potentials more desirable. Hence, this multi-well energy structure shown in Fig. 5.7 (a) can be utilized as a lattice potential for atom trapping, similar to the one obtained using interfering counter propagating laser beams (*i.e.* optical lattices). Characterization of the individual wells with different field parameters for trapping purposes is presented later in the next subsection.

5.3.2 Dependence of eigen-energies on field parameters

The eigen energies obtained from the Floquet spectrum can be manipulated using different rf-field parameters like field strength and mode separation. As the obtained eigen-energies can be utilized to trap atoms in the adiabatic potentials, these dependences can be exploited to tailor trapping geometries for specific applications.

In Fig. 5.8, the variation of eigen-energies in the first FBZ for three sub-manifolds ($m = 0, \pm 1$) has been plotted as a function of $\xi(\mathbf{r})$ to show the formation of the avoided crossings at very low (*i.e.* $\Omega_0 = 2\pi\times$ 2 kHz shown by black curves) and high (*i.e.* $\Omega_0 = 2\pi\times$ 400 kHz

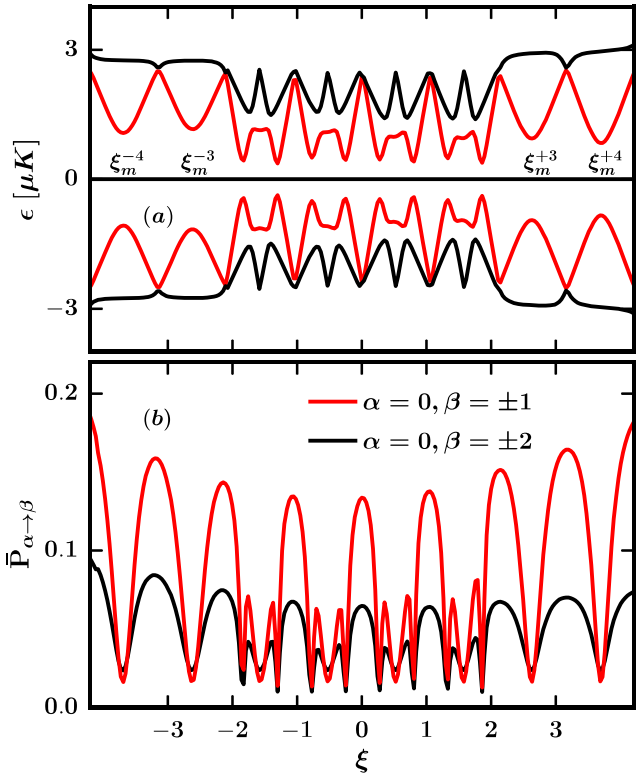

Figure 5.7: (a) Variation in eigen-energies (ϵ) as a function of dimensionless parameter $\xi = (\omega_L - \omega_0)/\omega_r$ for $N = 4$. Here, ξ_m^k correspond the eigen-energy minimum for the kth component of the rf-field. (b) Time averaged transition probabilities $\left(\bar{P}_{\alpha\to\beta}\right)$ between the $|0\rangle$ and $|\pm 1\rangle, |\pm 2\rangle$ states as a function of ξ. The other parameters are $\omega_0 = 2\pi \times$ 2 MHz, $\omega_r = 2\pi \times$ 100 kHz and $B_0^x = 1$ G, $B_0^y = B_0^z = 0$, $B_q = 100\ G\ cm^{-1}$, $N_o = 5$.

The eigen-energies inside the FBZ are uniquely defined and cannot cross each other as a result of the Von-Neumann-Wigner non-crossing rule. According to this rule, the crossing of eigen-energies are forbidden while only one single parameter is varied in the whole parameter space in which the Hamiltonian is spanned. Therefore, a spatial variation in the energy will essentially result in an avoided crossing at all the points where any of the field modes becomes resonant with the spatially varying Larmor precision frequency $\omega_L(\mathbf{r})$.

The central region of the FBZ has been plotted in Fig. 5.7 (a) as a function of the dimensionless parameter $\xi = (\omega_L(\mathbf{r}) - \omega_0)/\omega_r$. The choice of this spatial parameter takes into consideration of all the relevant frequency components involved in the interaction

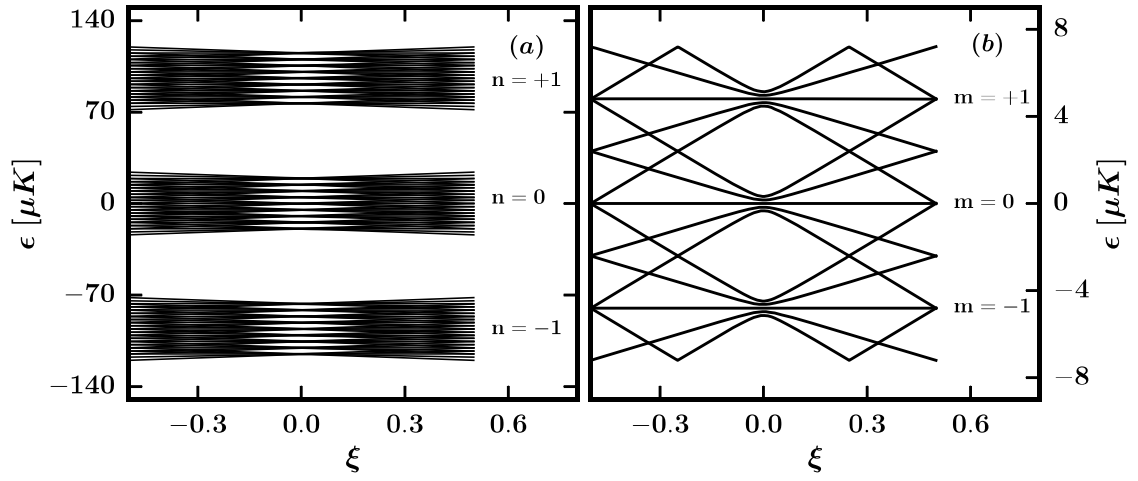

Figure 5.6: Spatial variation of the quasi-energies as a function of the dimensionless scale ξ are plotted for the Floquet manifolds $n = 0, \pm 1$ (a); and the sub-manifolds $m = 0, \pm 1$ for n=0 (b).

where n and m are integers representing different orders of extension of the Fourier basis states for ω_0 and ω_r respectively, denoting the energy band indices. Here, $\epsilon_{\alpha 00}$ represents the eigen-energy of the central Floquet spectrum for the indices $n = 0$ and $m = 0$.

As the index n belongs to the set of integers, the eigen-energy values $\epsilon_{\alpha nm}$ increase indefinitely with n, while preserving the fundamental energy structure associated with $\epsilon_{\alpha 0m}$. Therefore, similar to the Bloch theory, we utilize this repetition of energy structure to identify the Floquet-Brillouin zone (FBZ) as the fundamental manifold of eigen-energies corresponding to $n = 0$. Hence, our discussion of the results are limited upto the boundary of the first FBZ defined by the eigen-energy $\epsilon_{\alpha nm}$ lying in the energy interval $[-\hbar\omega_0/2, \hbar\omega_0/2]$. The index m relates to the polychromaticity of the radiation field and thus restricted to values from $-N$ to N,which is corresponding to total number of modes present in the spectrum. Hence, inside the FBZ, a total of $(2N + 1)$ individual eigen-energy sub-manifolds will emerge corresponding to different m values. The different eigen-energy manifolds generated by different number of n values are shown in Fig. 5.6 (a) and the sub-manifolds for different m values for the central manifold $n = 0$ is shown in Fig. 5.6 (b).

next sections using the MMFT approach with the optimum truncation order $N_o = 5$, which is sufficient to achieve acceptable accuracy.

5.3 Results of MMFT on interaction of atoms with the polychromatic rf-field

In this section, the interaction of an atom with a polychromatic rf-field having more than two component has been studied numerically. In the numerical calculations, using the Floquet formalism described in section 5.1, we tune the coupling strength of the central mode Ω_0 and the separation frequency between consecutive modes ω_r to access different regimes of the interaction. The atomic system considered is comprising of ^{87}Rb atoms trapped in a quadrupole magnetic trap with a radial field gradient $B_q = 100\ G\ cm^{-1}$ in the hyperfine state $|F = 2\rangle$. The polychromatic rf-field used in this study contains 8 side modes and one central mode at frequency $\omega_0 = 2\pi \times 2$ MHz. The values of the parameters such as ω_0, ω_r, B_q and Ω_0 are chosen such that experiments can be performed conveniently.

5.3.1 Analysis of the Floquet spectrum

In order to gain an insight into the various physical processes, the eigen-energy spectrum (or “Floquet spectrum") is obtained by diagonalizing the Floquet Hamiltonian $\mathbb{H}^F_{\omega_k}$. The eigen-energies in Floquet theory are called ‘quasi-energies’, akin to the ‘quasi-momentum’ for the momentum of electrons in the Bloch theory of lattices. In the Floquet formalism, the eigen-energies can be written as,

$$\epsilon_{\alpha nm} = \epsilon_{\alpha 00} + n\hbar\omega_0 + m\hbar\omega_r, \tag{5.31}$$

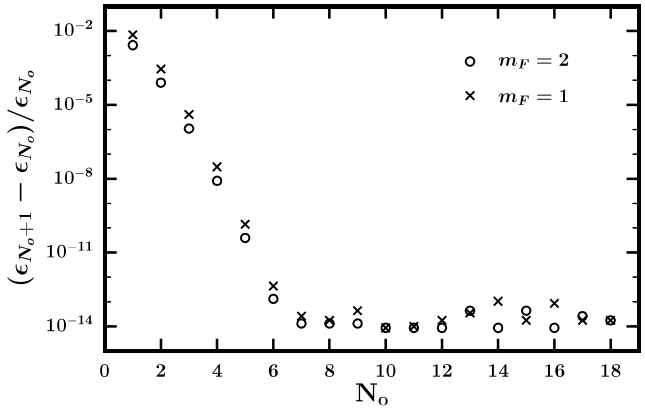

Figure 5.5: Calculated convergence of relative error (*i.e.* $(\epsilon_{N_0+1} - \epsilon_{N_0})/\epsilon_{N_0}$) of the infinite matrix $\mathbb{H}^F_{\omega_0}$ as a function of the truncation order at off-resonant detuning $\delta_0\,(r = 40\,\mu m)$. The other parameters are $\omega_0 = 2\pi \times 2$ MHz, $B^x_0 = 1$ G, $B^y_0 = B^z_0 = 0$, $B_q = 100\,G\,cm^{-1}$.

the resonant ($\delta_0(r = 0\ \mu m)$) and off-resonant ($\delta_0(r = 40\ \mu m)$) values of detuning when $N_o < 3$. After reaching $N_o = 3$, the $\Delta\epsilon_0$ stabilizes to a particular value depending on the Zeeman hyperfine state and detuning. This suggests a minimum value of N_o, *i.e.* $N_o > 3$, is sufficient to minimize the truncation error in the MMFT approach and the effect of truncation is higher for the off resonant detuning than the resonant ones.

The effect of truncation can not be completely established by comparing the values with the RWDS approach only, which itself is a crude approximation. In order to obtain a detailed understanding of the effect of truncation of the infinite matrices, convergence of relative error as a function of the truncation order is calculated and these results are shown in Fig. 5.5 for two states $|m_F = 1, 2\rangle$ for an off-resonant detuning at $\delta_0\,(r = 40\,\mu m)$. The minimum truncation order ($N_o = 3$) obtained from the comparison with the RWDS approach yields a relative error of $\sim 10^{-6}$ whereas the applied truncation order $N_o = 5$ yields a relative error of $\sim 10^{-11}$. Hence, in comparison with the absolute values of $\epsilon(\mathbf{r})$ ($\sim 20\,\mu K$ and $\sim 40\,\mu K$ for $m_F = 1, 2$ respectively), the error introduced due to truncation is vanishingly small for the applied truncation order $N_o = 5$. For $N_o > 7$, though the relative truncation error is $\sim 10^{-14}$, the computation time also increases considerably. Therefore, interaction of an atom with a polychromatic rf-field has been studied in the

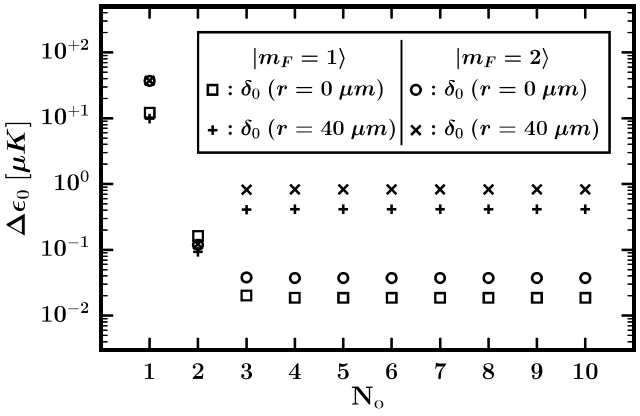

Figure 5.4: Calculated energy difference ($\Delta\epsilon_0$) between the RWDS and MMFT methods as a function of truncation order N_o in the infinite matrix $\mathbb{H}^F_{\omega_0}$ for two different values of detuning values $\delta_0\,(r = 0\,\mu m)$ and $\delta_0\,(r = 40\,\mu m)$. The saturation of energy difference above $N_o = 3$ provides the minimum order of truncation to be used is $N_o > 3$. The other parameters are $\omega_0 = 2\pi \times 2$ MHz, $B_0^x = 1$ G, $B_0^y = B_0^z = 0$, $B_q = 100\ G\ cm^{-1}$.

RWA, provides nearly accurate eigen-energies, while being used with appropriate truncation order.

5.2.3 Effect of truncation of the infinite matrices in MMFT

Despite the success of the MMFT approach in the above subsection to provide better results than the earlier established approaches, use of MMFT approach can only be validated when the error in the energy eigen values due to the truncation of the infinite Hamiltonian matrices is established appropriately. This implies that the error due to the truncation should be smaller than all the other relevant energy scales.

A close agreement between the eigen-energies obtained from the RWDS and the MMFT approach, as discussed in the previous subsection can be exploited to find out the minimum value of truncation order (N_o) for which the difference of the eigen-energies (*i.e.* $\Delta\epsilon_0$) from both the approaches is minimum. The difference between the eigen-energies ($\Delta\epsilon_0$) are plotted as a function of the truncation order N_o in Fig. 5.4 for two different detuning values $\delta_0\,(r = 0\,\mu m)$ and $\delta_0\,(r = 40\,\mu m)$. The results show a large $\Delta\epsilon_0$ for both

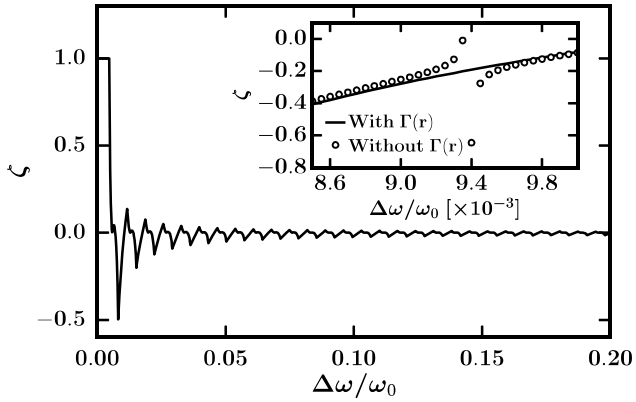

Figure 5.3: Dimensionless quality parameter ζ for equally strong rf-fields (*i.e.* $|\Omega_0|^2 = |\Omega_1|^2$) as a function of relative frequency separation $\Delta\omega/\omega_0$ in the LRM approach. The inset shows the magnified plot of a particular region with (continuous curve) and without (hollow circles) considering the stark shifts $\Gamma(\mathbf{r})$ due to the off-resonant rf-fields. Here $\omega_0 = 2\pi \times 2$ MHz, $B_0^x = 1$ G, $B_0^y = B_0^z = 0$ and $B_1^x = 1$ G, $B_1^y = B_1^z = 0$, $B_q = 100\ Gcm^{-1}$.

one eigen-energy to another at the resonance crossing points (r_c) becomes smooth while the depth of the potential minimum at the resonance points ($\delta_0 = \delta_1 = 0$) becomes equal [91]. This leads ζ to be nearly zero at the large $\Delta\omega/\omega_0$. On the contrary, at the smaller frequency separations, both the shift in the eigen-energy minima and the energy-shift at the resonance crossing points become finite. This leads to a large increase in the ζ value which questions the validity of the LRM approach at the limit $\Delta\omega/\omega_0 \to 0$.

The effect of inclusion of the stark-shifts due to the non-resonant rf-fields in the LRM approach is shown in the inset of Fig. 5.3. The smooth solid line shows the value of ζ while keeping the contribution of the stark-shifts, whereas the hollow circles shows the values without considering the stark-shifts. It is clear from this plot that the inclusion of stark-shift eliminates the sudden divergences and provided a smooth variation of ζ.

The outcome of this subsection establishes that even for only two rf-fields, with relative strength more than 0.1 and relative frequency separation less than 0.05, both the earlier approaches RWDS and LRM break down. Therefore, it is natural to look for a different formalism, such as MMFT, to cover all the regimes of the parameters where the earlier approaches are inadequate. The MMFT approach, being neither perturbative nor based on

$$\Gamma_0(\mathbf{r}) = \frac{\Omega_0^2}{\delta_1(\mathbf{r})}, \tag{5.27a}$$

$$\Gamma_1(\mathbf{r}) = \frac{\Omega_1^2}{\delta_0(\mathbf{r})}, \tag{5.27b}$$

where δ_0 and δ_1 are the frequency detunings of the two frequency components (ω_0 and ω_1) with Larmor frequency $\omega_L(\mathbf{r})$. After considering these stark shifts, the eigen-energies corresponding to the two frequency components become,

$$\epsilon_0(\mathbf{r}) = \sqrt{(\delta_0(\mathbf{r}) + 2\Gamma_0(\mathbf{r}))^2 + |\Omega_0|^2}, \tag{5.28a}$$

$$\epsilon_1(\mathbf{r}) = \sqrt{(\delta_1(\mathbf{r}) + 2\Gamma_1(\mathbf{r}))^2 + |\Omega_1|^2}. \tag{5.28b}$$

In the LRM approach, the final eigen-energy of the two component atom-field composite system with two component rf-field can be obtained as,

$$\epsilon_{0,1}(\mathbf{r}) = m_F\hbar\Big[\Theta\Big[\Delta\delta(\mathbf{r})\Big]\epsilon_0(\mathbf{r}) + \Theta\Big[-\Delta\delta(\mathbf{r})\Big]\epsilon_1(\mathbf{r})\Big] \tag{5.29}$$

where $\Delta\delta(\mathbf{r}) = |\delta_1(\mathbf{r})| - |\delta_0(\mathbf{r})|$, determines the proximity of resonance due to one component over the other component. The Heaviside step function $\Theta[x]$ facilitates the transition of the final eigen-energy $\epsilon_{0,1}(\mathbf{r})$ from one eigen-energy to another at the resonance crossing points r_c, defined by $\Delta\delta(r_c) = 0$ (*i.e.* $\delta_0(r_c) = \delta_1(r_c)$). The key approximation in this method is the separation between the two frequencies (*i.e.* $\Delta\omega = \omega_1 - \omega_0$) being sufficient so that the jump in energy at r_c is minimum. Hence, to obtain the validity regime of the LRM approach, the dimensionless parameter ζ can be defined as,

$$\zeta = \lim_{r \to r_c} \frac{\epsilon_0(\delta_0 = 0) - \epsilon_1(\delta_1 = 0)}{\epsilon_0(r) - \epsilon_1(r)}. \tag{5.30}$$

Figure 5.3 shows the plot of the dimensionless parameter ζ as a function of the relative frequency separation $\Delta\omega/\omega_0$. At large values of frequency separation, the transition from

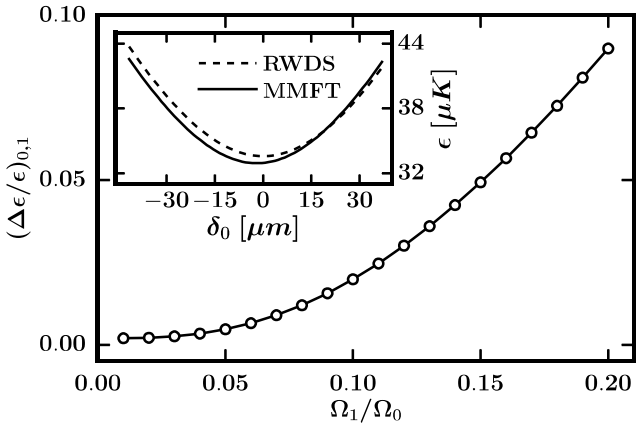

Figure 5.2: Relative shift in energy $(\Delta\epsilon/\epsilon)_{0,1}$ as a function of the relative strength (Ω_1/Ω_0). In the inset, eigen-energies $(\epsilon_{0,1})$ obtained from the RWDS (dashed curve) and the MMFT (solid curve) for relative strength $\Omega_1/\Omega_0 = 0.1$ are shown as a function of detuning δ_0. The other parameters are $\omega_0 = 2\pi \times 2$ MHz, $\omega_1 = 2\pi \times 2.2$ MHz, $B_0^x = 1$ G, $B_0^y = B_0^z = 0$, $B_q = 100\, G\, cm^{-1}$, $N_o = 5$.

where $\epsilon_{0,1}^{MMFT}$ is the eigen-energy obtained from MMFT for two component rf-field. The monotonic increase in the energy shift shows the limitation of the perturbative approach. For example, with $\Omega_1 \simeq 20\%$ of Ω_0, the difference in the eigen-energy is considerably large (9%). The eigen-energies obtained by two methods (MMFT and RWDS) have also been plotted as a function of detuning in the inset of Fig. 5.2 to bring out the difference clearly.

Since the perturbative approach shows very large shifts in the eigen-energies even for small relative coupling strengths, the interaction of an atom with two rf-fields with comparable strength $(\Omega_1 \simeq \Omega_0)$ can not be treated with this approach. In a work by Courteille et. al. [91], this atom-field interaction with two mode of rf-field, has been treated with a local resonance method (LRM) in which the atom is considered interacting with only a single frequency component of the rf-field (having lowest detuning) at any particular trap position ($\mathbf{r}$). The effect of the off-resonant components of the rf-field are incorporated by evaluating the ac stark-shifts $\Gamma(\mathbf{r})$ and modifying the dressed state eigen-energies as discussed below. To obtain the eigen-energies of this system, the stark shifts for the off-resonant rf-fields as a function of detuning (*i.e.* position) is obtained by using the relation,

system interacting with a single frequency rf-field. To correlate the frequency detuning with the spatial scale, Eq. (5.24) has been used along with Eq. (2.5) with the radial field gradient $B_q = 100\ G\ cm^{-1}$.

The energy difference $\Delta\epsilon_0 = \epsilon_0^{RWDS} - \epsilon_0^{MMFT}$ is shown in Fig. 5.1 (b) as a function of detuning. A perfect agreement between energy values from two approaches at zero detuning proves the excellent validity of both the approaches at the resonance point. The minuscule difference between the two approaches around the resonance may be due to the removal of the counter rotating term from the Hamiltonian under the RWDS approach.

5.2.2 Comparison of MMFT with earlier methods for two mode rf-field

To make a further comparison, the case of an rf-field having two frequency components has been considered. The second component of the rf-field, *i.e.* $\mathbf{B}_1(t)$, has frequency ω_1 and coupling strength $|\Omega_1|$, with other parameters (like polarization) considered same as $\mathbf{B}_0(t)$. In RWDS approach, the ratio of the coupling strengths of the two modes is assumed to be 'relatively small' ($\Omega_1/\Omega_0 \to 0$). Hence the interaction of the second component of the rf-field $\mathbf{B}_1(t)$ can be treated perturbatively, where the eigen-energy values are considered same as ϵ_0. To compare the results of this approach with the results of MMFT, the eigen-energies obtained by MMFT (using $\mathbb{H}^F_{\omega_k}$ for $k = 1$) are compared. An appropriate amplitude envelope $G(\omega)$ was used, which has a variable strength of the positive component $\omega_{k=+1}$ while having a zero strength of the negative component $\omega_{k=-1}$.

Figure 5.2 shows the dependence of the relative energy difference between the eigen-energies obtained from both the RWDS and MMFT method as a function of the relative coupling strength Ω_1/Ω_0, where the relative energy difference has been described as,

$$\left(\frac{\Delta\epsilon}{\epsilon}\right)_{0,1} = \left(\epsilon_0^{RWDS} - \epsilon_{0,1}^{MMFT}\right)/\epsilon_{0,1}^{MMFT}, \tag{5.26}$$

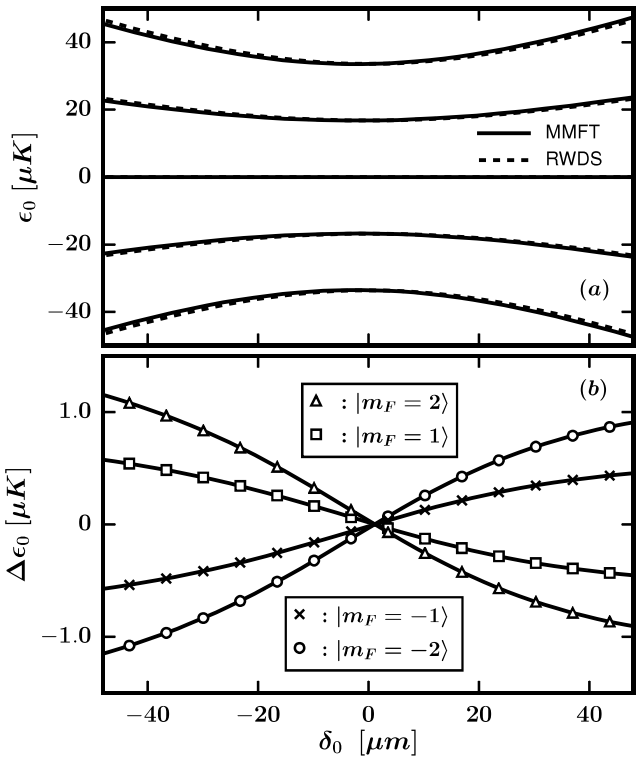

Figure 5.1: Comparison of the MMFT and RWDS method for an atom interacting with a single frequency rf-field. (a) Variation of eigen-energies (ϵ_0) for different Zeeman hyperfine sub-levels as a function of δ_0, using the RWDS and MMFT (for truncation order $N_o = 5$). (b) Difference ($\Delta\epsilon_0$) between the energy values predicted by MMFT and RWDS approaches as a function of δ_0. The other parameters used are $\omega_0 = 2\pi \times 2$ MHz, $B_0^x = 1$ G, $B_0^y = B_0^z = 0$, $B_q = 100\ G\ cm^{-1}$.

Hamiltonian becomes,

$$H = \frac{g_F \mu_B}{\hbar}\left[F_3\left(|\mathbf{B}_s(\mathbf{r})| + B_0^{\parallel}\right) + \sum_{i=1,2} F_i B_0^{\perp i}\right]. \tag{5.22}$$

Here $B_0^{\perp 1}$, $B_0^{\perp 2}$ and $B_0^{\parallel}$ are amplitudes of the perpendicular and parallel components of the applied rf-field $\mathbf{B}_0(t)$ with respect to the local static field vector $\mathbf{B}_s(\mathbf{r})$. F_i $(i = 1, 2)$ are the hyperfine operators along the $B_0^{\perp 1}$ and $B_0^{\perp 2}$ components and F_3 is the component of the hyperfine operator along $B_0^{\parallel}$ [77]. Due to the vectorial nature of coupling between the atomic hyperfine sub-levels and the applied rf-field, only the perpendicular components contribute to the final coupling strength Ω_0, and the contribution from the parallel component can be neglected using the adiabatic approximation. Using this Hamiltonian in Eq. (5.22), the eigen-energies for different Zeeman hyperfine sub-levels ($m_F = -F$ to F) in vicinity of the quadrupole trap center can be obtained using RWDS approach in terms of the detuning δ_0 and the coupling strength or Rabi frequency Ω_0 as,

$$\epsilon_0(\mathbf{r}) = m_F \hbar \sqrt{\delta_0^2 + |\Omega_0|^2}, \tag{5.23}$$

with

$$\delta_0(\mathbf{r}) = \omega_L(\mathbf{r}) - \omega_0, \tag{5.24}$$

$$|\Omega_0|^2 = \left(\frac{g_F \mu_B}{2\hbar}\right)^2 \left[2 B_0^{\perp 1} B_0^{\perp 2} \sin\gamma + \sum_{i=1,2} (B_0^{\perp i})^2\right], \tag{5.25}$$

where $\omega_L(\mathbf{r})$ is the Larmor frequency from Eq. (2.5), γ is the phase separation between the perpendicular components $B_0^{\perp 1}$ and $B_0^{\perp 2}$ [77].

Figure 5.1 (a) shows the eigen-energies $\epsilon_0(\mathbf{r})$ seen by ^{87}Rb atoms for different Zeeman hyperfine sub-levels of the $|F = 2\rangle$ state under RWDS and MMFT approaches, as function of detuning δ_0. Close agreement between the results from both the approaches ensures the validity of the many mode Floquet theory to predict the eigen-energies of an atomic

obtained by MMFT approach has been compared with those obtained by using the rotating wave dressed state (RWDS) approach for a single mode rf-field [77]. For a two mode rf-field, the eigen-energies obtained using MMFT approach have been compared with those obtained from RWDS and local resonance model (LRM) approach [91]. For a practical atom-field interaction problem, the infinite dimensional Floquet matrices $\mathbb{H}^F_{\omega_k}$, $\mathbb{H}^F_{\omega_0}$ and $\mathbb{Q}_k$ needs to be truncated after appropriate order. The effect of truncation of these matrices have been scrutinized to determine the resulting errors in the eigen-energies.

5.2.1 Comparison of MMFT with other techniques for single mode rf-field

To begin with, the interaction of the atoms with single frequency rf-field has been considered in presence of a static magnetic field using an approach based on the rotating wave approximation in dressed state picture (RWDS) and the results are compared with the MMFT formalism. In RWDS approach, the counter rotating terms are removed from the Hamiltonian for analytical simplicity.

We consider an atom trapped in a static quadrupole field $\mathbf{B}_s(\mathbf{r})$ given by the Eq. (2.4) and exposed to a monochromatic rf-field with frequency ω_0 and of form

$$\mathbf{B}_0(t) = \begin{pmatrix} B_0^x cos(\omega_0 t) \\ B_0^y cos(\omega_0 t - \phi_y) \\ B_0^z cos(\omega_0 t - \phi_z) \end{pmatrix}, \tag{5.21}$$

where B_0^x, B_0^y and B_0^z are the rf-field strengths along the Cartesian axes and ϕ_y, ϕ_z are the phase differences between the x-y and x-z component respectively. To remove the time dependence, we transform the composite atom-field system Hamiltonian by applying an unitary transformation and under the rotating wave approximation the transformed

ities are calculated using first and second order perturbation theory [107]. In contrast, the transition probability obtained from MMFT in Eq. (5.19) can be utilized to determine single and multi-photon transition probabilities without a prior specification of the total number of photons involved in the transition process. The obtained transition probability $\bar{P}_{\alpha\to\beta}$ is equivalent to the one obtained using an infinite order perturbation theory [108, 95].

Though, these time-averaged transition probabilities are useful for the determination of the 'avoided crossings' and probability of the trapping of the atom, we note that any avoided crossing is usually characterized by a different non-adiabatic transition probability, called Landau-Zener transition probability P_{LZ} [109, 110]. This transition probability was originally proposed by Landau and Zener for two level systems and later modified by Vitanov et al [111] for a multi-level system. At any avoided crossing, P_{LZ} can be determined in terms of the energy gap at the crossing $\delta\epsilon$, spread of the avoided crossing in frequency space $\delta\omega$, and rate of change of the frequency with time $\dot{\omega}$ which is dependent on velocity of the atom with which it traverses the avoided crossing. The LZ transition probability is given as,

$$P_{LZ} = 1 - \exp\left(-\frac{\pi}{2}\frac{\delta\epsilon\delta\omega}{\dot{\omega}}\right). \tag{5.20}$$

Due to the induction of avoided crossing in all the resonant interactions between the atom and radiation field, the transition probability P_{LZ} determines the validity of the adiabaticity condition in the system.

5.2 Establishment of validity of MMFT approach

In order to conduct a thorough numerical study, objective of which was to provide physical parameters of experimental interest, we consider the case of ^{87}Rb atom in the hyperfine state $|F = 2\rangle$, which is interacting with an rf-field in presence of a static magnetic field of a quadrupole trap. To establish the validity of the MMFT approach, the eigen-energies

truncated Floquet matrices of Eqs. (5.12) and (5.13) are constructed for each spatial grid point (1D space grid) and the corresponding eigen-energies are evaluated using the Eq. (5.9). The obtained eigen-energy values for different spatial grid points provide the spatial dependence of the eigen-energy spectrum corresponding to different eigen-states.

The time evolution of the composite atom-field system of Eq. (2.1) in the Floquet formalism can be described by the matrix form of the time evolution operator $U_{\beta\alpha}(t, t_0)$ in terms of the Floquet Hamiltonian as,

$$U_{\beta\alpha}(t, t_0) = \sum_n \sum_m \langle \beta nm | \exp[-iH^F(t - t_0)] | \alpha 00 \rangle \times \exp[i(n\omega_0 + m\omega_r)t]. \tag{5.16}$$

The transition probability between unperturbed atomic states can be calculated using the time evolution operator of Eq. (5.16) by,

$$P_{\alpha\to\beta}(t, t_0) = |U_{\beta\alpha}(t, t_0)|^2. \tag{5.17}$$

An average over the initial time t_0, with a fixed elapsed time $(t - t_0)$, leads to the transition probability,

$$\begin{aligned} P_{\alpha\to\beta}(t - t_0) &= \sum_{nm} |\langle \beta nm | \exp[-iH^F(t - t_0)] | \alpha 00 \rangle|^2 \\ &= \sum_{nm} \sum_{k_1,k_2} \sum_{\epsilon n' m'} |\langle \beta k_1 k_2 | \epsilon n' m' \rangle|^2 \langle \alpha nm | \epsilon n' m' \rangle \langle \epsilon n' m' | \alpha 00 \rangle \exp[i(n\omega_0 + m\omega_r)t_0]. \end{aligned} \tag{5.18}$$

A further average over the elapsed time $(t - t_0)$ provides the time-averaged transition probabilities between two atomic states $|\alpha\rangle$ and $|\beta\rangle$ in terms of only the eigen-states of the Floquet Hamiltonian H^F as [97],

$$\bar{P}_{\alpha\to\beta} = \sum_{n,m} \sum_{\epsilon n' m'} |\langle \beta nm | \epsilon n' m' \rangle \langle \epsilon n' m' | \alpha 00 \rangle|^2. \tag{5.19}$$

In standard perturbation theory approach, the single and two photon transition probabil-

$$\mathbb{H}^F_{\omega_0} = \begin{bmatrix} \ddots & \vdots & & & & \vdots & \\ \cdots & \mathbb{H}_0 + 2\hbar\omega_0\mathbb{I} & \mathbb{Y}_0 & \mathbb{O} & \mathbb{O} & \mathbb{O} & \cdots \\ & \mathbb{Y}_0 & \mathbb{H}_0 + \hbar\omega_0\mathbb{I} & \mathbb{Y}_0 & \mathbb{O} & \mathbb{O} & \\ & \mathbb{O} & \mathbb{Y}_0 & \mathbb{H}_0 & \mathbb{Y}_0 & \mathbb{O} & \\ & \mathbb{O} & \mathbb{O} & \mathbb{Y}_0 & \mathbb{H}_0 - \hbar\omega_0\mathbb{I} & \mathbb{Y}_0 & \\ \cdots & \mathbb{O} & \mathbb{O} & \mathbb{O} & \mathbb{Y}_0 & \mathbb{H}_0 - 2\hbar\omega_0\mathbb{I} & \cdots \\ & \vdots & & & & \vdots & \ddots \end{bmatrix}; \tag{5.13}$$

$$\mathbb{Q}_k = \begin{bmatrix} \ddots & \vdots & & & & \vdots & \\ \cdots & \mathbb{O} & \mathbb{Y}_k & \mathbb{O} & \mathbb{O} & \mathbb{O} & \cdots \\ & \mathbb{Y}_{-k} & \mathbb{O} & \mathbb{Y}_k & \mathbb{O} & \mathbb{O} & \\ & \mathbb{O} & \mathbb{Y}_{-k} & \mathbb{O} & \mathbb{Y}_k & \mathbb{O} & \\ & \mathbb{O} & \mathbb{O} & \mathbb{Y}_{-k} & \mathbb{O} & \mathbb{Y}_k & \\ \cdots & \mathbb{O} & \mathbb{O} & \mathbb{O} & \mathbb{Y}_{-k} & \mathbb{O} & \cdots \\ & \vdots & & & & \vdots & \ddots \end{bmatrix}; \; \mathbb{Y}_k = \begin{pmatrix} 0 & \Omega^{(k)}_{\alpha\beta} & \Omega^{(k)}_{\alpha\gamma} & \cdots \\ \Omega^{(k)}_{\beta\alpha} & 0 & \Omega^{(k)}_{\beta\gamma} & \\ \Omega^{(k)}_{\gamma\alpha} & \Omega^{(k)}_{\beta\gamma} & 0 & \\ \vdots & & & \ddots \end{pmatrix}; \tag{5.14}$$

$$\mathbb{O} = \begin{pmatrix} 0 & 0 & 0 & \cdots \\ 0 & 0 & 0 & \\ 0 & 0 & 0 & \\ \vdots & & & \ddots \end{pmatrix}; \; \mathbb{H}_0 = \begin{pmatrix} \varepsilon_\alpha & 0 & 0 & \cdots \\ 0 & \varepsilon_\beta & 0 & \\ 0 & 0 & \varepsilon_\gamma & \\ \vdots & & & \ddots \end{pmatrix}; \; \mathbb{I} = \begin{pmatrix} 1 & 0 & 0 & \cdots \\ 0 & 1 & 0 & \\ 0 & 0 & 1 & \\ \vdots & & & \ddots \end{pmatrix}. \tag{5.15}$$

The eigen-energies of the matrix $\mathbb{H}^F_{\omega_k}$ are called 'quasi-energies' as they contain contributions from all the Floquet modes n and m. As the eigen-value problem of Eq. (5.9) cannot be solved numerically with the infinite dimensional Floquet matrices $\mathbb{H}^F_{\omega_k}$ and $\mathbb{H}^F_{\omega_0}$, these matrices should be truncated after a particular order N and N_o respectively. The

where $\delta_{i,j}$ is the Kronecker delta function. The Hamiltonian matrix elements $H_{\alpha\beta}^{[n-n',m-m']}$ can be written in terms of the unperturbed eigen-energy ϵ_α and coupling strengths $\Omega_{\alpha\beta}^{(k)}$ as,

$$H_{\alpha\beta}^{[n-n',m-m']} = \varepsilon_\alpha \delta_{\alpha,\beta}\delta_{n,n'}\delta_{m,m'} + \sum_{k=-N}^{N} \Omega_{\alpha\beta}^{(k)} \left(\delta_{n+1,n'}\delta_{m+k,m'} + \delta_{n-1,n'}\delta_{m-k,m'}\right). \tag{5.11}$$

Hence, by determining the matrix element $H_{\alpha\beta}^{[n-n',m-m']}$, we can determine the complete infinite dimensional matrix $\mathbb{H}_{\omega_k}^F$, a sparse matrix containing many infinite dimensional sub-matrices, describes the atom-field interaction Hamiltonian in the Floquet space. The suffix ω_k in the Hamiltonian denotes the inclusion of all the components of the polychromatic rf-field with frequencies ω_k. The matrix containing only the contribution of ω_0, denoted as $\mathbb{H}_{\omega_0}^F$, is also an infinite dimensional matrix and is a sub-matrix of the composite Floquet matrix $\mathbb{H}_{\omega_k}^F$. An examination of the expanded form of these Floquet matrices can provide enough insight about their recursive and composite structure. Central region of these infinite dimensional matrices are shown as below,

$$\mathbb{H}_{\omega_k}^F = \begin{bmatrix}
\ddots & \vdots & & & & \vdots & \\
\cdots & \mathbb{H}_{\omega_0}^F + 2\hbar\omega_r\mathbb{I} & \mathbb{Q}_1 & \mathbb{Q}_2 & \mathbb{Q}_3 & \mathbb{Q}_4 & \cdots \\
 & \mathbb{Q}_1^T & \mathbb{H}_{\omega_0}^F + \hbar\omega_r\mathbb{I} & \mathbb{Q}_1 & \mathbb{Q}_2 & \mathbb{Q}_3 & \\
 & \mathbb{Q}_2^T & \mathbb{Q}_1^T & \mathbb{H}_{\omega_0}^F & \mathbb{Q}_1 & \mathbb{Q}_2 & \\
 & \mathbb{Q}_3^T & \mathbb{Q}_2^T & \mathbb{Q}_1^T & \mathbb{H}_{\omega_0}^F - \hbar\omega_r\mathbb{I} & \mathbb{Q}_1 & \\
\cdots & \mathbb{Q}_4^T & \mathbb{Q}_3^T & \mathbb{Q}_2^T & \mathbb{Q}_1^T & \mathbb{H}_{\omega_0}^F - 2\hbar\omega_r\mathbb{I} & \cdots \\
 & \vdots & & & & \vdots & \ddots
\end{bmatrix}; \tag{5.12}$$

mal atomic basis set $\{|\alpha\rangle\}$ comprising the Zeemann split levels of the atomic system. The eigen-energies of this Hamiltonian H_0 are defined as,

$$\epsilon_\alpha = \langle\alpha|H_0|\alpha\rangle. \tag{5.6}$$

The coupling strengths between the different eigen-states $\{|\alpha\rangle\}$ due to the time varying rf-fields are given by,

$$\Omega^{(k)}_{\alpha\beta} = -\frac{1}{2}\langle\alpha|\boldsymbol{\mu}.\mathbf{B}_k|\beta\rangle \tag{5.7}$$

where $|\alpha\rangle$ and $|\beta\rangle$ represents different atomic states belonging to the atomic basis set $\{|\alpha\rangle\}$.

In order to expand the complete Hamiltonian of Eq. (5.5), we construct two independent orthonormal fourier basis sets $\{|n\rangle\}$ and $\{|m\rangle\}$ representing the basis frequencies of the polychromatic rf-field, *i.e.* ω_0 and ω_r respectively. The complete atom-field system can now be described in terms of the composite Floquet basis set,

$$\{|\alpha nm\rangle\} = \{|\alpha\rangle\} \otimes \{|n\rangle\} \otimes \{|m\rangle\}. \tag{5.8}$$

As the Hilbert space spanned by these Floquet basis sets is infinite dimensional, the Hamiltonian represented in this basis set (called Floquet matrix H^F) is also an infinite dimensional matrix having the unperturbed Hamiltonian H_0 as the central component. Thus, we can transform the time dependent Hamiltonian of Eq. (5.5) to a class of eigen-value problem using the procedure described in an earlier work by [95] as,

$$\sum_\beta \sum_{n'} \sum_{m'} \langle\alpha nm|H^F|\beta n'm'\rangle\langle\beta n'm'|\epsilon\rangle = \epsilon\langle\alpha nm|\epsilon\rangle \tag{5.9}$$

where ϵ is the eigen-energy and $|\epsilon\rangle$ is the eigen-vectors of H^F.

The matrix elements of H^F can be determined as,

$$\langle\alpha nm|H^F|\beta n'm'\rangle = H^{[n-n',m-m']}_{\alpha\beta} + (n\omega_0 + m\omega_r)\delta_{\alpha,\beta}\delta_{n,n'}\delta_{m,m'} \tag{5.10}$$

as compared to the separation between the frequency components (*i.e.* ω_r). Under this approximation, the polychromatic rf-field can then be written as,

$$\mathbf{B}(t) = \sum_k \mathbf{B}_k \Re\left[e^{i\omega_k t}\right] \tag{5.1}$$

where,

$$\omega_k = \omega_0 + k\omega_r \text{ with } k = 0, \pm 1, \pm 2, \dots , \tag{5.2}$$

and ω_0 is the frequency of the central component. The monochromatic field components $\mathbf{B}_k$ can be described as,

$$\mathbf{B}_k = \mathbf{B}_0 G(\omega_k), \tag{5.3}$$

with $\mathbf{B}_0$ being the amplitude of the central component and $G(\omega)$ being the envelope function governing the amplitude of the other components relative to the amplitude of the central component in the comb spectrum. If we consider only $2N + 1$ modes having significant amplitude, then Eq. (5.1) can be rewritten as,

$$\mathbf{B}(t) = \sum_{k=-N}^{k=N} \mathbf{B}_0 G(\omega_k) \Re\left[e^{i\omega_k t}\right]. \tag{5.4}$$

Hence, using a suitable value of N along with an appropriately chosen envelop function $G(\omega)$, the rf-field $B(t)$ can have arbitrary polychromatic nature while being described by the two basis frequencies ω_0 and ω_r. In presence of the rf-field of Eq. (5.4), the complete system Hamiltonian of Eq. (2.2) takes the form,

$$H = H_0 - \sum_{k=-N}^{k=N} \boldsymbol{\mu}.\mathbf{B}_0 G(\omega_k) \Re[e^{i\omega_k t}], \tag{5.5}$$

where, $H_0 = \mathcal{H} - \mu.\mathbf{B}_s$ with $\mathcal{H}$ being the unperturbed Hamiltonian and $\mathbf{B}_s = B_q(x, y, -2z)^T$ being the field of a static quadrupole trap. The parameter μ is the magnetic dipole moment of the atoms. As a whole, H_0 represent the atomic Hamiltonian corresponding to the interaction of atoms with the static field B_s and hence can be represented in the orthonor-

magnetic field has been studied theoretically. The atom-field interaction is studied using the many mode Floquet theory (MMFT) formalism, which has been applied in several areas of science in the earlier works [95, 96, 97, 98, 99, 100, 101]. In particular, the use of MMFT is very popular to study interaction of atoms with ultra intense laser fields and to explain several important phenomenon such as multi-photon ionization and generation of higher harmonics [102, 103, 104]. Applying MMFT formalism we have shown that interaction between an atom and a strong polychromatic rf-field can result in several interesting phenomena. These include the generation of lattice like periodic potentials for cold atoms, large two photon transition and enhancement or suppression of single and two photon transition probabilities with the variation in the mode separation frequency of the polychromatic rf-field. The enhancement in two photon transitions is correlated to enhanced population in the intermediate states. The lattice like periodic dressed state potentials are convenient to manipulate atoms as compared to their counterpart in optical domain.

5.1 Many Mode Floquet Theory

In order to utilize the many mode Floquet formalism to study the interaction of cold atoms with a polychromatic rf-field, we consider the atom cloud trapped in a quadrupole trap with a field distribution described by Eq. (2.4) and exposed to a polychromatic rf-field $\mathbf{B}(t)$. Such an atomic system, fundamentally described by the Eqs. (2.1) - (2.5) in chapter 2, can be dealt with either by constructing a recursive Floquet Hamiltonian or by expanding the complete Hamiltonian as a Magnus series [105, 106].

In order to keep the problem simple, the polychromatic rf-field $\mathbf{B}(t)$ is considered to be composed of several monochromatic field components with their frequencies as ω_k, with $k = 0, \pm 1, \pm 2, ... \pm \infty$. Here we consider the frequency spectrum of the polychromatic field to be a comb type in which the width of the individual components $\Delta\omega_k$ is negligible

Chapter 5

Radio-frequency dressed traps with poly-chromatic rf-fields

The progress so far made in the area of rf-dressed potentials is limited to the use of single [49, 69, 77, 88, 43] or few frequencies [85, 90, 91, 92, 93] used in the dressing rf field. With a polychromatic dressing rf field and a static magnetic field, the theoretical description of the interaction of an atom with these fields becomes complicated as the underlying conditions reside well outside the validity regime of rotating wave approximations (RWA). Nevertheless, the case of an rf field having components at two frequencies, one component being much stronger than the other, has been treated perturbatively to explain the results of rf-spectroscopy of ultracold atoms trapped in an rf dressed potential of stronger rf fields [90, 94]. For the case of all frequency components in the rf field being sufficiently strong, a local resonance model was suggested by Courteille et al [91], which also breaks down for rf fields with closely spaced frequencies. To address this situation, there exist a requirement of a more accurate theoretical formalism which can deal with a polychromatic rf field of arbitrary frequency spectrum and field strength which is interacting with cold atoms trapped in a magnetic trap.

In this chapter, the interaction of a polychromatic rf-field with an atom trapped in a static

6.2 Future plan

Techniques presented in this thesis can be extended in future to perform a set of different type of experiments which can be useful to utilize ultra-cold atoms in various applications.

An experimentally generated tilted ring trap along with a frequency modulator attached between the rf-field sources can be of great use to rotate the atom cloud as described in theory in Chapter 2. These techniques with proper set of pulse sequences can act as an atomic conveyor belt to transfer an atom cloud to a desired location inside the trapping zone.

The numerically predicted rf-dressed lattice potentials with poly-chromatic rf-field are yet to be realized experimentally and can be an excellent tool to study condensed matter physics without the limitations posed by the optical lattices. These rf-dressed lattices, in which the shape and the separation of the lattice wells can be altered in a wide range otherwise not achievable in the common sinusoidal optical lattices can lead to a better understanding about a plethora of physical phenomenons observed in the domain of solid state physics.

An rf-spectroscopy technique based on the predicted large two photon transition probabilities in the periodic rf-dressed lattice potentials also need to be realized experimentally. Atom cloud characterization methods relying on these rf-spectroscopy techniques may enable one to determine the trap frequencies, trapped atom cloud temperatures and number of atoms trapped in it in near future.

ones. The numerical studies performed with this simulation technique enabled us to identify key processes and mechanisms of the complete evolution of the atom cloud from the quadrupole trap to the ring trap.

The loss mechanisms in the atom cloud trapped in the quadrupole trap and the rf-dressed trap were studied by holding a cold atom cloud in both the traps for a similar amount of time and observing the decay of number of trapped atoms. This study indeed shown that the loss rates are lower for the rf-dressed traps than the quadrupole traps. These higher amount of trapped atoms were useful to perform any further study on the rf-dressed trap.

A larger part of the existing literature dealt with the rf-dressed potentials using the monochromatic rf-fields [50, 56, 49] and a very few works have been carried out to study the effect of an rf-field with more than one frequency in the generation of the rf-dressed potentials [91]. To address this specific issue, we have studied the generation of the rf-dressed potentials with the polychromatic rf-field and static quadrupole trap, using the many mode Floquet theory [112]. This work has provided several new results and accurate treatment of the atom field interaction as compared to the earlier studies which were based on the rotating wave and local resonance approximations. We have obtained the lattice like periodic potentials in which the lattice shape and separation can be controlled directly by modifying the rf-field parameters. These potentials are far more superior to their optical counter parts in order to mimic original lattice potentials. In this study, large multi-photon transition probabilities [113] are also obtained in these rf-dressed lattices. These multi-photon transitions can become a perfect tool to characterize the trapped atom clouds using rf-spectroscopy techniques [90].

In conclusion, a detailed study has been presented in this thesis related to the generation of rf-dressed potentials in order to trap and manipulate ultra-cold atoms.

Next, some of the predicted rf-dressed potentials were realized [88] using a double magneto optical trap setup along with a custom built control system capable to operate the complete experimental setup with extreme precision in the time delay mechanism. In these experiments, using two separate rf-field generators, we have cooled the atom cloud evaporatively and then transferred the cold atom cloud from the quadrupole trap to an rf-dressed ring trap. In this ring trap, we have studied the dependence of the ring trap radius on the applied rf-field frequency. The application of another rf-radiation from another rf-source was also used to produce a tilted ring trap in which the asymmetry of the rf-dressed potentials were eminent. In a separate study, after the trapping of the atom cloud in the ring trap by radiating an rf-field of constant resonant frequency, we have produced an atom cloud with two concentric parts in which the two different Zeeman hyperfine spin components were spatially separated. This type of dual spin traps can be utilized to study spin dependence of collisional processes in ultra-cold atoms simultaneously for both the spin states.

Further experiments were performed to realize the ring or toroidal trap with the use of a single rf-field ramp, in which both the frequency and the amplitude of the rf-field was varied in a time dependent manner. This enabled us to perform the evaporative cooling as well as the rf-dressed trapping of the atom cloud simultaneously, resulting in the formation of the ring trap starting from the spherically symmetric quadrupole trap. The complete evolution process was experimentally studied with the use of a set of time resolved absorption probe images during the complete frequency ramp. By studying the rate of loss of number of atoms trapped in the atom cloud it was found that the evolution processes was divided in two parts. The atom cloud initially suffered from heavy atom losses in the form of evaporation process and in the final part the atom losses got reduced while the trapping of the atom cloud in the rf-dressed potential occurred. To obtain a detailed insight of the evolution dynamics, a direct simulation Monte Carlo method was utilized in which the Boltzmann equation of transport theory was solved in the discrete particle approximations with all the parameters being in vicinity of the experimental

Chapter 6

Conclusion

6.1 Summary

This thesis describes the theoretical calculations and experimental demonstration of radio frequency dressed potentials for trapping and manipulation of cold atoms. The basic limitation with the static magnetic traps are their inability to render 'rich' potential landscapes filled with both local minima and maxima. This restriction arises due to the Maxwell's equations along with the Earnshaw's theorem. To overcome this constraint, on design of potentials with more exquisite shapes and usefulness for specific applications, rf-dressed potentials can be used. These potentials can lead to some very useful trapping geometries, which are difficult to accomplish using static magnetic traps alone.

To understand the basics of the rf-dressed trapping schemes, initially a numerical study was performed in order to obtain all the parameters which can be realized experimentally in our lab. During this study [77], apart from all the potentials obtained by earlier studies [47, 43], we found new type of potentials which are asymmetric in nature and can be made to rotate or oscillate with a tunable rotation or oscillation frequency. These rotating potentials equipped with the tunability, can be useful in atom transport in studies related to super-fluidity and tunneling.

[104] M. Holthaus. Floquet engineering with quasienergy bands of periodically driven optical lattices. *Journal of Physics B: Atomic, Molecular and Optical Physics*, **49**(1), 013001, (2016).

[105] M. Klaiber, D. Dimitrovski, and J. S. Briggs. Magnus expansion for laser-matter interaction: Application to generic few-cycle laser pulses. *Phys. Rev. A*, **79**, 043402, (2009).

[106] E. A. Butcher, M. Sari, E. Bueler, and T. Carlson. MagnusâĂŹ expansion for time-periodic systems: Parameter-dependent approximations. *Communications in Nonlinear Science and Numerical Simulation*, **14**(12), 4226 – 4245, (2009).

[107] G. Grynberg, A. Aspect, and C. Fabre. *Introduction to Quantum Optics*. Cambridge University Press. (2010).

[108] S. I. Chu and W. P. Reinhardt. Intense field multiphoton ionization via complex dressed states: Application to the h atom. *Phys. Rev. Lett.*, **39**, 1195–1198, (1977).

[109] H. P. Breuer and M. Holthaus. Adiabatic processes in the ionization of highly excited hydrogen atoms. *Z. Phys. D: At. Mol. and Clusters*, **11**(1), 1–14, (1989).

[110] H.P. Breuer and M. Holthaus. Quantum phases and landau-zener transitions in oscillating fields. *Physics Letters A*, **140**(9), 507 – 512, (1989).

[111] N. V. Vitanov and K. A. Suominen. Time-dependent control of ultracold atoms in magnetic traps. *Phys. Rev. A.*, **56**(6), R4377, (1997).

[112] A. Chakraborty and S. R. Mishra. A floquet formalism for the interaction of magnetically trapped atoms with rf fields. *Journal of Physics B: Atomic, Molecular and Optical Physics*, **51**(2), 025002, (2018).

[113] A. Chakraborty and S. R. Mishra. Resonance enhancement of two photon absorption by magnetically trapped atoms in strong rf-fields. *Physics Letters A*, **382**(4), 157 – 161, (2018).

[96] T. S. Ho and S. I. Chu. Semiclassical many-mode floquet theory. ii. non-linear multiphoton dynamics of a two-level system in a strong bichromatic field. *Journal of Physics B: Atomic and Molecular Physics*, **17**(10), 2101, (1984).

[97] T. S. Ho and S. I. Chu. Semiclassical many-mode floquet theory. iii. su(3) dynamical evolution of three-level systems in intense bichromatic fields. *Phys. Rev. A*, **31**, 659–676, (1985).

[98] T. S. Ho and S. I. Chu. Semiclassical many-mode floquet theory. iv. coherent population trapping and su(3) dynamical evolution of dissipative three-level systems in intense bichromatic fields. *Phys. Rev. A*, **32**, 377–395, (1985).

[99] P. M. Blekher, H. R. Jauslin, and J. L. Lebowitz. Floquet spectrum for two-level systems in quasiperiodic time-dependent fields. *Journal of Statistical Physics*, **68**(1), 271–310, (1992).

[100] S. I. Chu and D. A. Telnov. Beyond the floquet theorem: generalized floquet formalisms and quasienergy methods for atomic and molecular multiphoton processes in intense laser fields. *Physics Reports*, **390**(1âĂŞ2), 1 – 131, (2004).

[101] M. Bukov, L. D'Alessio, and A. Polkovnikov. Universal high-frequency behavior of periodically driven systems: from dynamical stabilization to floquet engineering. *Advances in Physics*, **64**(2), 139–226, (2015).

[102] I S Ruddock. Nonlinear optical second harmonic generation. *European Journal of Physics*, **15**(2), 53, (1994).

[103] S. K. Son and S. I. Chu. Many-mode floquet theoretical approach for coherent control of multiphoton dynamics driven by intense frequency-comb laser fields. *Phys. Rev. A*, **77**, 063406, (2008).

[86] G. E. Skvortsov. Spectrum and evolution of boltzmann systems. *Journal of Experimental and Theoretical Physics*, **25**(5), 853, (1967).

[87] G. E. Skvortsov. The dynamics of boltzmann systems. *Journal of Experimental and Theoretical Physics*, **30**(6), 1114, (1970).

[88] A. Chakraborty, S. R. Mishra, S. P. Ram, S. K. Tiwari, and H. S. Rawat. A toroidal trap for cold ^{87}Rb atoms using an rf-dressed quadrupole trap. *Journal of Physics B: Atomic, Molecular and Optical Physics*, **49**(7), 075304, (2016).

[89] O. Morizot, C. L. G. Alzar, P. E. Pottie, V. Lorent, and H. Perrin. Trapping and cooling of rf-dressed atoms in a quadrupole magnetic field. *Journal of Physics B: Atomic, Molecular and Optical Physics*, **40**(20), 4013, (2007).

[90] R. K. Easwaran, L. Longchambon, P. E. Pottie, V. Lorent, H. Perrin, and B. M. Garraway. Rf spectroscopy in a resonant rf-dressed trap. *Journal of Physics B: Atomic, Molecular and Optical Physics*, **43**(6), 065302, (2010).

[91] Ph. W. Courteille, B. Deh, J. Fortagh, A. Gunther, S. Kraft, C. Marzok, S. Slama, and C. Zimmermann. Highly versatile atomic micro traps generated by multifrequency magnetic field modulation. *J. Phys. B*, **39**, 1055, (2006).

[92] S. Hofferberth, B. Fischer, T. Schumm, J. Schmiedmayer, and I. Lesanovsky. Ultracold atoms in radio-frequency dressed potentials beyond the rotating-wave approximation. *Phys. Rev. A*, **76**, 013401, (2007).

[93] T. Morgan and Th. Busch. Adiabatic potentials using multiple radio frequencies.

[94] A. G. Martin, K. Helmerson, V. S. Bagnato, G. P. Lafyatis, and D. E. Pritchard. rf spectroscopy of trapped neutral atoms. *Phys. Rev. Lett.*, **61**, 2431–2434, (1988).

[95] T. S. Ho, S. I. Chu, and J. V. Tietz. Semiclassical many-mode floquet theory. *Chem. Phys. Lett*, **96**(4), 464 – 471, (1983).

[76] S. P. Ram, S. R. Mishra, S. K. Tiwari, and H. S. Rawat. Temperature and phase-space density of a cold atom cloud in a quadrupole magnetic trap. *Journal of the Korean Physical Society*, **65**(4), 462–470, (2014).

[77] A. Chakraborty and S. R. Mishra. Anisotropic two-dimensional rf-dressed potentials for ultracold atoms. *J. of the Kor. Phys. Soc.*, **65**, 1324–1335, (2014).

[78] G. A. Bird. *Molecular Gas Dynamics and the Direct Simulation of Gas Flows*. Oxford University Press Inc. (1994).

[79] H. Wu and C. J. Foot. Direct simulation of evaporative cooling. *Journal of Physics B: Atomic, Molecular and Optical Physics*, **29**(8), L321, (1996).

[80] H. Wu, E. Arimondo, and C. J. Foot. Dynamics of evaporative cooling for bose-einstein condensation. *Phys. Rev. A*, **56**, 560–569, (1997).

[81] Wu, H. and Arimondo, E. Expansion of the non-condensed trapped bose gas in bose-einstein condensation. *Europhys. Lett.*, **43**(2), 141–146, (1998).

[82] K. A. Suominen, E. Tiesinga, and P. S. Julienne. Nonadiabatic dynamics in evaporative cooling of trapped atoms by a radio-frequency field. *Phys. Rev. A*, **58**, 3983–3992, (1998).

[83] Z. Y. Ma, A. M. Thomas, C. J. Foot, and S. L. Cornish. The evaporative cooling of a gas of caesium atoms in the hydrodynamic regime. *Journal of Physics B: Atomic, Molecular and Optical Physics*, **36**(16), 3533, (2003).

[84] A. C. J. Wade, D. Baillie, and P. B. Blakie. Direct simulation monte carlo method for cold-atom dynamics: Classical boltzmann equation in the quantum collision regime. *Phys. Rev. A*, **84**, 023612, (2011).

[85] Carlos L. G. Alzar, H. Perrin, B. M. Garraway, and V. Lorent. Evaporative cooling in a radio-frequency trap. *Phys. Rev. A*, **74**, 053413, (2006).

[67] M. Vangeleyn, B. M. Garraway, H. Perrin, and A. S. Arnold. Inductive dressed ring traps for ultracold atoms. *Journal of Physics B: Atomic, Molecular and Optical Physics*, **47**(7), 071001, (2014).

[68] T. Fernholz, R. Gerritsma, P. Krüger, and R. J. C. Spreeuw. Dynamically controlled toroidal and ring-shaped magnetic traps. *Phys. Rev. A*, **75**, 063406, (2007).

[69] O. Morizot, Y. Colombe, V. Lorent, H. Perrin, and B. M. Garraway. Ring trap for ultracold atoms. *Phys. Rev. A*, **74**, 023617, (2006).

[70] E. M. Wright, J. Arlt, and K. Dholakia. Toroidal optical dipole traps for atomic bose-einstein condensates using laguerre-gaussian beams. *Phys. Rev. A*, **63**, 013608, (2000).

[71] V. G. Minogin, J. A. Richmond, and G. I. Opat. Time-orbiting-potential quadrupole magnetic trap for cold atoms. *Phys. Rev. A*, **58**, 3138–3145, (1998).

[72] M. Gildemeister, E. Nugent, B. E. Sherlock, M. Kubasik, B. T. Sheard, and C. J. Foot. Trapping ultracold atoms in a time-averaged adiabatic potential. *Phys. Rev. A*, **81**, 031402, (2010).

[73] M. Gildemeister, B. E. Sherlock, and C. J. Foot. Techniques to cool and rotate bose-einstein condensates in time-averaged adiabatic potentials. *Phys. Rev. A*, **85**, 053401, (2012).

[74] S. R. Mishra, S. P. Ram, S. K. Tiwari, and S. C. Mehendale. Enhanced atom transfer in a double magneto-optical trap setup. *Phys. Rev. A*, **77**, 065402, (2008).

[75] S. P. Ram, S. K. Tiwari, S. R. Mishra, and H. S. Rawat. Push beam spot-size dependence of atom transfer in a double magneto-optical trap setup. *Review of Scientific Instruments*, **84**(7), 073102, (2013).

[57] F. Bloch. Superfluidity in a ring. *Phys. Rev. A*, **7**, 2187, (1973).

[58] A. S. Arnold and E. Riis. Bose-einstein condensates in 'giant' toroidal magnetic traps. *Journal of Modern Optics*, **49**(5-6), 959–964, (2002).

[59] A. Ramanathan, K. C. Wright, S. R. Muniz, M. Zelan, W. T. Hill, C. J. Lobb, K. Helmerson, W. D. Phillips, and G. K. Campbell. Superflow in a toroidal bose-einstein condensate: An atom circuit with a tunable weak link. *Phys. Rev. Lett.*, **106**, 130401, (2011).

[60] K. P. Marzlin and W. Zhang. Laser-induced rotation of a trapped bose-einstein condensate. *Phys. Rev. A*, **57**, 3801–3804, (1998).

[61] G. C. Marques, V. Bagnato, and D. Spehler. Fluidity aspects of bose-einstein condensed systems. *Phys. Rev. A*, **63**, 043607, (2001).

[62] P. L. Halkyard. *Dynamics in Cold Atomic Gases: Resonant Behaviour of the Quantum Delta-Kicked Accelerator and Bose-Einstein Condensates in Ring Traps*. PhD thesis, Durham University, 2010.

[63] K. T. Kapale and J. P. Dowling. Vortex phase qubit: Generating arbitrary, counter-rotating, coherent superpositions in bose-einstein condensates via optical angular momentum beams. *Phys. Rev. Lett.*, **95**, 173601, (2005).

[64] J. A. Sauer, M. D. Barrett, and M. S. Chapman. Storage ring for neutral atoms. *Phys. Rev. Lett.*, **87**, 270401, (2001).

[65] A. Hopkins, B. Lev, and H. Mabuchi. Proposed magnetoelectrostatic ring trap for neutral atoms. *Phys. Rev. A*, **70**, 053616, (2004).

[66] P. F. Griffin, E. Riis, and A. S. Arnold. Smooth inductively coupled ring trap for atoms. *Phys. Rev. A*, **77**, 051402, (2008).

[47] I. Lesanovsky, T. Schumm, S. Hofferberth, L. M. Andersson, P. Krüger, and J. Schmiedmayer. Adiabatic radio-frequency potentials for the coherent manipulation of matter waves. *Phys. Rev. A*, **73**, 033619, (2006).

[48] Y. Colombe, E. Knyazchyan, O. Morizot, B. Mercier, V. Lorent, and H. Perrin. Ultracold atoms confined in rf-induced two-dimensional trapping potentials. *EPL (Europhysics Letters)*, **67**(4), 593, (2004).

[49] K. Merloti, R. Dubessy, L. Longchambon, A. Perrin, P. E. Pottie, V. Lorent, and H. Perrin. A two-dimensional quantum gas in a magnetic trap. *New Journal of Physics*, **15**(3), 033007, (2013).

[50] M. White, H. Gao, M. Pasienski, and B. DeMarco. Bose-einstein condensates in rf-dressed adiabatic potentials. *Phys. Rev. A*, **74**, 023616, (2006).

[51] K. Merloti, R. Dubessy, L. Longchambon, M. Olshanii, and H. Perrin. Breakdown of scale invariance in a quasi-two-dimensional bose gas due to the presence of the third dimension. *Phys. Rev. A.*, **88**, 061603, (2013).

[52] W. H. Heathcote, E. Nugent, B. T. Sheard, and C. J. Foot. A ring trap for ultracold atoms in an rf-dressed state. *New Journal of Physics*, **10**(4), 043012, (2008).

[53] B. E. Sherlock, M. Gildemeister, E. Owen, E. Nugent, and C. J. Foot. Time-averaged adiabatic ring potential for ultracold atoms. *Phys. Rev. A*, **83**, 043408, (2011).

[54] M. Gildemeister. *Trapping ultracold atoms in time-averaged adiabatic potentials*. PhD thesis, University of Oxford, 2010.

[55] W. Heathcote. *A toroidal trap for ultracold atoms in a rf-dressed state*. PhD thesis, University of Oxford, 2007.

[56] I. Lesanovsky and W. von Klitzing. Time-averaged adiabatic potentials: Versatile matter-wave guides and atom traps. *Phys. Rev. Lett.*, **99**, 083001, (2007).

[37] Y. P. Wang, J. Q. Zhong, X. Chen, R. B. Li, D. W. Li, L. Zhu, H. W. Song, J. Wang, and M. S. Zhan. Extracting the differential phase in dual atom interferometers by modulating magnetic fields. *Optics Communications*, **375**, 34 – 37, (2016).

[38] A. Gauguet, B. Canuel, T. Leveque, W. Chaibi, and A. Landragin. Characterization and limits of a cold-atom sagnac interferometer. *Phys. Rev. A*, **80**, 063604, (2009).

[39] S. R. Segal. *Progress towards an ultracold atomic Sagnac gyroscope*. PhD thesis, Pennsylvania State University, 2003.

[40] J. Fortagh, A. Grossmann, C. Zimmermann, and T. W. Hansch. Miniaturized wire trap for neutral atoms. *Phys. Rev. Lett.*, **81**, 5310–5313, (1998).

[41] R. Folman, P. Krueger, J. Schmiedmayer, J. Denschlag, and C. Henkel. Microscopic atom optics: from wires to an atom chip. *Adv. At. Mol. Opt. Phys.*, **48**, 263, (2002).

[42] T. Schumm, S. Hofferberth, L. M. Anderson, S. Widermuth, S. Groth, I. Bar-Joseph, J. Schmiedmayer, and P. Kruger. Matter-wave interferometry in a double well on an atom chip. *Nat. Phys.*, **1**, 57, (2005).

[43] S. Hofferberth, I. Lesanovsky, B. Fischer, J. Verdu, and J. Schmiedmayer. Radiofrequency-dressed-state potentials for neutral atoms. *Nat. Phys.*, **2**, 710–716, (2006).

[44] M. Inguscio, S. Stringari, and C.E.Wieman, editors. *Procedings of International School of Physics, Enrico Fermi Course CXL*. IOS Press, Amsterdam, 1999.

[45] O. Zobay and B. M. Garraway. Two-dimensional atom trapping in field-induced adiabatic potentials. *Phys. Rev. Lett.*, **86**, 1195–1198, (2001).

[46] O. Zobay and B. M. Garraway. Atom trapping and two-dimensional bose-einstein condensates in field-induced adiabatic potentials. *Phys. Rev. A*, **69**, 023605, (2004).

[28] F. G. Deng, X. H. Li, C. Y. Li, P. Zhou, and H. Y. Zhou. Quantum secure direct communication network with einsteinâĂŞpodolskyâĂŞrosen pairs. *Physics Letters A*, **359**(5), 359 – 365, (2006).

[29] D. Schrader, I. Dotsenko, M. Khudaverdyan, Y. Miroshnychenko, A. Rauschenbeutel, and D. Meschede. Neutral atom quantum register. *Phys. Rev. Lett.*, **93**, 150501, (2004).

[30] O. Mandel, M. Greiner, A. Widera, T. Rom, T. W. HÃd'nsch, and I. Bloch. Controlled collisions for multi-particle entanglement of optically trapped atoms. *Nature*, **425**, 937, (2003).

[31] B. Canuel, F. Leduc, D. Holleville, A. Gauguet, J. Fils, A. Virdis, A. Clairon, N. Dimarcq, Ch. J. Bordé, A. Landragin, and P. Bouyer. Six-axis inertial sensor using cold-atom interferometry. *Phys. Rev. Lett.*, **97**, 010402, (2006).

[32] Y. Le Coq, J. A. Retter, S. Richard, A. Aspect, and P. Bouyer. Coherent matter wave inertial sensors for precision measurements in space. *Applied Physics B*, **84**(4), 627–632, (2006).

[33] Muller, T., Gilowski, M., Zaiser, M., Berg, P., Schubert, Ch., Wendrich, T., Ertmer, W., and Rasel, E. M. A compact dual atom interferometer gyroscope based on laser-cooled rubidium. *Eur. Phys. J. D*, **53**(3), 273–281, (2009).

[34] G. Rosi, F. Sorrentino, L. Cacciapuoti, M. Prevedelli, and G. M. Tino. Precision measurement of the newtonian gravitational constant using cold atoms. *Nature*, **510**, 518, (2014).

[35] P. R. Berman. *Atom interferometry*. Academic Press Inc. (1997).

[36] A. B. Tacla, S. Boixo, A. Datta, A. Shaji, and C. M. Caves. Nonlinear interferometry with bose-einstein condensates. *Phys. Rev. A*, **82**, 053636, (2010).

[18] M. R. Andrews, D. M. Kurn, H.-J. Miesner, D. S. Durfee, C. G. Townsend, S. Inouye, and W. Ketterle. Propagation of sound in a bose-einstein condensate. *Phys. Rev. Lett.*, **79**, 553–556, (1997).

[19] I. Bloch. Ultracold quantum gases in optical lattices. *Nature Physics*, **1**, 23, (2005).

[20] P. Windpassinger and K. Sengstock. Engineering novel optical lattices. *Reports on Progress in Physics*, **76**(8), 086401, (2013).

[21] C. Ryu, P. W. Blackburn, A. A. Blinova, and M. G. Boshier. Experimental realization of josephson junctions for an atom squid. *Phys. Rev. Lett.*, **111**, 205301, (2013).

[22] M. Albiez, R. Gati, J. Fölling, S. Hunsmann, M. Cristiani, and M. K. Oberthaler. Direct observation of tunneling and nonlinear self-trapping in a single bosonic josephson junction. *Phys. Rev. Lett.*, **95**, 010402, (2005).

[23] M. Greiner, O. Mandel, T. W. Hansch, and I. Bloch. Quantum phase transition from a superfluid to a mott insulator in a gas of ultracold atoms. *Nature*, **415**, 39, (2002).

[24] M. Bartenstein, A. Altmeyer, S. Riedl, S. Jochim, C. Chin, J. Hecker Denschlag, and R. Grimm. Crossover from a molecular bose-einstein condensate to a degenerate fermi gas. *Phys. Rev. Lett.*, **92**, 120401, (2004).

[25] M. A. Nielsen and I. L. Chuang. *Quantum Computation and Quantum Information*. Cambridge University Press. (2000).

[26] J. I. Cirac and P. Zoller. Quantum computations with cold trapped ions. *Phys. Rev. Lett.*, **74**, 4091–4094, (1995).

[27] J. J. García-Ripoll, P. Zoller, and J. I. Cirac. Speed optimized two-qubit gates with laser coherent control techniques for ion trap quantum computing. *Phys. Rev. Lett.*, **91**, 157901, (2003).

[9] W. D. Phillips. Nobel lecture: Laser cooling and trapping of neutral atoms. *Rev. Mod. Phys.*, **70**, 721–741, (1998).

[10] Bose. Plancks gesetz und lichtquantenhypothese. *Zeitschrift für Physik*, **26**(1), 178–181, (1924).

[11] A. Einstein. Quantentheorie des einatomigen idealen gases. *Sitzungsber. Preuss. Akad. Wiss.*, **22**, 261, (1924).

[12] M. H. Anderson, J. R. Ensher, M. R. Matthews, C. E. Wieman, and E. A. Cornell. Observation of bose-einstein condensation in a dilute atomic vapor. *Science*, **269**(5221), 198–201, (1995).

[13] C. C. Bradley, C. A. Sackett, J. J. Tollett, and R. G. Hulet. Evidence of bose-einstein condensation in an atomic gas with attractive interactions. *Phys. Rev. Lett.*, **75**, 1687–1690, (1995).

[14] K. B. Davis, M. O. Mewes, M. R. Andrews, N. J. van Druten, D. S. Durfee, D. M. Kurn, and W. Ketterle. Bose-einstein condensation in a gas of sodium atoms. *Phys. Rev. Lett.*, **75**, 3969–3973, (1995).

[15] F. Schreck, L. Khaykovich, K. L. Corwin, G. Ferrari, T. Bourdel, J. Cubizolles, and C. Salomon. Quasipure bose-einstein condensate immersed in a fermi sea. *Phys. Rev. Lett.*, **87**, 080403, (2001).

[16] J. Javanainen and S. M. Yoo. Quantum phase of a bose-einstein condensate with an arbitrary number of atoms. *Phys. Rev. Lett.*, **76**, 161–164, (1996).

[17] L. Amico, D. Aghamalyan, F. Auksztol, H. Crepaz, R. Dumke, and L. C. Kwek. Superfluid qubit systems with ring shaped optical lattices. *Scientific Reports*, **4**, 4298, (2009).

Bibliography

[1] A. Ashkin. Atomic-beam deflection by resonance-radiation pressure. *Phys. Rev. Lett.*, **25**, 1321–1324, (1970).

[2] J. E. Bjorkholm, R. R. Freeman, A. Ashkin, and D. B. Pearson. Observation of focusing of neutral atoms by the dipole forces of resonance-radiation pressure. *Phys. Rev. Lett.*, **41**, 1361–1364, (1978).

[3] P. Meystre. *Atom Optics*. 33. Springer-Verlag New York. (2001).

[4] C. J. Foot. *Atomic Physics*. Oxford University Press. (2005).

[5] O. J. Luiten, M. W. Reynolds, and J. T. M. Walraven. Kinetic theory of the evaporative cooling of a trapped gas. *Phys. Rev. A.*, **53**(1), 381, (1996).

[6] M. Yamashita, M. Koashi, and N. Imoto. Quantum kinetic theory for evaporative cooling of trapped atoms: Growth of bose-einstein condensate. *Phys. Rev. A*, **59**, 2243–2249, (1999).

[7] R. Meppelink, R. A. Rozendaal, S. B. Koller, J. M. Vogels, and P. van der Straten. Thermodynamics of bose-einstein-condensed clouds using phase-contrast imaging. *Phys. Rev. A*, **81**, 053632, (2010).

[8] S. Chu. Nobel lecture: The manipulation of neutral particles. *Rev. Mod. Phys.*, **70**, 685–706, (1998).